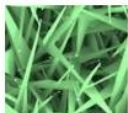
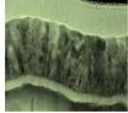


Institut für Festkörperphysik

FRIEDRICH-SCHILLER-UNIVERSITÄT JENA



 <p>Tiefemperaturphysik Prof. Dr. P. Seidel apl. Prof. Dr. F. Schmidl</p>	 <p>Angewandte Physik / Festkörperphysik Prof. Dr. T. Fritz</p>
 <p>Experimentelle Festkörperphysik Prof. Dr. C. Ronning</p>	 <p>Ionenstrahlphysik apl. Prof. Dr. E. Wendler</p>
 <p>Photovoltaik Prof. Dr. C. Ronning Dr. U. Reislöhner</p>	 <p>Laborastrophysik und Clusterphysik Dr. C. Jäger</p>

Annual Report 2015

Institut für Festkörperphysik

Friedrich-Schiller-Universität Jena

Annual Report 2015



Editor: Prof. Dr. Carsten Ronning & Cindy Büchner

**Institut für Festkörperphysik
Friedrich-Schiller-Universität Jena
Helmholtzweg 3/5
D-07743 JENA**

home page: <http://www.ifk.uni-jena.de/>

Prof. Dr. Torsten Fritz
(director) Tel.: +49 (0) 3641 / 947400, 947411
 Fax: +49 (0) 3641 / 947412
 e-mail: torsten.fritz@uni-jena.de
 home page: <http://www.organics.uni-jena.de>

Prof. Dr. Carsten Ronning Tel.: +49 (0) 3641 / 947300, 947301
 Fax: +49 (0) 3641 / 947302
 e-mail: carsten.ronning@uni-jena.de
 home page: <http://www.nano.uni-jena.de>
 <http://www.photovoltaik.uni-jena.de>

Prof. Dr. Paul Seidel Tel.: +49 (0) 3641 / 947410, 947411
 Fax: +49 (0) 3641 / 947412
 e-mail: paul.seidel@uni-jena.de
 home page: <http://www.tieftemperaturphysik.uni-jena.de/>

apl. Prof. Dr. Frank Schmidl Tel.: +49 (0) 3641 / 947429, 947411
 Fax: +49 (0) 3641 / 947412
 e-mail: frank.schmidl@uni-jena.de
 home page: <http://www.tieftemperaturphysik.uni-jena.de/>

apl. Prof. Dr. Elke Wendler Tel.: +49 (0) 3641 / 947333
 Fax: +49 (0) 3641 / 947302
 e-mail: elke.wendler@uni-jena.de
 home page: <http://www.physik2.uni-jena.de/inst/exphys/ionen/>

Dr. Cornelia Jäger Tel.: +49 (0) 3641 / 947354
 Fax: +49 (0) 3641 / 947308
 e-mail: cornelia.jaeger@uni-jena.de
 home page: <http://www.astrolab.uni-jena.de/>

Preface

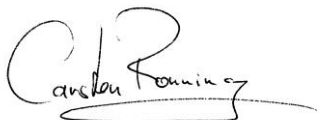
I am pleased to introduce this Annual Report, because 2015 was again a very successful year for the Institute of Solid State Physics (IFK) at the Friedrich-Schiller-University Jena. A significant amount of highly educated persons, which received either Master or PhD degrees among our research groups, left our institute and accepted new challenging jobs in industry and academia around the world in the past year. We are very proud on our alumni, which spent one of the most important time spans of their career with us, and now hold important positions and functions in our society.

We consider this education of young people at all levels as our most important duty and task, but we are also extremely proud on the research output produced in 2015. Even though our human recourses are continuously decreasing in the past years, the quality and quantity of scientific achievements is rather high and still increasing. Some outstanding examples are documented in the following pages of this report.

Furthermore, we like to take this annual report as an opportunity to thank a lot of people, funding agencies, and organizations for their manifold support for our research. We also like to thank all our colleagues at other universities and institutes all over the world, which were or still are collaborating with us, but where the collaborative work has not been presented in the research articles of this report.

Last but not least, we are very grateful for the work of our very motivated secretaries, technicians, and the people in the mechanical and electrical workshops. All of them have contributed to our research in an outstanding way and, thus, to this report.

Let's altogether keep up the excellent work in 2016 and beyond!

A handwritten signature in black ink, appearing to read 'Carsten Ronning', with a stylized flourish underneath.

Prof. Dr. Carsten Ronning

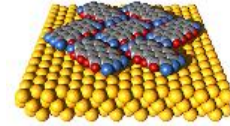
Content

1. Scientific Groups of the Institute (Portraits)	11
1.1 Applied Physics / Solid State Physics [Prof. Fritz]	12
1.2 Experimental Physics / Solid State Physics [Prof. Ronning]	13
1.3 Low Temperature Physics [Prof. Seidel]	14
1.4 Ion Beam Physics [Prof. Wendler]	15
1.4 Laboratory Astrophysics / Cluster Physics [Dr. Jäger]	16
2. Current Research Projects	17
2.1 Research Areas and Important Results	17
2.2 Third Party Grants	20
3. Publications, Invited Talks, and Theses	22
3.1 Publications in Scientific Journals	22
3.2 Invited Talks at Conferences and Colloquia	27
3.3 Theses	29
4. Cooperations, Visiting Scientists, and Colloquia at the IFK	32
4.1 Cooperations	32
4.2 Visiting Scientists	33
4.3 Colloquia at the Institute of Solid State Physics	34
5. Personnel	35
6. Technical Reports and Equipment	37
6.1 Operation of the Ion-Accelerator JULIA and the Ion-Implanter ROMEO	37
6.2 Cryogenic Services (TTS)	39
6.3 Equipment	40
7. Scientific Reports	43
Plastic deformation in ion irradiated, amorphous Si nanowires	44
Modeling of redeposition and sputtering of ion irradiated Au nanoparticles	46
Measuring the laser onset time of semiconductor nanowire lasers	48
Cathodoluminescence of CIGSe solar-cell-lamellae	50
Advanced X-ray fluorescence analysis of Cu(In,Ga)Se ₂ cross sections	52
Activation of Al dopants in contacted ZnO nanowires	54
Electroluminescence of single Eu implanted ZnO nanowires	56
Investigations of the electroluminescence of single Eu ion implanted ZnO nanowires at room temperature	58

Investigation of the Potassium-Doping of Tetraphenyldibenzoperiflanthene (DBP) on Ag(111) by Photoelectron Spectroscopy	60
Commensurism at Electronically Weakly Interacting Phthalocyanine/PTCDA Heterointerfaces	62
Electronic structure of one monolayer DBP on HOPG	64
Planar Hybrid Josephson Junctions on FeSe _{0.5} Te _{0.5} Thin Films	66
Measuring the photo-elastic coefficients of silicon at 1550 nm by means of a rotating wave plate polarimeter	68
Zero-field steps and resonant modes of the long Josephson junction	70
Point contact spectroscopy of Co-doped Ba-122 single crystals	72
The Einstein Telescope	74
Cryogenic Current Comparator for Storage Rings and Accelerators	76
Towards a single photon detector in the microwave regime	78
Optical absorption of silicon at near infrared and its correlation with electronic properties at cryogenic temperatures	80
Examination of bicrystal grain boundary junctions of BaFe ₂ (As,P) ₂ pnictide superconductors	82
A portable three-axis SQUID-based absolute vector magnetometer	84
Effects of LC shunting on the Shapiro steps features of a Josephson junction	86
Multi-resonance frequencies matching – Measurement of very small inductivities	88
Inner-gap structure in differential-conductance spectra of superconducting junctions with degraded interfaces	90
Direction-dependent RBS channelling studies in ion implanted LiNbO ₃	92
Ion-induced erosion of ice-covered carbon grains in molecular clouds and planetary disks	94
Photostability of PAH molecules - Interstellar chemistry	96
In-situ temperature dependent resistance measurement of ion irradiated vanadium dioxide thin films	98

1. Scientific Groups of the Institute (Portraits)

Applied Physics / Solid State Physics



Prof. Dr. Torsten Fritz

- Preparation of highly ordered thin films of organic molecules by UHV-deposition (OMBE)
- Chemical vapor deposition and characterization of carbon nanotubes
- Epitaxial graphene
- Organic-organic heteroepitaxy
- K-doped organic semiconductors and superconductors
- *In situ* optical spectroscopy (DRS and PL) on ultrathin molecular layers
- Analyses of surfaces, layers and nanostructures using AES, UPS, ARUPS, XPS, LEED, RHEED, XPD, STM, AFM, and SEM

The group *Applied Physics / Solid State Physics* at the Institute of Solid State Physics is engaged in the research on nanostructures, solid surfaces and thin films of both organic and inorganic semiconductor materials.

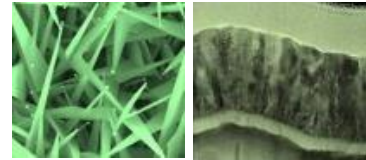
Our main research interest lays in the discovery of structure-property-relations of structurally well defined ultrathin epitaxial layers, organic quantum wells, K-doped organic super conductors, and carbon nanotubes. The main target of our research is the development of basic principles for the use of nano materials in prospective devices.

For the analyses of the chemical composition and bonding at surfaces and in thin films we use surface analysis methods like photoelectron spectroscopy (XPS, UPS) and Auger electron spectroscopy (AES). The crystalline structure can be determined by electron diffraction (LEED, RHEED, XPD, and electron channeling). Scanning tunneling microscopy (STM), atomic force microscopy (AFM) and scanning electron microscopy (SEM) are used for high-resolution imaging of nanostructures and surfaces. Electronic states are accessible via UPS, ARUPS and STS, the latter at low temperatures down to 1.1 K.

Our *in situ* optical spectroscopy, namely differential reflectance spectroscopy (DRS) is used to study organic (sub-)monolayers and heterostructures in terms of absorption spectroscopy to analyse the optical interaction between either the molecules itself, organic adsorbates and inorganic substrates, or molecules and dopants.

Experimental Physics / Solid State Physics

Prof. Dr. Carsten Ronning



- Synthesis, doping and functionization of semiconductor nanowires
- Photovoltaics
- Atomic structure and band-gap of complex semiconductors
- Modification and functionaization of phase change materials
- Growth and functionalization of diamond-like materials
- Semiconductor physics: doping using ion beams

Recent work of the research group *Experimental Physics / Solid State Physics* in the field of semiconductor nanowires focuses both on the growth of desired nanostructures as well as on the modification of semiconductor nanowires using ion beams for the use as photonic and electronic devices. This includes the realization of light-emitting diodes, single photon emitters, sensors for bio and chemical applications, and the observation of laser oscillations within single nanowires. Another scientific area of the group is the investigation and manipulation of phase change materials and devices using ion beams in order to create novel metamaterials and meta-surfaces. Furthermore, the group works on the basic mechanism of ion–nanostructure–interactions: here, the different accelerator systems are used for detailed investigations of the sputter yield of nanoparticles and nanowires, as well as their dynamic changes on morphology and stoichiometry upon high ion fluence irradiations.

The research on photovoltaics is mainly directed to the synthesis and analysis of $\text{Cu}(\text{In,Ga})(\text{Se,S})_2$ based thin film solar cells (CIGS). The research aims at a better understanding of the materials science of the CIGS chalcopyrite semiconductors and the improvement of existing cell concepts. To this end, a complete baseline on a form factor of $10 \times 10 \text{ cm}^2$ is available at the institute. Most important, we developed a high expertise in a comprehensive characterization of the structural, electrical and optical properties of CIGS solar cells. Besides standard tools, such as XRD, PL, CL, IV, we also use sophisticated synchrotron based characterization methods (EXAFS, XRF) or advanced electrical instruments (TAS, DLTS, etc.).

Low Temperature Physics



Prof. Dr. Paul Seidel

- Superconductivity within thin layers and layer systems
- Josephson effects, proximity effect, and tunnel effects in superconducting devices
- DC-SQUID's and their application in measurements, e.g. CCC, MRX
- cryogenic measurements of mechanical quality factor and optical properties
- Dynamics of superconducting Josephson arrays
- cryogenic engineering (cryocoolers, cryogenic storage, cryostates)

The *Low Temperature Physics* group works on the following fields:

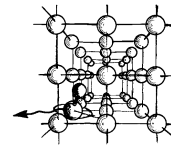
- preparation, characterization, modelling and application of Josephson junctions and SQUIDs (high precision and magneto-relaxation measurements with LTS SQUIDs, development of HTS SQUIDs, intrinsic Josephson junctions and Josephson junctions with iron based superconductors)
- low temperature physics and cryogenic engineering (development of new kinds of pulse tube cryocoolers, low loss cryostats and cryogenic storage, cryogenic current comparator CCC for particle accelerator beam analysis)
- experimental work on cryogenic measurements of the Q-factor and of optical properties of components for future gravitational wave detectors like the Einstein Telescope
- thin film technologies for insulators and other materials
- alternative preparation and properties of crystalline gold nanoclusters

The research is carried out in cooperation with other research groups in Thuringia (TU Ilmenau, Leibniz Institute IPHT Jena, SUPRACON Jena, Innovent e.V. Jena, Helmholtz Institute Jena). Within common activities the group works together with the Gesellschaft für Schwerionenforschung (GSI) Darmstadt, DESY Hamburg, MPI Heidelberg, IFW Dresden and the DLR Bremen.

Several research activities exist with industrial partners e.g. with the TransMIT center for adaptive cryotechniques Gießen. A long tradition of cooperation with the the Universities of Moscow and Dubna (Russia), Bratislava (Slovak Republic), Kharkov and Donetsk (Ukraine), Glasgow (U.K.), Poznan (Poland), Padua, Torino and Florence (Italy), Twente (Netherlands) and the Universities of Osaka, Tokyo and Nagoya (Japan) is also remarkable.

Ion Beam Physics

Prof. Dr. Elke Wendler



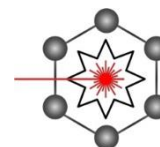
- Modification of solids by ion implantation and subsequent processes
- Ion beam analysis (RBS, PIXE, ERD, NRA)
- Ion beam synthesis of buried nanostructures
- Investigation of damage formation and amorphisation of covalent-ionic materials

The *Ion Beam Physics* group deals with modification of solids and synthesis of buried nanostructures using ion beams and combined secondary processes. The studies cover fundamental processes of ion-beam induced structural modification in semiconductors and insulators being relevant for future electronic, optoelectronic and photonic device technologies.

Classical group IV and III-V semiconductors are continuously investigated for relating ion-beam induced damage formation to the primary energies deposited in electronic and nuclear processes. This is important for predicting kind and concentration of damage to be expected for given irradiation conditions. Additionally oxidic semiconductors are in the focus of our research, which are important for the field of transparent electronics.

Our research on new materials and new research topics is connected with a continuous development of the ion beam analysis. This comprises both the experimental technique and the extended and combined use of the various ion beam analysis methods.

Laboratory Astrophysics / Cluster Physics



Dr. Cornelia Jäger

- Electronic spectroscopy of neutral and ionized polycyclic aromatic hydrocarbons (PAHs) in supersonic jets and cryogenic matrices
- Study of astrochemically relevant reactions in liquid helium nanodroplets
- Condensation and growth of cosmic dust at low temperature and pressure
- Gas-phase condensation processes of cosmic dust nanoparticles at high temperatures in circumstellar environments
- Study of chemical and structural processing of cosmic dust grains and astrophysically relevant molecules by UV photons and ion bombardment
- Chemical reactions and processing at the interface between dust and molecular ices

The *Laboratory Astrophysics and Cluster Physics Group* at the Institute of Solid State Physics results from a cooperation between the Max Planck Institute for Astronomy, Heidelberg, and the Friedrich Schiller University, Jena. Inaugurated in February 2003, it is now conducted by Prof. Dr. Thomas Henning and Dr. Cornelia Jäger.

The research of our group is devoted to fundamental astrophysical questions that can be answered by laboratory experiments, with particular emphasis on spectroscopy. The electromagnetic radiation reaching us from stellar objects is modified in a characteristic manner by interstellar molecules and dust particles. Many of these “fingerprints” are still far from being understood. In order to determine the species causing the modification of the electromagnetic signals detected by telescopes and satellites, and to understand global cosmic processes, comprehensive laboratory studies are urgently needed.

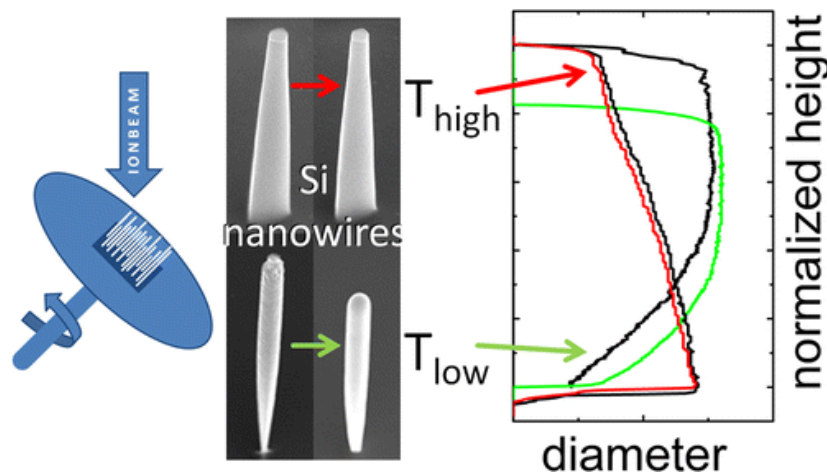
In our laboratory, we study the condensation, processing, and spectral properties of carbonaceous and siliceous dust grains and astrophysically relevant molecules that may play a role as progenitors of grain formation. Laboratory astrophysics is an interdisciplinary field whose research profits from sophisticated experimental facilities. We are able to simulate astrophysically relevant processes such as gas-phase condensation of grains and molecules by laser-induced pyrolysis of hydrocarbons or laser ablation of solids in the laboratory. Interesting molecules, clusters, and nanoparticles are prepared in vacuum chambers under conditions coming close to those in interstellar or circumstellar environments (low pressures and definite temperature ranges from around 10 K up to more than 2000 K). Sophisticated analytical tools comprising optical and IR spectroscopy, mass spectrometry, chromatography, and electron microscopy help us to characterise the composition and structure of the laboratory analogs of dust and complex molecules.

2. Current Research Projects

2.1 Important Results

Important results of the research group of **Prof. Dr. Carsten Ronning** obtained in 2015 included:

- Discovery of anomalous Plastic Deformation of Ion Irradiated Silicon Nanowires
- Determination of the nature of AX Centers in Sb-Doped Cadmium Telluride Nanobelts
- Observation of Enhanced sputter yields of ion irradiated Au nano particles
- Realization of phonon-assisted lasing in ZnO microwires at room temperature
- Measurements of the ultrafast dynamics of lasing semiconductor nanowires
- Understanding from atomic-scale structure to bandgap bowing for compound semiconductor alloys
- Determination of spatial variations in the chemical composition of CIGS thin film solar cells using high resolution X-ray fluorescence

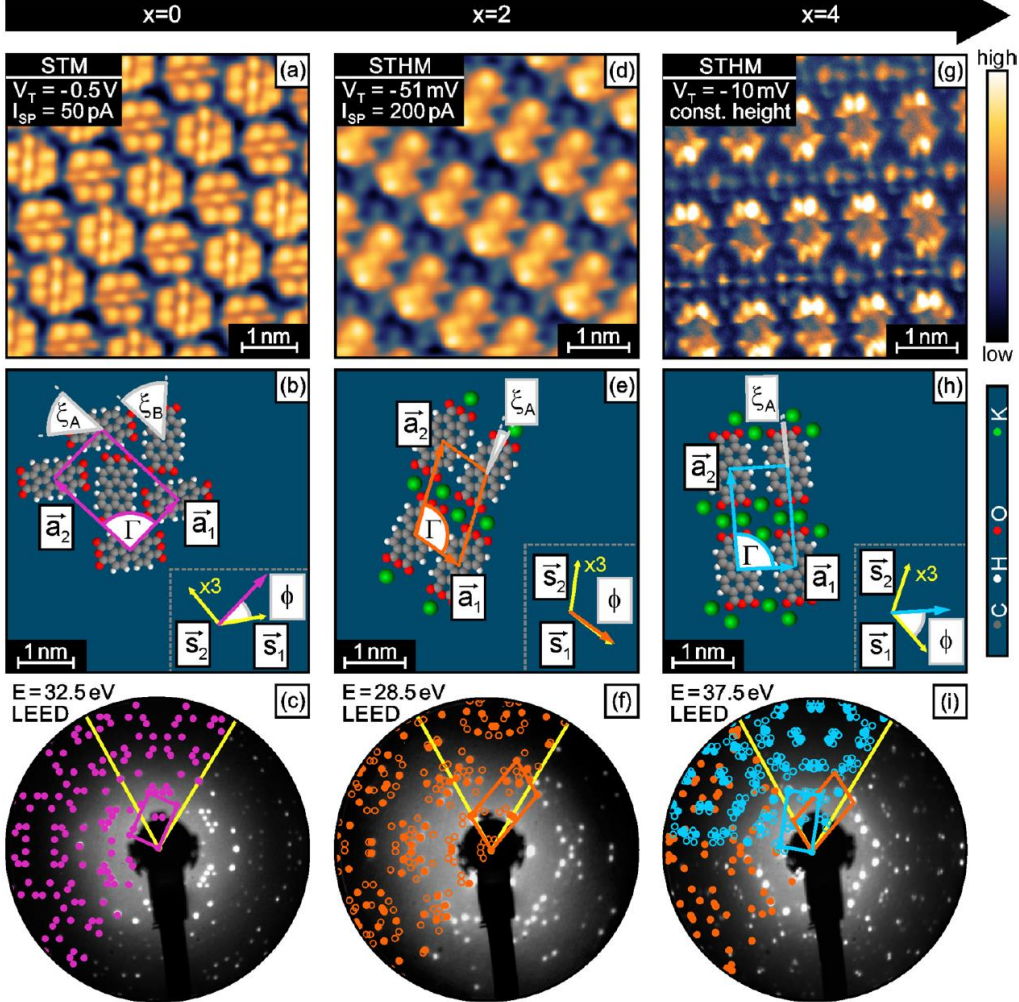


Anomalous Plastic Deformation and Sputtering of Ion Irradiated Silicon Nanowires. Silicon nanowires of various diameters were irradiated with 100 keV and 300 keV Ar⁺ ions on a rotatable and heatable stage. Irradiation at elevated temperatures above 300 °C retains the geometry of the nanostructure and sputtering can be gauged accurately. The diameter dependence of the sputtering shows a maximum if the ion range matches the nanowire diameter, which is in good agreement with Monte Carlo simulations based on binary collisions. Nanowires irradiated at room temperature, however, amorphize and deform plastically. So far, plastic deformation has not been observed in bulk silicon at such low ion energies. The magnitude and direction of the deformation is independent of the ion-beam direction and cannot be explained with mass-transport in a binary collision cascade but only by collective movement of atoms in the collision cascade with the given boundary conditions of a high surface to volume ratio.

Important results of the research of the group of **Prof. Dr. Torsten Fritz** obtained in 2015 included:

- Theoretical and experimental investigation of the charge transfer and the hybridization at an organic semiconductor / conductive oxide interface
- Discovery of several commensurate structures at electronically weakly interacting phthalocyanine/PTCDA heterointerfaces
- Identification of vibrational excitations and optical transitions of the organic electron donor tetraphenyldibenzoperiflanthene (DBP)
- Elucidation of the Complex Stoichiometry Dependent Reordering of 3,4,9,10-Perylene-tetracarboxylic dianhydride on Ag(111) upon K intercalation

Stoichiometry x of the system $K_x\text{PTCDA}$

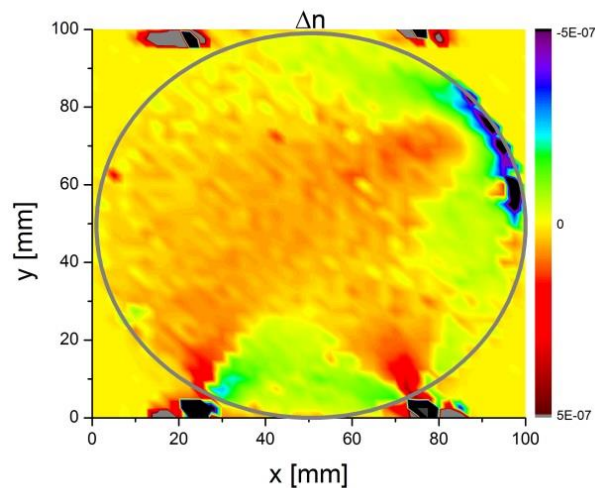


Self-assembled structures of distinct $K_x\text{PTCDA}$ phases on $\text{Ag}(111)$ for $x = 0, 2,$ and 4 . (a), (b), and (c) show the STM image, structural model, and LEED image of pristine $\text{PTCDA}/\text{Ag}(111)$. STHM images associated with $x = 2$ (d) and $x = 4$ (g) exhibit features originating from both K and PTCDA . Note that the determination of the unit cell compositions, especially for $x = 4$, is not straightforward and relies on the comparison with DFT calculations. The deduced structural models are depicted for $x = 2$ (e) and $x = 4$ (h). In each LEED image (c), (f), and (i), the simulated reciprocal unit cell of the associated $K_x\text{PTCDA}$ structure ($x = 0$ purple, $x = 2$ orange, and $x = 4$ blue) and the silver surface orientation along (01) and (10) (yellow) are superimposed. All possible rotational and mirror domains are considered for the simulation, and when taking multiple scattering into account (open circles), all visible spots are consistent with the model and none remain unidentified. The LEED image shown in (i) belongs to a substrate area simultaneously exhibiting domains corresponding to $x = 2$ and $x = 4$. Displayed quantities: V_T bias voltage; I_{SP} tunneling current; E beam energy; \vec{a}_1, \vec{a}_2 adsorbate lattice vectors; $\Gamma = \angle(\vec{a}_1, \vec{a}_2)$ adsorbate unit cell angle; \vec{s}_1, \vec{s}_2 substrate lattice vectors with unit cell angle of 120° ; $\phi = \angle(\vec{s}_1, \vec{a}_1)$ domain angle; $\zeta_{(A/B)} = (\vec{a}_2, \vec{m}_{(A/B)})$ orientation of molecules A and B in the unit cell.

Important results of the research group of **Prof. Dr. Paul Seidel** obtained in 2015 included:

- Measurement of the stress induced birefringence in silicon at both cryogenic and room temperature and its correlation with crystal defects
- Different kinds of Josephson junctions with one or two pnictide electrodes in thin film technology as well as using a pnictide single crystal for basis electrode with high $I_C R_N$ products

- Modification of structural and superconducting / optical properties of thin high- T_c / STO films with selforganised grown Au-nanoparticles



Measurement of the stress-induced birefringence of a silicon test mass sample for a future gravitational wave detector. Using a special developed polarimeter it was possible to identify intrinsic stress-fields in the silicon sample and distinguish them from gravity induced fields (stress pattern arising from the mechanical support of the sample at the lower part of the figure).

Important results of the research group of **Prof. Dr. Elke Wendler** obtained in 2015 included:

- Successful application of ion beam analysis for quantifying the oxygen and carbon content in silicon based solar cell structures
- Clear proof of Nb atoms occupying free octahedron places in ion implanted LiNbO_3 which results in higher defect visibility in z-direction than in x-direction

Important results of the research the group of **Dr. Cornelia Jäger** obtained in 2015 included:

- Photoelectron photoion coincidence spectroscopy was used to measure the dissociative photoionization, adiabatic ionization energy, and the appearance energy of fragment ions of ethynyl-substituted PAHs. The stability of ethynyl-substituted PAH molecules upon photoionization was calculated. This group of PAH derivatives was found to be as photostable as the non-substituted species in regions of ionized hydrogen and may play an important role in the growth of interstellar PAH molecules.
- The ion-induced erosion of carbonaceous grains at the interface between oxygen-bearing ices and solid carbon combined with an additional formation of CO and CO_2 in the ice layers at 10K has been observed for the first time. Carbon erosion rates upon proton bombardment were quantitatively measured. In addition, the solid carbon material beneath the ice layer was structurally modified, which has strong consequences on the spectral properties of the remaining dust.
- The R2PI spectra of Al atoms solvated in helium droplets reveal vibrational progressions, which are assigned to Al-He_n vibrations. These vibrations suggest a relatively strong interaction between Al atoms in their excited state and the helium. The presented data do not provide evidence in favor of the formation of regular Al clusters or the formation of an aluminum foam in helium droplets.

2.2 Third Party Grants

DFG projects

Dotierte aromatische Dünnschichten mit supraleitenden Eigenschaften

(FO 770/2-1)

Time span: 09/14 – 08/17

Formation and shaping of magnetic nanoclusters in oxides, using ion implantation

Time span: 03/11 – 02/15

Research unit FOR1616: Dynamics and Interactions of Semiconductor Nanowires for Optoelectronics

Time span: 03/12 – 06/15

Time span: 08/15 – 08/18

Teilprojekt P4: Light-matter interaction in optically doped nanowire LEDs and nano lasers

Time span: 03/12 – 11/15

Time span: 08/15 – 08/18

Josephson effects at iron pnictides - phase-sensitive experiments (SE 664/15-2)

Time span: 10/13 – 09/16

Experimental and theoretical studies of charge transport in heterostructures based on two-band superconductors and/or ferromagnetic metals (SE 664/18-1)

Time span: 11/13 – 12/15

Experimental studies of the low-temperature condensation of cosmic dust in the interstellar medium (HE 1935/26-1) (1. Tranche of the SPP 1378) (financial management by the MPIA)

Time span: 02/12 – 01/15

Experimental studies of the low-temperature condensation of cosmic dust in the interstellar medium (JA 2107/2-2) (2. Tranche of the SPP 1378)

Time span: 10/14 – 09/17

Kohlenwasserstoff-Chemie bei ultratiefen Temperaturen in flüssigen Helium-Tröpfchen (HU 474/22-3)

Time span: 05/12 – 05/15

Optical properties and photostability of ice-silicate-carbon mixtures in stellar UV fields (JA 2107/3-1) TP8 of the Research Group 'Debris disks in planetary systems'

Time span: 12/15 – 12/18

Experimental studies on the diamond formation in astrophysical environments (JA 2107/4-1)

Time span: 11/15 – 10/18

BMBF-, BMU- and BMWi-projects

Verbundvorhaben: Grenzflächen und Defekte – Rechnerunterstützte Optimierung des Wirkungsgrades von CIGS Dünnschichtsolarzellen in der industriellen Umsetzung
Teilvorhaben: Ermittlung von Struktur-Eigenschaftsbeziehungen und ihre Beeinflussung durch Variation der Prozessparameter

Time span: 08/12 – 02/16

Neuartige Verbundmaterialien u. Fertigungstechnologien für Kryostate zur see- u. luftgestützten Rohstoff- und Umwelterkundung (MAKSEL)

Time span: 09/14 – 12/17

Phase dynamics of intrinsic Josephson junctions and superconducting quantum interference devices (Heisenberg-Landau Programm)

Time span: 01/15 – 12/15

ET R&D – Networking and R&D for the Einstein Telescope (3rd common ASPERA call)

Time span: 03/13 – 02/16

Verbundprojekt 05P2015 - R&D Beschleuniger (CCC): Entwicklung, Sensoroptimierungen und Tests von Kryogenen Stromkomparatoren zum Einsatz an neuartigen Ionenquellen, Beschleunigeranlagen und Speicherringen

Time span 07/15 - 06/18

Cryogenic Current Comparator SQUID-Cartdidge

Time span: 02/15 – 04/15

Anfertigung eines CCC (Optimierung des Gerätes)

Time span: 09/15 – 08/16

Komplexe Metalloxide als effiziente und stabile Komponenten für die Solare Wasserstofferzeugung

Verbundprojekt „Metalloxid-4-Hydrogen“

Time span: 09/14 – 08/17

Other projects

Nanoscale Interfaces for Organic Electronics (DAAD PaJaKo Project Japan, ID 56264880)

Time span: 01/13 – 12/15

Virtuelles Institut „MEMRIOX“ (HZDR Dresden-Rossendorf)

Memory Effects in Resistive Ion-beam Modified Oxides

Time span: 10/11 – 09/16

Switchable and tunable infrared devices by controlled manipulation of the insulator-to-metal transition in Vanadium dioxide (DAAD/PPP USA)

Time span: 01/14 – 12/15

Schwingungsdynamik in komplexen Verbindungshalbleitern (ProChance, FSU Jena)

Time span: 03/13 – 12/16

FP7-PEOPLE-IRSES Scientist Exchange Program „ELiTES“

Time span: 03/12 – 02/17

3. Publications, Invited Talks, and Theses

3.1 Publications in Scientific Journals

Nanocluster formation in Co/Fe implanted ZnO

K. Bharuth-Ram, H. Masenda, T. B. Doyle, S. Geburt, C. Ronning
Hyperfine Interactions **230**, 181 (2015)

Stoichiometry variation for the atomic layer deposition of $Sr_xTi_yO_z$ from $Sr(iPr_3Cp)_2$, $Ti[N(CH_3)_2]_4$ and H_2O

S. Rentrop, S. Abendroth, J. Walter, J. Rensberg, W. Münchgesang, R. Strohmeyer, H. Stöcker, C. Ronning, S. Gemming, D.C. Meyer
Thin Solid Films **577**, 134 (2015)

Nature of AX Centers in Antimony Doped Cadmium Telluride Nanobelts

L. Huang, C.-C. Lin, M. Riediger, R. Röder, P. L. Tse, C. Ronning, G. Lu
Nano Letters **15**, 974 (2015)

ZnO/porous-Si and TiO₂/porous-Si nanocomposite nanopillars

D. Wang, Y. Yan, P. Schaaf, T. Sharp, S. Schönherr, C. Ronning, R. Ji
Journal of Vacuum Science and Technology **A 33**, 01A102 (2015)

Adjusting the forming step for resistive switching in Nb₂O₅ by ion irradiation

H. Wylezich, H. Mähne, A. Heinrich, S. Slesazeck, J. Rensberg, C. Ronning, P. Zahn, T. Mikolajick
Journal of Vacuum Science and Technology **B 33**, 01A105 (2015)

Corrigendum: Enhanced sputtering and incorporation of Mn in implanted GaAs and ZnO nanowires

A. Johannes, S. Noack, W. Paschoal Jr, S. Kumar, D. Jacobsson, H. Pettersson, L. Samuelson, K. A. Dick, G. Martinez-Criado, M. Burghammer
J. Phys. D: Appl. Phys. **48**, 079501 (2015)

Corrigendum: Polarization features of optically pumped CdS nanowire lasers

R. Röder, D. Ploss, A. Kriesch, R. Buschlinger, S. Geburt, U. Peschel and C. Ronning
J. Phys. D: Appl. Phys. **48**, 239501 (2015)

Ion beam irradiation of nanostructures: sputtering, dopant incorporation and dynamic annealing

A. Johannes, H. Holland-Moritz, C. Ronning
Semiconductor Science and Technology **30**, 033001 (2015)

Anomalous plastic deformation and sputtering of ion irradiated silicon nanowires

A. Johannes, S. Noack, W. Wesch, A. Lugstein, M. Glaser, C. Ronning
Nano Letters **15**, 3800 (2015)

Ultrafast dynamics of lasing semiconductor nanowires

R. Röder, T.P.H. Sidiropoulos, C. Tessarek, S. Christiansen, R.F. Oulton, C. Ronning
Nano Letters **15**, 4638 (2015)

Enhanced sputter yields of ion irradiated Au nano particles: energy and size dependence

H. Holland-Moritz, S. Scheeler, C. Stanglmair, C. Pacholski, C. Ronning
Nanotechnology **26**, 325301 (2015)

Improved Ga grading of sequentially produced Cu(In,Ga)Se₂ solar cells studied by high resolution X-ray fluorescence

P. Schöppe, Claudia S. Schnohr, M. Oertel, A. Kusch, A. Johannes, S. Eckner, M. Burghammer, G. Martínez-Criado, U. Reislöhner, C. Ronning
Appl. Phys. Lett. **106**, 013909 (2015)

Dynamics of the phase formation process upon the low temperature selenization of Cu/In-multilayer stacks

M. Oertel, C. Ronning
J. Appl. Phys. **117**, 105302 (2015)

Compound semiconductor alloys: From atomic-scale structure to bandgap bowing

C.S. Schnohr
Appl. Phys. Rev. **2**, 031304 (2015)

Composition-dependent nanostructure of Cu(In,Ga)Se₂ powders and thin films

C. S. Schnohr, H. Kämmer, T. Steinbach, M. Gnauck, T. Rissom, C. A. Kaufmann, C. Stephan, S. Schorr
Thin Solid Films **582**, 356 (2015)

Principal processes of organic-inorganic hybrid solar cells using the example of ZnPc with ZnO

M. Kozlik, R. Forker and T. Fritz
Phys. Status Solidi A: Applications and Materials Science **212**, 554–560 (2015).

Charge Transfer and Hybridization at an Organic Semiconductor / Conductive Oxide Interface

M. Gruenewald, L. K. Schirra, P. Winget, M. Kozlik, P.F. Ndione, A.K. Sigdel, D.S. Ginley, J.J. Berry, J. Shim, H. Kim, B. Kippelen, R. Forker, J.-L. Bredas, T. Fritz and O.L.A. Monti
J. Phys. Chem. C **119** (9), 4865–4873 (2015).

Commensurism at electronically weakly interacting phthalocyanine/PTCDA heterointerfaces

M. Gruenewald, C. Sauer, J. Peuker, M. Meissner, F. Sojka, A. Schöll, F. Reinert, R. Forker and T. Fritz
Phys. Rev. B. **91**, 155432 (2015).

Growth of coronene on (100)- and (111)-surfaces of fcc-crystals

T. Hümpfner, F. Sojka, R. Forker and T. Fritz
Surf. Sci. **639**, 80-99 (2015).

Comment on “Calculating Optical Absorption Spectra of Thin Polycrystalline Organic Films: Structural Disorder and Site-Dependent van der Waals Interaction

R. Forker and T. Fritz
J. Phys. Chem. C **119** (32), 18816-18817 (2015).

Identification of vibrational excitations and optical transitions of the organic electron donor tetraphenyldibenzoperiflanthene (DBP)

G. Rouillé, T. Kirchhübel, M. Rink, M. Gruenewald, J. Kröger, R. Forker and T. Fritz
Phys. Chem. Chem. Phys. **17**, 30404-30416 (2015).

Complex Stoichiometry Dependent Reordering of 3,4,9,10-Perylenetetracarboxylic Dianhydride on Ag(111) upon K Intercalation

C. Zwick, A. Baby, M. Gruenewald, O. T. Hofmann, R. Forker, G. Fratesi, G. P. Brivio, E. Zojer and T. Fritz
ACS Nano (2015).

Measurement of the mechanical loss of prototype GaP/AlGaP crystalline coatings for future gravitational wave detectors

A. Cumming, K. Craig, I. Martin, R. Bassiri, L. Cunningham, M. Fejer, J. Harris, K. Haughian, D. Heinert, B. Lantz, A. Lin, A. Markosyan, R. Nawrodt, R. Route, S. Rowan
Class. Quantum Grav. **32**, 035002 (2015)

Hybrid Josephson Junctions with Iron-based and Conventional Superconductor Electrodes

S. Döring, S. Schmidt, D. Reifert, M. Feltz, M. Monecke, N. Hasan · V. Tympel, F. Schmidl, J. Engelmann, F. Kurth, K. Iida, I. Mönch, B. Holzapfel, P. Seidel
J. Supercond. Nov. Magn. **28**, 1117 (2015)

Low-temperature mechanical dissipation of thermal evaporated indium film

P. G. Murray, I. W. Martin, L. Cunningham, K. Craig, G. D. Hammond, J. Hough, R. Nawrodt, G. Hofmann, D. Reifert, S. Rowan
Class. Quantum Grav. **32**, 115014 (2015)

Formation and Characterization of Silver Nanoparticles Embedded in Optical Transparent Materials for Preparation of Plasmonic Sensor Surfaces

G. Schmidl, J. Dellith, H. Schneidewind, D. Zopf, O. Stranik, A. Gawlik, S. Anders, V. Tympel, Chr. Katzer, F. Schmidl, W. Fritzsche
Materials Science and Engineering B **193**, 207 (2015)

Tracing the evolution of the two energy gaps in magnesium diboride under pressure

V. Kononenko, V. Tarenkov, M. Belogolovskii, S. Döring, S. Schmidt, P. Seidel
Low Temperature Physics **41**, 343 (2015)

A SQUID-based beam current monitor for FAIR / CRYRING

R. Geithner, F. Kurian, H.-J. Reeg, M. Schwickert, R. Neubert, P. Seidel, T. Stoehlker
Phys. Scr. T **166**, 014057 (2015)

Crystallographic investigation of Au nanoparticles embedded in a SrTiO₃ thin film for plasmonics applications by means of synchrotron radiation

D. Pincini, C. Mazzoli, H. Bernhardt, C. Katzer, F. Schmidl, I. Uschmann, C. Detlefs
Journal of Applied Physics **117**, 105305 (2015)

Characterization of self-organized crystalline Au nano-particles embedded in epitaxially grown SrTiO₃

H. Bernhardt, C. Katzer, A. Undisz, M. Drüe, M. Rettenmayr, I. Uschmann, F. Schmidl
Journal of Materials Research **30**, 973 (2015)

The Einstein Telescope

S. Kroker, R. Nawrodt
IEEE Instrumentation & Measurement Magazine **18**, 4 (2015)

Electron backscatter diffraction analysis of gold nanoparticles on YBa₂Cu₃O_{7- δ}

A. Bochmann, C. Katzer, F. Schmidl, S. Teichert
J. Appl. Phys. **117**, 215306 (2015)

Engineering crystalline Au nanoparticles of anisotropic shape in epitaxially grown high index SrTiO₃

H. Bernhardt, R. Diener, P. Sungur, C. Katzer, G. Schmidl, W. Fritzsche, F. Schmidl
J. Mater. Sci. **50**, 5562 (2015)

Superconductivity, role of pnictogen, and Fe substitution in 112-LaPdxPn2 (Pn = Sb, Bi)
R. Retzlaff, A. Buckow, P. Komissinskiy, S. Ray, S. Schmidt, H. Mühlig, F. Schmidl, P. Seidel, J. Kurian, L. Alff
Phys. Rev. B **91**, 104519 (2015)

Effects of LC shunting on the Shapiro steps features of Josephson junction
Yu. M. Shukrinov, I.R. Rahmonov, K.V. Kulikov, P. Seidel
EPL **110**, 47001 (2015)

Excess currents in planar Ba(Fe_{1-x}Cox)₂As₂/TiO_x/Pb Josephson junctions
S. Döring, D. Reifert, N. Hasan, S. Schmidt, F. Schmidl, V. Tympel, F. Kurth, K. Iida, B. Holzapfel, T. Wolf, P. Seidel
Physica Status Solidi B **252**, 2858 (2015)

Optical Characterization of YBa₂Cu₃O_{7-δ} Thin Film Modified Gold Nanoparticles
P. Naujok, C. Katzer, G. Schmidl, J. Jatschka, W. Fritzsche, F. Schmidl
Appl. Surf. Sci. **357**, 340 (2015)

Indium joints for cryogenic gravitational wave detectors
G. Hofmann, D. Chen, G. Bergmann, G. D. Hammond, M. Hanke, K. Haughian, D. Heinert, J. Hough, A. Khalaidovski, J. Komma, H. Lück, E. Majorana, M. Masso Reid, P. G. Murray, L. Naticchioni, R. Nawrodt, S. Reid, S. Rowan, F. Schmidl, C. Schwarz, P. Seidel, T. Suzuki, T. Tomaru, D. vine, K. Yamamoto
Class. Quantum Grav. **32**, 245013 (2015)

Dissociative photoionization of polycyclic aromatic hydrocarbon molecules carrying an ethynyl group
G. Rouillé, S. A. Krasnokutski, D. Fulvio, C. Jäger, Th. Henning, G. A. Garcia, X.-F. Tang, and L. Nahon
Astrophys. J. **810**, 114 (2015)

Toward laser-induced vibrational emission spectroscopy of C₆₀⁺
S. Kumar Sudhakaran, P. Bizenberger, K. Blaum, C. Breitenfeldt, J. Göck, U. Grözinger, Th. Henning, J. Karthein, B. Kern, C. Meyer, G. Rouillé, D. Strelnikov, A. Wolf, S. George, and H. Kreckel in Proceedings of the XXIX International Conference on Photonic, Electronic, and Atomic Collisions (ICPEAC2015), eds. C. Díaz, I. Rabadán, G. García, L. Méndez, and F. Martín,
J. Phys. Conf. Ser. **635**, 112072 (2015)

Luminescence spectroscopical properties of plagioclase particles from Hayabusa sample return mission
A. Gucsik, H. Nishido, K. Ninagawa, A. Kereszturi, T. Nakamura, A. Tsuchiyama, C. Jäger, U. Ott, and M. Kayama in Lunar and Planetary Science Conference XLVI,
LPI Contribution Series **1832**, 2931 (2015)

Cathodoluminescence microscopy and spectroscopy of forsterite from the Tagish lake meteorite: An implication for asteroidal processes
A. Gucsik, H. Nishido, K. Ninagawa, I. Gyollai, M. Izawa, C. Jäger, U. Ott, and M. Kayama in Lunar and Planetary Science Conference XLVI
LPI Contribution Series **1832**, 2117 (2015)

Cosmic Dust VII

H. Kimura, L. Kolokolova, A. Li, J.-C. Augereau, H. Kaneda, and C. Jäger:,
Planet. Space Sci. **116**, 1 (2015)

Toward the formation of carbonaceous refractory matter in high temperature hydrocarbon-rich atmospheres of exoplanets upon micrometeoroid impact,

B. B. Dangi, Y. S. Kim, S. A. Krasnokutski, R. I. Kaiser, and C. W. Bauschlicher Jr:
Astrophys. J. **805**, 76 (2015)

Cathodoluminescence spectroscopical properties of plagioclase particles from asteroid Itokawa: An implication for the luminescence-based astromineralogy

A. Gucsik, H. Nishido, K. Ninagawa, A. Kereszturi, T. Nakamura, A. Tsuchiyama, C. Jäger, U. Ott, and M. Kayama
Adv. ESR Appl. **31**, 6 (2015)

Photoluminescence properties of silicon nanocrystals interacting with gold nanoparticles via exciton-plasmon coupling

K. Potrick and F. Huisken
Phys. Rev. B **91**, 125306 (2015)

Resonant two-photon ionization spectroscopy of Al atoms and dimers solvated in helium nanodroplets

S. A. Krasnokutski and F. Huisken
J. Chem. Phys. **142**, 084311 (2015)

A laboratory study of ion-induced erosion of ice-covered carbon grains

T. Sabri, G. A. Baratta, C. Jäger, M. E. Palumbo, T. Henning, G. Strazzulla, and E. Wendler:,
Astron. Astrophys. **575**, A76 (2015)

UV-vis gas-phase absorption spectroscopy of PAHs,

in Laboratory Astrochemistry - From Molecules through Nanoparticles to Grains

Y. Carpentier, G. Rouillé, M. Steglich, C. Jäger, Th. Henning, and F. Huisken, eds. by S. Schlemmer, Th. Giesen, H. Mutschke, and C. Jäger,
Wiley-VCH, Weinheim, p29-49, (2015)

Spectroscopic properties of carbon compounds

in Laboratory Astrochemistry - From Molecules through Nanoparticles to Grains

H. Mutschke and C. Jäger, eds. by S. Schlemmer, Th. Giesen, H. Mutschke, and C. Jäger,
Wiley-VCH, Weinheim, p385-397, (2015)

Photoluminescence studies of silicon-based nanoparticles

in Laboratory Astrochemistry - From Molecules through Nanoparticles to Grains

F. Huisken, O. Guillois, O. Debieu, K. Potrick, and T. Schmidt, eds. by S. Schlemmer, Th. Giesen, H. Mutschke, and C. Jäger,
Wiley-VCH, Weinheim, p397- 408, (2015)

Laboratory approach to gas-phase condensation of particles

in Laboratory Astrochemistry - From Molecules through Nanoparticles to Grains

C. Jäger
Wiley-VCH, Weinheim, p 447- 455, (2015)

Gas-phase condensation of carbonaceous particles in the laboratory

in Laboratory Astrochemistry - From Molecules through Nanoparticles to Grains

C. Jäger and H. Mutschke,
Wiley-VCH, Weinheim, p 467- 477, (2015)

Processing of silicates

in Laboratory Astrochemistry - From Molecules through Nanoparticles to Grains

C. Jäger

Wiley-VCH, Weinheim, p 477- 483, (2015)

Indirect method to measure differential cross-sections for nuclear reaction analysis

A. Nathanael, E. Schmidt, W. Wesch, E. Wendler, E

Nucl. Instrum. Methods Phys. Res. B **345**, 37 (2015)

Comparison of silicon oxide and silicon carbide absorber materials in silicon thin-film solar cells

C. Walder, M. Kellermann, E. Wendler, J. Rensberg, K. von Maydell, C. Agert,

Comparison of silicon oxide and silicon carbide absorber materials in silicon thin-film solar cells

EPJ Photovoltaics **6**, 65302 (2015)

Scanning electron microscopy of the surfaces of ion implanted SiC

J.B. Malherbe, N.G. van der Berg, R.J. Kuhudzai, T.T. Hlatshwayo, T.T. Thabethe, O.S.

Oduemowo, C.C. Theron, E. Friedland, A.J. Botha, E. Wendler,

Nucl. Instrum. Methods Phys. Res. B **354**, 23 (2015)

Dynamic defect annealing in wurtzite MgZnO implanted with Ar ions

A. Yu. Azarov, E. Wendler, X.L. Du, A.Yu. Kuznetsov, B.G. Svensson,

Nucl. Instrum. Methods Phys. Res. B **358**, 16 (2015)

Analysis of the stability of InGaN/GaN multiquantum wells against ion beam intermixing

A. Redondo-Cubero, K. Lorenz, E. Wendler, S. Magalhaes, E. Alves, D. Carvalho, T. Ben,

F.M. Morales, R. Garcia, K.P. O'Donnell, C. Wetzel,

Nanotechnology **26**, 425703 (2015)

Defect-induced magnetism in SiC: Interplay between ferromagnetism and paramagnetism

Y.T. Wang, Y. Liu, E. Wendler, R. Hubner, W. Anwand, G. Wang, X.L. Chen, W. Tong, Z.R.

Yang, F. Munnik, G. Bukalis, X.L. Chen, S. Gemming, M. Helm, S.Q. Zhou,

Phys. Rev. B **92**, 174409 (2015)

Deep ultra violet and visible Raman spectroscopy studies of ion implanted 6H-SiC:

Recrystallisation behaviour and thermal decomposition/thermal etching of the near surface region

R.J. Kuhudzai, J.B. Malherbe, N.G. van der Berg, T.T. Hlatshwayo, A. Oduemowo, L.C.

Prinsloo, A.V. Buys, R. Erasmus, E. Wendler

Nucl. Instrum. Methods Phys. Res. B **365**, 342 (2015)

3.2 Invited Talks at Conferences and Colloquia

T. Fritz:

Incommensurate Growth and Static Distortion Waves in Organic-Inorganic Epitaxy

The 15th International Conference on the Formation of Semiconductor Interfaces (ICFSI-15)

Hiroshima (Japan), 19.11.2015

Incommensurate Growth and Static Distortion Waves in Organic-Inorganic Epitaxy

Electronic Structure and Processes at Molecular-Based Interfaces (ESPMI viii)

Biosphere 2 (USA), 14.10.2015

Epitaxial Organic Thin Films of Large Aromatic Hydrocarbons - Structure and Physical Properties

Department of Chemistry, University of Arizona, Tucson (USA), 02.10.2015

Incommensurate Growth and Static Distortion Waves in Organic-Inorganic Epitaxy

1st workshop on functional molecules

Izu-Kogen (Japan), 03.09.2015

Organic-Inorganic Epitaxy: Lattice Epitaxy vs. Incommensurate Growth

Department of Physics, Osaka University, Osaka (Japan), 27.08.2015

Incommensurate Growth and Static Distortion Waves in Organic-Inorganic Epitaxy

Department of Chemistry, Osaka University, Osaka (Japan), 06.08.2015

C. Ronning:

Ion-Nanostructure Interactions

The 19th International Conference on Surface Modification of Materials by Ion Beams (SMMIB-19), Chiang Mai, Thailand, 23. Nov. 2015

Semiconductor nanowire photonics

Ireland Photonics conference 2015, Cork, 03.09.2015

Ion beam doping of semiconductor nanowires

Seminar at TU Eindhoven, Netherlands, 01.09.2015

Semiconductor nanowire photonics

Seminar of the Department of Electrical Engineering at U Wisconsin, Madison, USA, 24.08.2015

Semiconductor nanowire photonics

Physikalisches Kolloquium, TU Ilmenau, 21.04.2015

P. Seidel:

Josephson effekte in eisenbasierten Supraleitern

Christian-Albrechts-Universität zu Kiel, 23.07.2015

SQUID-Sensorik für Teilchenbeschleuniger

Workshop "Zukunftsperspektiven supraleitender Anwendungen", Dresden, 31.08.2015

E. Wendler:

Primary Processes of Damage Formation in Ion Implanted Semiconductors

Leibniz-Institut für Oberflächenmodifizierung (IOM), Leipzig, 10.12.2015

R. Nawrodt:

Experimental Aspects of Gravitational Wave Detection

Astronomy from 4 perspectives, Jena, September 04, 2015

Materials for future gravitational wave detectors
Stanford University, USA, May 15, 2015

Materials for suspensions and test masses in a cryogenic detector
GWADW 2015, Girdwood/Alaska, USA, Mai 19, 2015

C. Jäger:

Current expectations concerning the interstellar PAH population
International Symposium on Polycyclic Aromatic Compounds, Session: Interstellar PAHs,
Bordeaux, 13-17 September 2015

Dust formation and processing in the ISM
International Workshop on Silicates in Space, Heidelberg, Kirchhoff-Institut für Physik
28. September – 01. October 2015

The Characteristics of Dust in Molecular Clouds
International Conference ‘From Clouds to Protoplanetary Disks: The Astrochemical Link,
Berlin, Germany, 5 – 8 October 2015

Laboratory experiments on the formation and processing of dust in astrophysical environments
Planet and Star-Formation Workshop of the Max Planck Institute for Astronomy, Ellwangen,
Germany, 26 – 28 October 2015

G. Rouillé:

Optical absorption spectroscopy on cold, isolated molecules
Seminar zur Oberflächenforschung, Institut für Physikalische und Theoretische Chemie,
Bonn, 16 January 2015

Polycyclic aromatic hydrocarbon molecules carrying an ethynyl group: Photostability in H I regions
Planet and Star-Formation Workshop of the Max Planck Institute for Astronomy, Ellwangen,
Germany, 26 – 28 October 2015

S. Krasnokutski:

Reaction between H₂ molecules and C atoms at ultra-low temperatures
Planet and Star-Formation Workshop of the Max Planck Institute for Astronomy, Ellwangen,
Germany, 26 – 28 October 2015

R. Forker:

Organic Epitaxial Interfaces
7th School on Organic Electronics
Lake Como School of Advanced Studies, 14-18.09.2015

3.3 Theses

(A) Bachelor Theses and Studienarbeiten

Paul Schenk	<i>Röntgendiffrakometrie an CIGS-Dünnschichtsolarzellen</i>
Adrian Weisskopf	<i>Scanning tunneling microscopy and spectroscopy of PbPc on graphite(0001)Diploma, Master and state examination theses</i>
Johannes Dickmann	<i>Mechanische Verluste von SiO₂-Schichten</i>
Johann Schwengber	<i>Untersuchungen zum Einfluss von Au-Nanopartikeln auf die kritische Stromdichte von YBCO-Schichten</i>
Lena Kath	<i>RBS-Untersuchungen an kristallinem LiNbO₃ in Zufallsrichtungen und ent-lang verschiedener Hauptachsen</i> Titel

(B) Diploma, Master Theses, and State Examination Theses

Sven Bauer	<i>Nanostrukturierung von Lithiumniobat mittels selbstorganisierter Nano-strukturmasken und Ionenstrahlen</i>
Markus Schwiderke	<i>Anregungs- und temperaturabhängige Lasingeigenschaften von Halbleiternanodrähten</i>
Michelle Geelen	<i>Ion beam doping and defect engineering of ZnO nanowires for photode-tection and sensing applications</i>
Max Riedieger	<i>Emissionscharakteristik von ZnO Nanodrahtlasern</i>
Tim Barth	<i>Wachstum und Charakterisierung von Vanadiumdioxid-Mikrodrähten</i>
Felix Otto	<i>Untersuchung der Kalium-Dotierung von Tetraphenyldibenzoperiflanthen (DBP) mittels Photoelektronenspektroskopie</i>
Ellen Butz	<i>Herstellung und Charakterisierung von Kaliumfluorid-behandelten Cu(In,Ga)Se₂-Solarzellen</i>
Erik Haubold	<i>Strukturanalyse kupferarmer Cu(In,Ga)Se Phasen mittels Röntgenabsorp-tionsspektroskopie</i>
Adebowale Anthony	<i>Structural and optical characterisation of Cu(In,Ga)Se₂ solar cells</i>
Jonas Gronemann	<i>Charakterisierung von Au-modifizierten Korngrenzen-Kontakten</i>
Marcus Junghanns	<i>PEDOT:PSS Emitter auf mc-Si Absorbern für Hybrid-Dünnschicht-Solarzellen</i>
Rene Glaser	<i>Untersuchungen zur Photoelastizität von Silizium</i>
Philip Pastrik	<i>Optische Untersuchungen an Materialien für zukünftige Gravitationswel-len-detektoren</i>
Martin Feltz	<i>Voruntersuchungen zur Realisierung eines Parker-Mazin-Designes auf Ba-122</i>
Lukas Maczewsky	<i>Mechanische Spektroskopie optischer Materialien für Gravitationswellendetektoren</i>

Valentin Biehl	<i>Aufbau und Charakterisierung eines Messsystems zur Detektion kleiner mechanischer Schwingungen</i>
Gregor Becker	<i>Defektuntersuchungen an ionenimplantiertem Lithiumniobat</i>
(C) PhD Theses	
Christoph Heisler	<i>Herstellung und Dotierung von polykristallinen CdTe-Dünnschichten für Solarzellen</i>
Andreas Johannes	<i>High fluenz ion beam irradiation of semiconductor nanowires</i>
Steffen Wolf	<i>Metallische Nanopartikel in Lithiumniobat für plasmonische Anwendungen</i>
Sebastian Döring	<i>Dünnschicht-Josephson-Kontakte zur Charakterisierung eisenbasierter Supraleiter</i>
Christian Katzer	<i>Gold Nanopartikel und deren Auswirkungen auf die physikalischen Eigenschaften dünner Schichten</i>

4. Cooperations, Visiting Scientists, and Colloquia at the IFK

4.1 Cooperations

The Institute of Solid State Physics collaborates with a large number of Institutes and Universities in Germany and around the world and has also close connections with several companies. In the framework of these wide spread contacts a large number of scientists from various countries visited our Institute in 2015 to perform experiments, discuss scientific results obtained within joint projects and to give talks in the colloquium of the Institute of Solid State Physics.

The Surface Science group of **Prof. Dr. T. Fritz** strengthened their international cooperations in 2015. The ongoing collaboration with the group of Prof. Dr. T. Munakata (University of Osaka) was continued and even intensified not only by numerous exchange visits (founded via a PaJaKo project of the DAAD) between Germany and Japan but also by awarding a prestigious Visiting Professorship at Osaka University to Prof. Fritz.. In the USA we cooperate with the groups of Prof. Dr. O. Monti and Prof. Dr. N.R. Armstrong (University of Arizona). Within Europe we have intensive collaborations with the theory groups of Prof. Dr. E. Zojer (Graz University of Technology) and Prof. Dr. G.-P. Brivio (Universita di Milano-Bicocca). In Germany our collaborations include the group of Prof. Dr. C. Kumpf (Forschungszentrum Jülich GmbH), Prof. Dr. J. Kröger (TU Ilmenau), and the University Würzburg (Profs. F. Reinert and A. Schöll).

The group of **Prof. Dr. C. Ronning** collaborated in 2015 with various international groups. Special situations have been established with the groups of Prof. Dr. F. Capasso (U Harvard), Prof. Dr. M. Kats (U Wisconsin), Prof. A. Lugstein (TU Vienna), Prof. A. Fontcuberta i Moral (EPF Lausanne), and Prof. K. Bharuth-Ram (iThemba Labs, South Africa), which have been founded either by the DAAD or DFG. Further collaborations have been conducted with the groups at the University of Lund (Sweden, Prof. L. Samuelson), Australian National University Canberra (Australia, Prof. M. Ridgway), University of Southern California (USA, Prof. J.G. Lu), University of Florence (Italy, Dr. F. di Benedetto), University of the Basque Country (Spain, Prof. A. Rubio), ERSF Grenoble (France, Dr. G. Martinez-Criado, Dr. M. Burghammer & Dr. F. d'Acapito) and Imperial College (UK, Dr. R. Oulton & Prof. O. Hess). National collaborations involve partners from Bremen, Duisburg, Mainz, Leipzig, Braunschweig, and Erlangen within the frame of the DFG research unit FOR1616. In the field of photovoltaics, ongoing collaborations include groups at the HZ Berlin, FHI Berlin, Manz AG, and ZSW Stuttgart.

The Low Temperature Physics group of **Prof. Dr. Paul Seidel** is collaborating with Thuringian research institutions (TU Ilmenau, IPHT Jena, SUPRACON Jena, Innovent e.V. Jena, Helmholtzinstitut Jena). Within funded research projects joint research is carried out with the IFW Dresden, the GSI Darmstadt, the DESY Hamburg, the MPI Heidelberg and the CERN Genf. Long-term collaborations exist to the Karlsruhe Institute of Technology KIT and the research groups at the universities in Erlangen-Nürnberg, Hannover, Dresden, Gießen, Heidelberg, Tübingen as well as the Universities of Applied Science in Aalen and Jena. Scientific results have been obtained in close collaboration with national (Hannover, Tübingen,

Golm, Garching) as well as international partners, such as the universities of Glasgow, Padova, Lyon, Tokyo, Pisa, Salerno, Roma, Moscow and others. Additional international partners in the field of superconducting materials and its application are the universities of Bratislava, Poznan, Twente, Donetsk, Kharkov, Osaka, Nagoya and Tokyo.

The ion beam physics group of **Prof. Dr. Elke Wendler** cooperated in 2015 with Prof. Dr. Fadei F. Komarov (BGU Minsk), Prof. Dr. Maria Katsikini (U Thessaloniki), Dr. Katharina Lorenz (IST, U Lissabon), Prof. Dr. Johan B. Malberbe (U Pretoria), Dr. Alexander Yu. Azarov (U Oslo). National cooperations exist with Dr. Klaus Ellmer (HZ Berlin) and Dr. Jan Dellith (IPHT Jena).

In 2015, the laboratory astrophysics and cluster physics group of **Dr. Cornelia Jäger** collaborated with Prof. Dr. S. Price, University College London, Dr. Lisseth Gavilan from Institut d'Astrophysique Spatiale (CNRS, Paris), Prof. Dr. E. Palumbo (INAF–Osservatorio Astrofisico di Catania), Prof. Dr. A. Kereszturi, Research Centre for Astronomy and Earth Sciences, Budapest, Prof. P. Scheier, University of Innsbruck, and Prof. E. Kovacevic (GREMI, Université d'Orléans). Strong collaborations with German groups exist with Prof. Dr. P. Caselli (MPI für Extraterrestrische Astrophysik, München), Dr. S. Zhukovska (MPI für Astrophysik, München), Prof. Dr. S. Schlemmer (Cologne Laboratory Astrophysics Group), Prof. T. Giesen (Laboratory Astrophysics Group at the University Kassel), and Dr. Holger Kreckel (Max Planck Institute for Nuclear Physics, Heidelberg).

4.2 Visiting Scientists

Prof. Dr. Takashi Yamada	Osaka (Japan)
Prof. Dr. Toshiaki Munakata	Osaka (Japan)
Prof. Dr. Satoshi Kera	Okazaki (Japan)
MSc. Yui Ioka	Chiba (Japan)
Prof. Dr. Krish Bharuth-Ram	TU Durban (South Africa)
Dr. Sebastian Lehmann	U Lund (Sweden)
Prof. Dr. J. Grace Lu	U Southern California (USA)
Dr. T.P.H. Sidiropoulos	Imperial College London (England)
Prof. Dr. G. Cagnoli	LMA / Lyon (France)
Dr. K. Haughian	IGR / Glasgow (Scotland)
Dr. Mikhail Belogolovskii	Donetsk Physical and Technical Institute, National Academy of Sciences of Ukraine (Ukraine)
Dr. Olena Zhytlukhina	Donetsk Physical and Technical Institute, National Academy of Sciences of Ukraine (Ukraine)
Dr. Yury M. Shukrinov	Bogoliubov Laboratory of Theoretical Physics, Joint Institute for Nuclear Research Dubna, Moscow Region (Russia)
Dr. Kulikov, Kirill	Bogoliubov Laboratory of Theoretical Physics, Joint Institute for Nuclear Research Dubna, Moscow Region (Russia)
Rahmonov, Ilhom	Bogoliubov Laboratory of Theoretical Physics, Joint Institute for Nuclear Research Dubna, Moscow Region (Russia)

Dr. Arnold Gucsik	Konkoly Thege Miklos Astronomical Institute, Astrophysical and Geochemical Laboratory, Budapest, Hungary and Department of Geology, University of Johannesburg
Prof. Dr. Jan Cami	University of Western Ontario, Department of Physics and Astronomy, Ontario, Canada
Dr. Roland Gredel	Max-Planck-Institut für Astronomie, Heidelberg
Dr. Svitlana Zhukovska	Max-Planck-Institut für Astrophysik Garching
Dr. A. Yu. Azarov	U Oslo

4.3 Colloquia at the Institute of Solid State Physics

Prof. Dr. Gianpietro Cagnoli, 9. Jan. 2015

Modern Coatings for Advanced and Future Gravitational Wave Detectors

Prof. Dr. Sibylle Gemming (TU Chemnitz / HZDR), 23. Jan. 2015

Microscopic processes in data and energy storage – considerations based on multiscale modeling

Prof. Dr. Christian Loppacher (IM2NP - UMR CNRS), 30. Jan. 2015

Kontrollierte Selbstorganisation von organischen Molekülen auf Ionenkristallen durch geeignete Wahl von polaren Ankergruppen

Dr. Claudia Stahl (MPI Stuttgart), 24. April 2015

Detecting Magnetic Flux Density Distributions in High-Tc Superconductors with Magnetic X-ray Microscopy

Prof. Dr. Roel van de Krol (HZ Berlin), 22. Mai 2015

Multinary Metal Oxide Photoelectrodes for Solar Water Splitting

Prof. Dr. Stefan Krischok (TU Ilmenau), 5. Juni 2015

Elektronische Oberflächeneigenschaften von Gruppe III-Nitriden und deren Beeinflussung durch Adsorbate

Prof. Dr. Christina Trautmann (GSI Darmstadt & TU Darmstadt), 19. Juni 2015

Materials Research and Nanotechnology with MeV-GeV Ion Beams

Dr. Tilmann Leisegang (TU Bergakademie Freiberg), 3. Juli 2015

Elektrochemische Energiespeicherung

Dr. Rüdiger Schmidt-Grund (U Leipzig), 10. Juli 2015

Ellipsometry: From Electronic Properties to Surface Structures

Dr. Svitlana Zhukovska (Max-Planck Institut für Astrophysik), 13. Nov. 2015

Cosmic dust lifecycle with 3D numerical simulations of the Interstellar Medium

Dr. Marcus Schwickert (GSI Darmstadt), 27. Nov. 2015

Kryogene Stromkomparatoren für das internationale FAIR Projekt

Prof. Dr. Stefan G. Mayr (IOM Leipzig), 11. Dez. 2015

Ferromagnetic shape memory alloys: From ion-beam-assisted synthesis to plasma-aided functionalization for biomedical applications

5. Personnel

Professors

Prof. Dr. habil. Torsten Fritz
Prof. Dr. habil. Carsten Ronning
Prof. Dr. habil. Paul Seidel
apl. Prof. Dr. habil. Elke Wendler
apl. Prof. Dr. habil. Frank Schmidl

Scientific Staff

Dr. Roman Forker	Dr. Udo Reislöhner
Dr. Daniele Fulvio	Dr. Gael Rouillé
Dr. Ernst Glaser	Dr. Bernd Schröter
Dr. Christoph Heisler	Dr. Claudia Schnohr
Dr. Cornelia Jäger	Dr.-Ing. Christian Schwarz
Dr. Andreas Johannes	Dr.-Ing. Volker Tympel
Dr. Sergiy Krasnokutski	Dr. Steffen Wolf
Dr. Ronny Nawrodt	

PhD Students

Davide Cammi	Ali Hasan Noor
Stefanie Eckner	Robert Röder
Martin Gnauck	Emanuel Schmidt
Marco Grünewald	Stefan Schmidt
Yaser Haj-Hmeidi	Philipp Schöppe
Gerd Hofmann	Sven Schönherr
Henry Holland-Moritz	Falko Sojka
Tobias Hümpfner	Jura Rensberg
Christian Katzer	Christian Udhardt
Tino Kirchhübel	Hagen Walter
Julius Komma	Christian Zwick
Matthias Meissner	

Extern PhD Students

Constantin Csato	FH Jena
Florian Krippendorf	FH Jena
Gregor Oeslner	IPHT Jena
Matthias Rost	Bosch Solar EnergySolarworld, Arnstadt
Thomas Schönau	IPHT Jena
Charlotte Weiss	Fraunhofer ISE, Freiberg

Diploma and Master Students

Tim Barth	Marie Mende
Sven Bauer	Felix Otto
Gregor Becker	Philip Pastrik

Ellen Butz
Walter Dickmann
Martin Feltz
Rene Glaser
Paul Gerlach
Jonas Gronemann
Martin Hafermann
Erik Haubold
Torsten Lindemann

Max Riediger
Lisa Schade
Markus Schwiderke
Alexander Tille
Lukas Trefflich
Enrico Treiber
Maximilian Zapf

External Diploma and Master Students

Michelle Geleen (U Hasselt, Belgium)
Claudia Schnitter (U Linköping, Sweden)
Anton Zimare (Vacom)

Marcus Junghanns (IPHT Jena)
Steffen Becker (Nanoplus, Würzburg)

Technical Staff

Ulrich Barth
Cindy Büchner
Uwe Eberhardt
Tobias Eißmann
Lutz Föllmer
Silke Frunzke
Kristina Garlipp
Frank Jehn
Patrick Hoffmann

Holger Mühlig
Anja Mittelstädt
Ralf Neubert
Stefan Prass
Helga Rudolph
Sylvia Stender
Matthias Thürk
Carmen Voigt

6. Technical Reports and Equipment

6.1 Operation of the Ion-Accelerator JULIA and the Ion-Implanter ROMEO

U. Barth, P. Hoffmann, F. Jehn, C. Ronning

The 3 MV high current tandetron accelerator **JULIA** (Jena University Laboratory for Ion Acceleration) went in operation end of 1996. Since the beginning of the routine-operation in 1997 it has been used for different types of experiments requiring a broad spectrum of ion-beams. With the exception of helium, where the duoplasmatron ion-source followed by a lithium exchange channel was used, all ions were extracted from a sputter-type ion-source. The beam-on-target-time of 1250 h was a little bit higher than in 2014. The 400 kV ion-accelerator **ROMEO** is in routine operation since 1998, here the beam-on-target-time of 1200 h was also 30 % higher as in the preceding years. Both accelerators can be operated separately or in combination. The ion-beams produced until 2015 are summarized in table 1. The ion-beam currents quoted are typical values of the ion source currents used for the experiments.

Period	Element	Julia	Romeo	
1	Hydrogen (H)	1 μ A	4 μ A	
	Helium (He)	0,1 μ A	4 μ A	
2	Lithium (Li)	2 μ A	-	
	Boron (B)	0,1 μ A	5 μ A	
	Carbon (C)	3 μ A	1 μ A	
	Nitrogen (N)	0,4 μ A	4 μ A	
	Oxygen (O)	2 μ A	2 μ A	
	Flourine (F)	-	2 μ A	
	Neon (Ne)	-	5 μ A	
	3	Sodium (Na)	-	6 μ A
Magnesium (Mg)		-	5 μ A	
Aluminium (Al)		-	4 μ A	
Silicon (Si)		16 μ A	4 μ A	
Phosphorus (P)		1 μ A	4 μ A	
Sulfur (S)		1 μ A	-	
Chlorine (Cl)		-	2 μ A	
Argon (Ar)		-	20 μ A	
4		Potassium (K)	-	3 μ A
		Manganese (Mn)	0,02 μ A	5 μ A
	Iron (56 Fe)	0,8 μ A	2 μ A	
	Iron (57 Fe)	-	0,015 μ A	
	Copper (Cu)	0,5 μ A	1 μ A	
	Zinc (Zn)	0,05 μ A	6 μ A	
	Gallium (Ga)	-	3 μ A	
	4	Germanium (Ge)	1,6 μ A	4 μ A
Arsenic (As)		0,4 μ A	1 μ A	
Selenium (Se)		0,5 μ A	1,5 μ A	
Krypton (Kr)		-	10 μ A	
5		Strontium (Sr)	-	3 μ A
	Yttrium (Y)	-	4 μ A	
	Rhodium (Rh)	0,2 μ A	-	
	Palladium (Pd)	0,09 μ A	1 μ A	
	Silver (Ag)	1,6 μ A	10 μ A	
	Cadmium (Cd)	-	0,8 μ A	
	Indium (In)	0,5 μ A	8 μ A	
	Tin (Sn)	1,0 μ A	3 μ A	
	Iodine (I)	3 μ A	-	
	Xenon (Xe)	-	10 μ A	
6	Caesium (Cs)	-	4 μ A	
	Samarium (Sm)	0,01 μ A	1,5 μ A	
	Europium (Eu)	0,03 μ A	2 μ A	
	Erbium (Er)	0,04 μ A	2 μ A	
	Thulium (Tm)	-	1 μ A	
	Tungsten (W)	0,3 μ A	0,01 μ A	
	Osmium (Os)	0,05 μ A	-	
	Platinum (Pt)	0,2 μ A	-	
	Gold (Au)	2,8 μ A	20 μ A	
	Lead (Pb)	0,03 μ A	15 μ A	

Table 1: Ion-beams accelerated until 2014. The currents given were measured at the *Q-Snout-Faraday-cup* after the low-energy mass separator (*JULIA*) and at the target position (*ROMEO*), respectively.

A computer control system was been installed on the accelerator Romeo in this year, and a screen shot is displayed in figure 1. Once can now record the parameters of the ion source. This addition enables more optimal operation of the ion source. The gas supply for the ion source was been modernized. The operational safety is by this upgradings significantly increased.

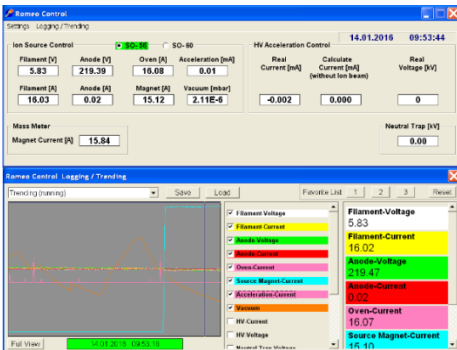
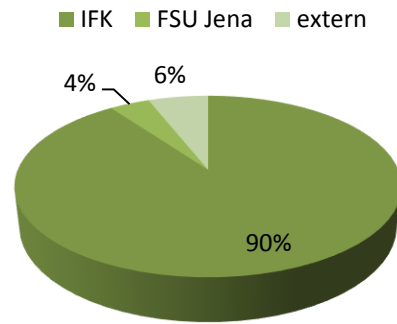


Figure 1: Screenshot of the new control program of the ion accelerator ROMEO.

As in the preceding years the ion-beam facility was used by external research groups:

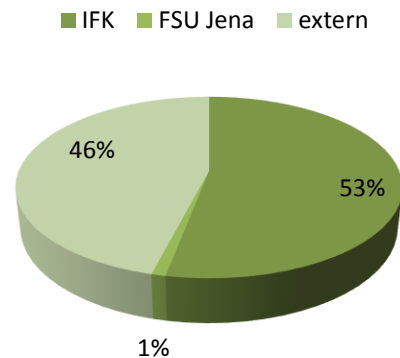
3 MV-Tandatron „JULIA”

- University of Pretoria, South Africa
Dr. Thulani Hlatshwayo
- Ernst-Abbe-Hochschule Jena,
Mr. Grimm
- IPHT Jena
Dr. Diegel
- Ernst-Abbe-Gymnasium Jena
Seminar paper
- Angergymnasium Jena
Seminar paper
- Belorussian State University, Belarus
Prof. F.F. Komarov, Dr. L. Vlasukova,
Mr. Uladzimir Pilko, Mr. Maksim Makhavikou



400kV Implanter „ROME0“

- iThemba Labs, South Africa
Prof. K. Bharuth-Ram
- University of Lund, Sweden
L. Samuelson, H. Pettersson
- TU Vienna, Austria
Prof. A. Lugstein
- PDI Berlin
Dr. L. Geelhaar
- Belorussian State University, Belarus
Prof. F.F. Komarov, Dr. L. Vlasukova
Mr. Uladzimir Pilko, Mr. Maksim Makhavikou



6.2 Cryogenic Services (TTS)

M. Thürk

All in-house customers of cryogenic liquids, which are all faculties of natural sciences, the university medical division including several hospitals, and other external scientific institutes (e.g. Institute for Photonic Technology Jena, Leibniz Institute Hans-Knöll Jena) as well as some private customers like the Innovent e.V. Jena and some medical practices, were provided with liquid helium (LHe), with high purity gases (He, N₂), and with cryogenic gases like liquid nitrogen (LN₂) and liquid argon (LAr) by the Cryogenic Services. Roughly 119,000 litres of LN₂ were delivered by the cryogenic services in 2015. The total delivery has been levelled out over the last years due to the by now stabilized demands of inert gas in the IAAC-institute and the new installed ZAF site.

As illustrated in Figure 1, the output of liquid helium (LHe) has decreased in 2015. Roughly 33,000 litres of LHe were delivered which calls for an annual gross refrigeration value of just 40,600 litres which corresponds to an annual all round price of € 0.45 million. Last three years we had to face a worldwide shortage in helium supplies which leads generally to increased costs with persistent fierce fluctuations of the competitive market price over the year. On the crest of the wave the costs for short term LHe-orders have increased by a fivefold. Therefore the financial weakness and supply shortfall have caused a strong reduction in LHe-

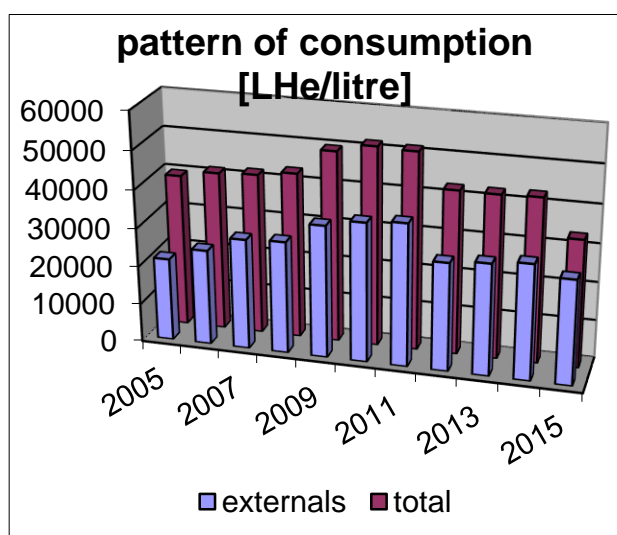


Figure 1 Liquid helium output.

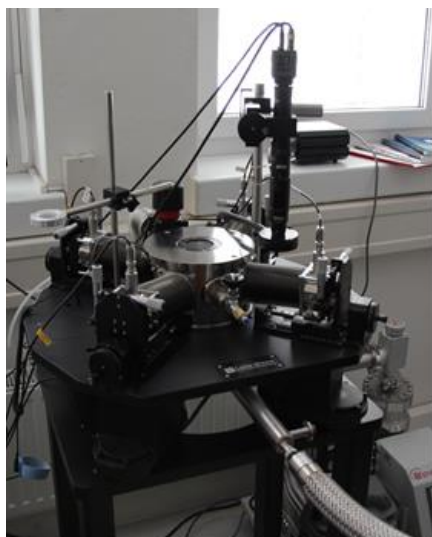


Figure 2: Lake Shore TTPX probe station.

use since 2012. Fortunately the relation between the produced amount of LHe to the bought quantity was a good deal bigger than the years before 2012 to 2013. In spite of the lower production rate the rising market prices increased the gross financial benefits of the internal helium liquefaction for all users noticeably. Mentoring of scientists using new standard cryogenic equipment has become more important over the previous periods. Last year the TTS staff has carried out advisory services to implement proper cryogenic procedures on various new acquired scientific installations. Some of the finest examples are a new NMR-instrument, a cryo-vacuum pump, a He-3 refrigerator and a low temperature probe station which is presented in Fig. 2. The project “helium-recovery” for the Max-Wien-Platz 1 site is under way.

6.3 Equipment

Preparation of Thin Films and Devices

- HV evaporation facilities for thermal and electron beam evaporation
- UHV evaporation facilities, including electron gun and in situ RHEED system
- Equipment for laser deposition of thin crystalline films and material systems, especially high temperature superconductors (KrF excimer laser, $\lambda = 248$ nm)
- Molecular Beam Epitaxy (MBE) facilities: MBE for silicon carbide (RIBER EVA 32 R&D)
- Organic Molecular Beam Epitaxy (OMBE) facilities including surface analysis techniques (MCP-LEED, UHV STM/AFM, RHEED) and *in situ* optical spectroscopy (PL and DRS)
- dc and rf sputtering systems for metallic (Au, Ti) and oxidic (SiO_2 , Ta_2O_5) thin films and multilayers
- Ion beam etching with Ar ions at sample temperatures down to 80 K in vacuum
- Chamber for ion- and reactive etching up to 4" wafer
- Reactive ion beam etching with sample diameters up to 6 cm
- Ultrasonic wire bonder
- Equipment for photolithographic patterning
- MBE system NEBULA for $\text{Cu}(\text{In,Ga})\text{S}_2$ layers on 4" substrates including RHEED setup
- Two HV systems for closed-space sublimation (CSS) for deposition of CdTe layers
- RF reactive sputtering system for transparent conducting oxides (TCO's) and molybdenum
- DC sputtering system for copper and indium
- UHV system ULS400 for $\text{Cu}(\text{In,Ga})(\text{Se,S})_2$ on (100x100) mm^2 substrates
- Wet chemical processing and chemical bath deposition of photoactive layers

Surface Analysis Systems

- LT-STM/AFM (1.1 K) with 3 Tesla magnet, QMS (1000 amu), MCP-LEED, DRS
- Surface analysis systems SPECS and UNISPEC with XPS, UPS, AES, LEED, STM
- AUGER electron spectrometer
- Atomic force microscopes (AFM and Microstructure Measuring Device VERITEKT 3 with needle sensor)
- Surface profilometer DEKTAK 100
- Scanning electron microscopes
- Several UHV-scanning probe devices (STM, AFM)

Electrical Measurement Techniques

- Electrical transport measurements (resistance, critical current density, point contact and tunneling spectroscopy)
- Hall-effect and Four-point probe equipment
- Current-voltage characteristics ($2 \text{ K} < T < 300 \text{ K}$, $B \leq 5 \text{ T}$)
- Current-voltage characteristics by microwave irradiation ($2 \text{ GHz} < f < 300 \text{ GHz}$)
- Noise measurements (frequency range 60 μHz - 100 kHz) at low temperatures
- LTS-SQUID characterization at 4.2 K (current-voltage, flux-voltage, noise, screening properties)
- HTS-SQUID characterization up to 100 K (current-voltage, flux-voltage, noise)
- 2 Deep level transient fourier spectrometers (temperature range 80 K - 690 K, 30 K - 330 K)
- 3 Admittance spectrometers (frequency range 40 Hz - 100 kHz, 20 Hz - 2 MHz and 75 kHz - 30 MHz, temperature range 30 K - 690 K)

- Microwave signal generator (frequency range 1 - 20 GHz, resolution: 1 kHz)
- Electrical and optical characterization of high power diode laser arrays

Equipment for Optical Characterization

- UV-VIS spectrometer
- FTIR spectrometer
- Cathodoluminescence at SEM, equipped for IR - UV
- Micro-Photoluminescence, IR-UV, time-resolution ~ 1ns
- Photoluminescence excitation (PLE)
- Optical cryostats (2...300 K) for optical absorption, photoluminescence and Raman spectroscopy
- Excitation lasers in a wide range from 405-1550 nm (fiber, gas, solid state and diode lasers)
- Optical microscopes
- Magnetrelaxation of ferrofluids (MORFF) for characterization of magnetic nanoparticles

Equipment for Electro-Optical (Solar) Characterization

- Solar simulator (AM 1.5) with Current-Voltage measurement
- Illuminated Current-Voltage measurements for 10 K to RT
- Quantum efficiency (EQE) measurements of solar cells

Equipment for Thermal Treatment

- Furnace for conventional thermal treatment in inert gas atmosphere or vacuum (temperatures up to 2050 K)
- RTA apparatus (double graphite strip heater) for short time annealing (annealing time in the order of seconds, temperature range 1000 K to 1950 K, temperature rise rate 100 K s⁻¹)

Electron Microscopy

- Scanning electron microscope JEOL JSM-6490 with LaB₆-cathode
- FEI field-emission electron microscope connected with FIB system

Ion Beam Techniques

3 MV Tandatron accelerator "JULIA", equipped with

- Sputter ion source and Duoplasmatron source
- Universal beam line for ion implantation and ion beam analysis
- Second beam line for ion beam analysis, combined with implantation chamber of 400 kV implanter
- Irradiation chamber with cooled and heated sample holder and four axis goniometer

Application:

- Ion implantation: energy range 500 keV - 12 MeV, temperature range 15 K - 1500 K
- Ion beam analysis: RBS and PIXE in combination with channeling, ERDA, NRA

400 kV implanter "ROMEO", equipped with

- Hot filament, hollow cathode ion source
- Irradiation chamber with cooled and heated sample holder and four axis goniometer, combined with beam line of 3 MV Tandatron accelerator

Application:

- Ion implantation: energy range 20 keV - 400 keV, temperature range 15 K - 1500 K
- Ion implantation at low temperatures and subsequent RBS analysis using H- or He-ions from 3 MV Tandatron accelerator

Low Energy implanter "LEILA", equipped with

- Colutron Ion source 100-Q
- Colutron Ion Gun System G-2-D
- Irradiation chamber with heated sample holder

Application:

- Irradiation of surfaces: energy range sub-keV, temperature range 300 K - 750 K

Low Energy implanter "Mr. JIM Stringer", equipped with

- Hot filament, hollow cathode ion source
- Irradiation and deposition chamber

Application:

- Deposition of diamond-like thin films: energy range 100eV – 30 keV, RT

Focused Ion Beam system FEI NanoLab Helios 600i

- Liquid ion source, E = 500 eV – 30 keV
- Electron microscope, E = 350 eV – 30 keV

Application:

- TEM-lamella preparation, etc.

Low Temperature Measuring Equipment

- LT STM/AFM down to 1.1 K. 3 Tesla magnet available
- He-4 cryostats for temperatures down to 4.2 K
- He-4 refrigerator for the temperature range 1.3 K - 4.2 K
- [Cryostat](#) for temperatures range 4,2K - 300 mK with superconducting magnet to 2 T
- He-3/He-4 dilution refrigerator for temperatures range 4,2 K - 6 mK with superconducting magnet to 10 T
- He-3/He-4 dilution refrigerator with a base temperature of 35 mK
- Electronic equipment for characterization of cryoelectronic devices
- SQUID sensor systems for magnetic measurements under unshielded conditions
- SQUID sensor system for spatially resolved magnetorelaxometry
- Cryostats (2 K < T < 300 K; optical window; magnetic field)
- Cryocoolers (Gifford-McMahon and Stirling)
- Pulse tube refrigerators (for sensor cooling)

7. Scientific Reports

Plastic deformation in ion irradiated, amorphous Si nanowires

Andreas Johannes, Stefan Noack, Werner Wesch, Markus Glaser*, Alois Lugstein* and Carsten Ronning

* Vienna University of Technology, Institute of Solid State Electronics, Floragasse 7, 1040, Vienna, Austria

Ion implantation is a versatile tool to modify the properties of semiconductors in general and Si specifically. In addition, Silicon is to date the most studied semiconductor and ion irradiation in silicon has been studied at great lengths. Because it is instrumental in the development and production of modern microelectronics, many textbooks cover the topic [1]. We demonstrate a novel observation in this work in that for certain ion implantation parameters silicon nanowires are plastically deformed by the impinging ion beam [2].

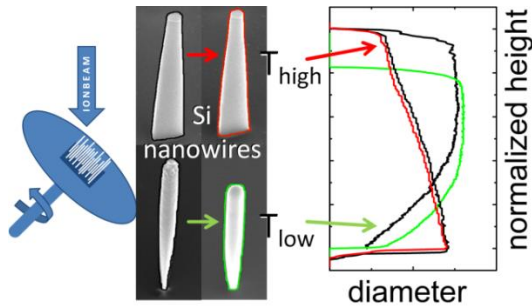


Fig. 1: Schematic experimental setup (left) with rotated irradiation of Si nanowire arrays. SEM image (middle) showing nanowires irradiated at elevated (top, red) and room temperature (bottom, green). On the right the local diameters extracted from such images are shown.

Top-down fabricated Si nanowire arrays of various diameters were irradiated with multiple ion fluences at room temperature while rotating them at 45° to the 100 keV Ar^+ ion beam. With these irradiation conditions Si amorphizes at very low ion fluences [3]. Scanning electron microscopy (SEM) images shown in Fig. 1 were taken of individual nanowires before and after each irradiation step. Image processing yields the diameter over height profile

shown. Figure 2 shows the progressive deformation with increased ion fluence for one particular, exemplary nanowire.

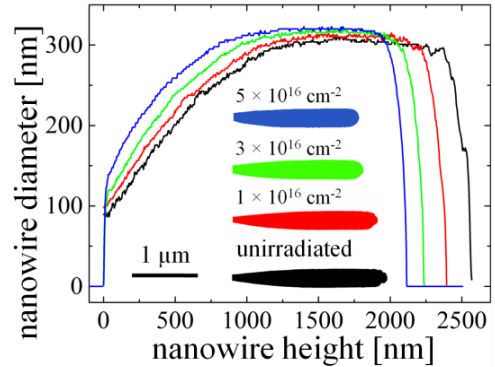


Fig. 2: Diameter versus height of one single nanowire before (black-line) and after 1×10^{16} (red), 3×10^{16} (green) and $5 \times 10^{16} \text{cm}^{-2}$ (blue) 100 keV Ar^+ irradiation. The clear shrinking and slight broadening is visible in both the plotted diameter profiles and the inset SEM profiles of this nanowire.

A quantitative evaluation of this plastic deformation from such curves was performed to extract an effective mass transport rate. This is a measure for the deformation which can directly be compared to simulation results. The average mass transport rate is 1.2×10^4 atoms·nm/ion with a standard deviation of 7×10^3 atoms·nm/ion, including some outliers showing very large deformation. This means that in order to change the form of the nanowire shown in Fig. 2 from black to red, on average 1.2×10^4 atoms are displaced by one nanometer for every ion hitting the nanowire.

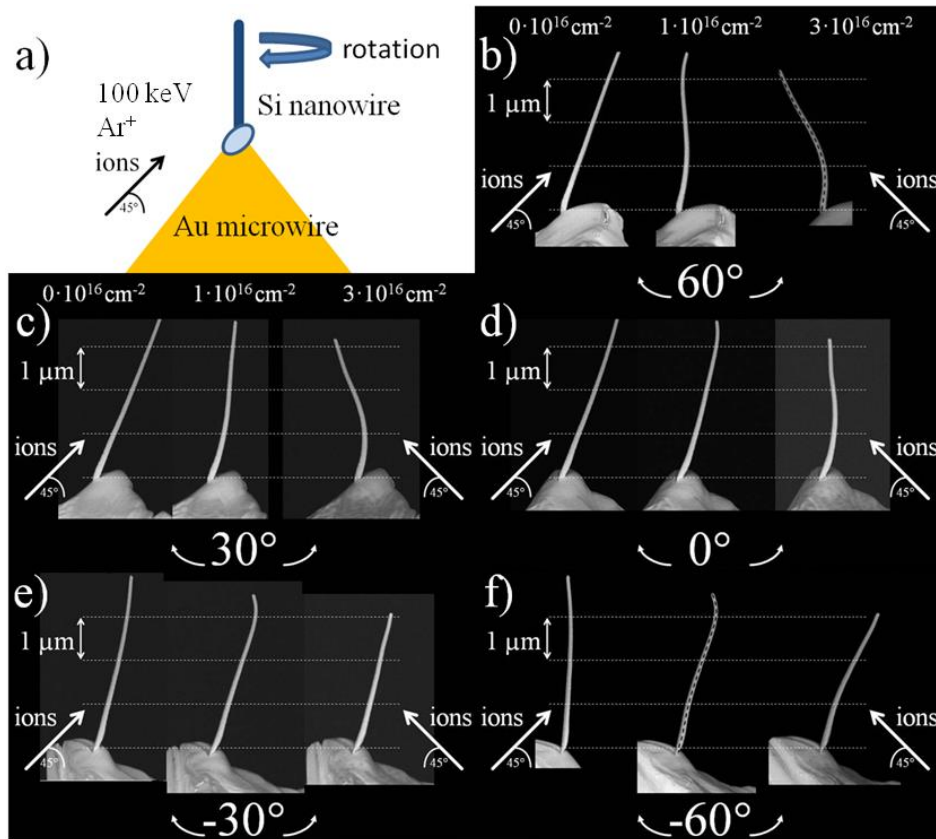


Fig. 3: (a) Schematic illustration of the rotated irradiation under “ -45° ” to the nanowire axis. (b–f) SEM images acquired perpendicular to the axis of rotation during the irradiation. The same nanowire is shown at different observation angles shown below the respective images. The total irradiated fluence is indicated above the respective images in panel b,c. The angle of incidence of the ion beam is indicated on both sides of each image. The dashed horizontal lines are $1\ \mu\text{m}$ apart and guide the eye, while the dashed lines along the nanowires in panels b and f indicate where the length of these wires was measured.

To evaluate whether the plastic deformation is coincident with the ion beam direction, an individual nanowire was attached to a sharpened Au microwire with a focused ion beam (FIB) tool to allow irradiation from “below the substrate”. Fig. 3 a) illustrates the principle, whereby the VLS-grown Si nanowire is fixed on an Au microwire and to a rotatable stage in the irradiation chamber under “ -45° ” to the ion beam.

The SEM images in Fig. 3 b-f) clearly show that the deformation is not aligned with the impinging ions. Thus, the driving force for the deformation can be found in the surface tension. It can act on the nanoscale slices of the nanowire in which

the atoms are heated and mobilized for a short time with each impinging ion. The total surface area is thus incrementally reduced by an incrementally increased local radius and shorter length of the wire.

References

- [1] Nastasi, M.; Mayer, J.; Hirvonen, J. K. *Ion-Solid Interactions: Fundamentals and Applications*. Cambridge University Press (2008).
- [2] Johannes A. et al. *Nano Letters* **15**, 3800 (2015).
- [3] Pelaz, L.; Marqués, L. A.; Barbolla, J. *J. Appl. Phys.* **96** (2004).
- [4] Borschel, C.; Ronning, C. *Nucl. Instrum. Methods Phys. B* **269**, 2133 (2011).

Modeling of redeposition and sputtering of ion irradiated Au nanoparticles

Henry Holland-Moritz, Andrey Ilinov¹, Flyura Djurabekova¹, Kai Nordlund¹,
Carsten Ronning

¹Department of Physics, University of Helsinki, Finland

Nanoparticles (NPs) can easily be fabricated by different physical and chemical processes and can be arranged in many different patterns. The synthesis of NPs is usually restricted to thermal equilibrium conditions. Ion beam irradiation, a non equilibrium method, is a tool to tune the properties of NPs [1, 2]. An important effect in this case is sputtering, since it is enhanced for NPs compared to bulk geometry. The sputtered material could be redeposited on neighboring particles for patterned NPs.

A Monte-Carlo (MC) code has been developed to investigate this effect and simulate the interaction of patterned NPs under ion irradiation. The code simulates a 4×4 grid with quadratic cells. The NPs were placed in the center of the cell. The NP size was randomly chosen from the Gaussian size distribution obtained in reference [1] with a mean NP diameter of 51 nm. A Gaussian size distribution with mean diameter of 25 nm was used to cover also smaller NP sizes. Periodic boundary conditions were applied in x and y direction to simulate a large NP pattern. The irradiation and pattern parameters were taken from experiments [1]. As a sputter model the Järvi model [2, 3] was used and scaled to fit the experiments presented in reference [1]. The simulations were repeated 120 times with different random seeds. The ion species was Ga^+ with an energy of 25 keV.

The statistical results are shown in figure 1. The red curve shows the distribution before irradiation. The orange

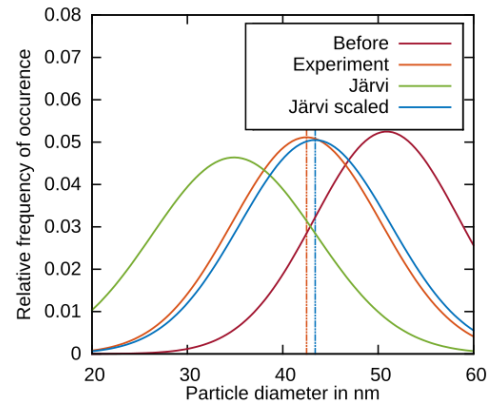


Fig. 1: Size distributions of NPs before (red) and after irradiation.

curve represents the experimental NP size distribution after irradiation with a mean diameter of (42.5 ± 7.8) nm. The green curve shows the simulated results using the pure Järvi model with a mean diameter of (35.6 ± 8.2) nm. The results using the scaled Järvi model fit the experimental results best with a mean diameter of (43.4 ± 7.9) nm. If the redeposition in the simulation is switched off, the mean diameter is (41.8 ± 8.1) nm, which is also in line with the experiment.

To investigate the amount of sputtered material on the NPs in detail, the ratio of gained versus sputtered atoms as a function of the initial NP diameter is shown in figure 2 a). The yellow and blue points show the results for single particles for 25 nm and 51 nm mean diameter, respectively, while the red points show the average values for a certain NP size. One can see that the gained versus sputtered ratio decreases linearly with decreasing NP size for NP sizes larger 20 nm, as the linear fits shown in orange indicate. The ratio of

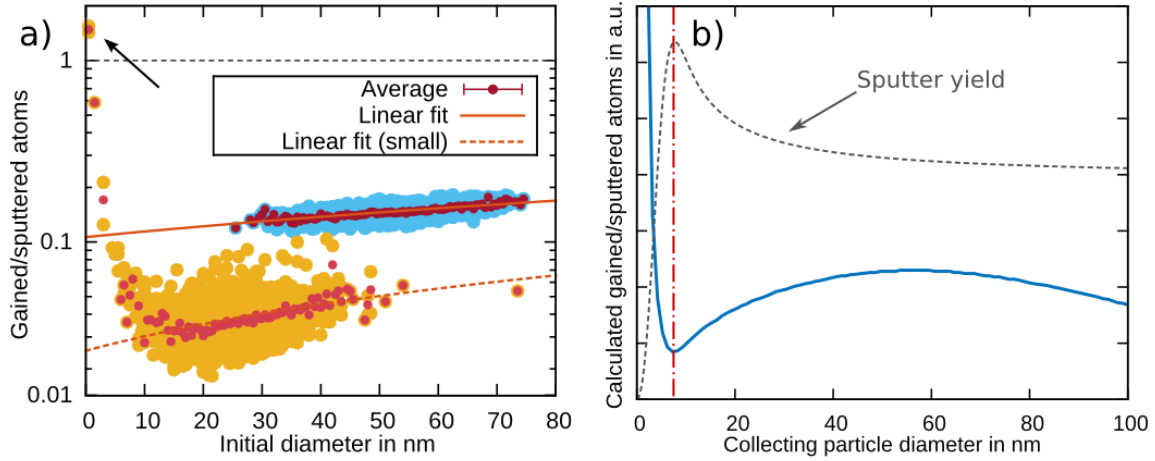


Fig. 2: Ratio of gained versus sputtered atoms as a function of the initial diameter a) for the two simulated size regimes and b) calculated by model.

gained versus sputtered atoms is up to 0.18 depending on the NP size.

For NP sizes smaller than 20 nm, the behavior changes. Smaller NPs gained relatively more atoms and the ratio increases non-linearly with decreasing NP size. NPs with sizes smaller than 5 nm compensate a relevant amount of their sputtered material. NP with sizes of 1 nm show a gained versus sputtered atom ratio of 1.4, which means they actually grow by redeposited material.

One has to consider two competing mechanisms to understand this behavior: the sputtering process and redeposition. The number of sputtered atoms depends on the probability of an ion hitting a NP with cross section $A(d)$, and on the sputter yield $Y(d)$. The number of collected atoms depends on the solid angle covered by the NP $\Omega(d, D)$, which depends on the NP diameter d and the average interparticle distance D . The ratio of gained versus sputtered R_{gs} atoms is then given by

$$R_{gs} \propto \frac{\Omega(d, D)}{Y(d) \cdot A(d)}.$$

The sputter yield acts as a scaling factor, as shown in figure 2 b), the minimum of R_{gs} matches the maximum of the sputter

yield. In figure 2 b), the model is shown for a NP with a diameter of 50 nm and a mean interparticle distance of 50 nm. This leads to the conclusion that the size dependence of the sputter yields decides, whether sputtering or redeposition is the dominating process.

In this work, we investigated the redeposition process sputtered atoms from ion irradiated Au NPs on neighboring NPs qualitatively and quantitatively. The statistical results using a scaled Järvi sputtering model matches experimental results. For NP sizes larger than 20 nm, the redeposition compensates up to 18 % of the sputtered material, while NPs with sizes smaller than 2 nm grow due to redeposition.

References

- [1] C. Ronning *et al.*, *Mater. Sci. Eng. R Rep.* **70**, 30-43 (2010).
- [2] A. Johannes *et al.*, *Semicond. Sci. Technol.* **30**, 033001 (2015).
- [3] H. Holland-Moritz *et al.*, *Nanotechnology* **32**, 325301 (2015).
- [4] T. T. Järvi *et al.*, *EPL Europhys. Lett.* **82**, 26001 (2008).
- [5] T. T. Järvi *et al.*, *Nucl. Instrum. Methods Phys. Res. Sect. B.* **87**, 66-69 (2012).

Measuring the laser onset time of semiconductor nanowire lasers

R. Röder, T.P.H. Sidiropoulos*, R.F. Oulton* and C. Ronning

* Imperial College London

The immense progress in understanding and tuning the properties of semiconductor nanowire (NW) lasers drives conceptual thoughts exploiting coherent radiation available at dimensions below the wavelength barrier [1]. Such nanoscale light sources are especially required to keep up with recent developments in nanophotonics and photonic circuitry to circumvent the drawbacks of conventional electronic circuitry. Semiconductor NWs, made from high optical gain material, mark the lower size limit for laser oscillators based on photonic modes, because they provide efficient waveguiding as well as resonator feedback. Most of the fundamentals of NW lasers like emission wavelength, polarization and cavity modification have been studied in the past years. However, the temporal dynamics of these smallest lasers remain relatively unstudied, mainly due their ultrafast response times and small intensities, which are difficult to detect.

Knowing the possible operation speed of NW lasers is urgent to judge about the potential of these devices as coherent nanoscale light source. Thus, we developed a double-pump measurement technique to assess the ultrafast onset time of CdS NWs lasers. This technique exploits the nonlinearity of the laser process and is schematically shown in figure 1a. Here, the CdS NWs, which were synthesized using a thermal transport technique [2], were optically pumped at 355 nm wavelength. Figure 1b depicts the expected response of the NW laser system; “Pump1” is sufficient to invert the laser system to $\Delta N/N_T > 0$. By generating a first output pulse at the time t_1 ,

the laser inversion gets successively depleted. Then, “Pump2” approaches at time delay τ and is not able to induce lasing on its own, but effectively samples the laser process, since the semiconductor material remained close to inversion. Thus, a second output pulse is emitted at the time τ_m . Both output pulses show interference, causing a

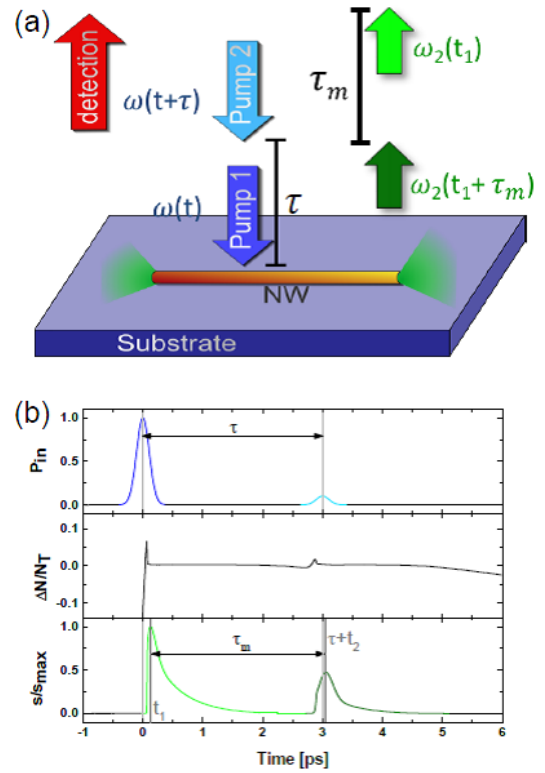


Fig. 1: (a) Schematic drawing of the measurement geometry in the double-pump technique. The nanowire laser is optically pumped with two pump pulses, which are time-delayed by τ . The two coherent output pulses occur time-delayed by τ_m . The first output pulse is emitted at the time t_1 after the first pump pulse. (b) The three graphs show the response of the strong (Pump1) and the weak (Pump2) pump pulses with power (P_{in}), the difference in population ΔN between excited (upper laser) level and ground (lower laser) level normalized to maximum inversion N_T , and the normalized cavity photon number s/s_{max} for a NW laser.

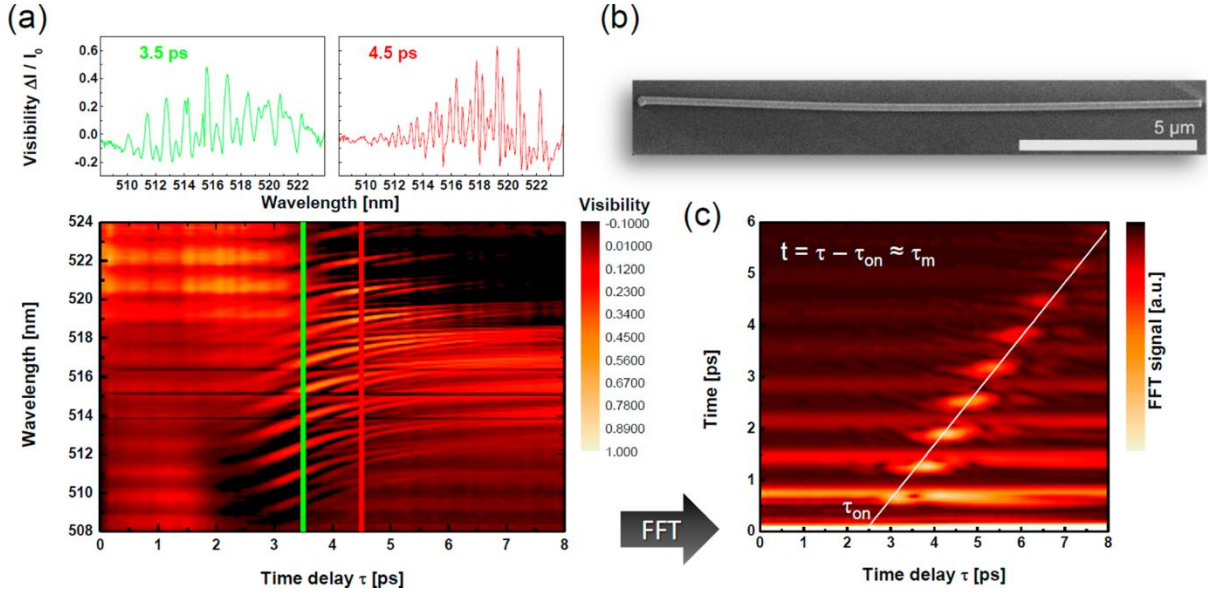


Fig. 2: (a) Visibility plot (normalized difference spectrum) $\Delta I(\lambda, \tau) / I_0(\lambda) = I(\lambda, \tau) / I_0(\lambda) - 1$ of the CdS nanowire laser (Length 15.9 μm , diameter ≈ 190 nm), which is shown in the SEM image of (b). Here $I(\lambda, \tau)$ is the microphotoluminescence (μPL) spectrum at double-pump excitation and $I_0(\lambda)$ is the μPL spectrum at single strong pulse pumping. The strong [weak] Pump1 [Pump2] was set to twice [0.2 times] the lasing threshold. The left [right] upper panel shows the visibility $\Delta I(\lambda, \tau) / I_0(\lambda)$ spectrum for the time delay $\tau = 3.5$ ps [4.5 ps] as marked in the lower visibility plot by vertical colored lines indicating the increasing spectral modulation frequency with pulse delay. The pumping wavelength was set to 355 nm. (c) Fourier transform of each spectrum of the lower color plot in (a) as function of time delay τ . The white line indicates the trend $t = \tau - \tau_{\text{on}} \approx \tau_m$. The x-axis intersect of this trend indicates $\tau_{\text{on}} = 2.5$ ps.

modulation of the spectral intensity, which is measurable in the spectrometer as function of time delay: $\Delta I(\omega; \tau) \propto \cos(\omega\tau_m + \Delta\phi(\omega; \tau))$. Indeed, the modulation increases in frequency, as shown in figure 2a. Subsequently, this spectral data were Fourier transformed into the time domain (figure 2c), such that the spectral modulation gets apparent as sideband following a linear behavior. The sideband is also depicted in figure 2c.

The sideband indicates the temporal interference of the two coherent output pulses for $t = \tau - (t_1 - t_2)$. Note, that the NW laser remains close to inversion also after emitting the first output pulse (figure 1b) leading to the reasonable assumption of $t_1 \gg t_2$. Thus, the time $\tau_{\text{on}} \approx t_1$, which is obtained as the x-axis intersect of the linear trend, is required approximately to establish the first output pulse. Therefore, the CdS

NW laser (figure 2b) reveals a laser onset time of $\tau_{\text{on}} \approx 2.5$ ps.

In conclusion, we established a double-pump measurement method to assess the ultrafast NW laser dynamics – laser onset time. This method was applied to different material systems revealing that the laser onset time is a material dependent parameter [3]. Furthermore this technique can be used to determine the NW laser output pulse width [4].

References

- [1] M. Stockman, Nat. Phys. **10**, 799-800 (2014).
- [2] S. Geburt *et al.*, Nanotechnology **23**, 365204 (2012).
- [3] R. Röder *et al.*, Nano Lett. **15**, 4637-4643 (2015).
- [4] T. Sidiropoulos *et al.*, Nat. Phys. **10**, 870-876 (2014).

Cathodoluminescence of CIGSe solar-cell-lamellae

Sven Schönherr, Philipp Schöppe, Michael Oertel, Udo Reislöhner and Carsten Ronning

CIGSe thin film solar cells reached efficiencies up to 22.3%. Such high efficiencies can only be reached with a graded band gap by a varying gallium or sulfur concentration. In a sequential process the grading can't be adjusted directly during the cell production. Therefore a characterization method with a high spatial resolution is needed to investigate the grading.

Cathodoluminescence (CL) is a powerful characterization tool which uses the electron beam of an electron microscope for excitation. But the resolution of electron beam based methods is limited because of the excitation volume. With increasing electron energy the spatial resolution decreases strongly. With energies below 5 keV a spatial resolution of few 10 nanometers can be achieved [1], but simultaneously the signal intensity reduces rapidly.

By preparing thin cross section lamellae [2], the resolution increases by cutting off the biggest part of the excitation volume. A spatial resolution of about 25 nm can be reached with an electron energy of 30 keV and a lamellae thickness of about 50 nm [3]. But for a good signal to noise ratio an optimal lamella thickness of 200 nm was found. Nevertheless the electron energy and the beam current have an impact on the cathodoluminescence spectra of thin lamellae. In figure 1 the impact of the electron beam current on the CL spectra of a 200 nm thin lamella is shown. With increasing beam current the peak energy shifts to higher energies. But this shift is not an effect of the lamellae thickness, it is a

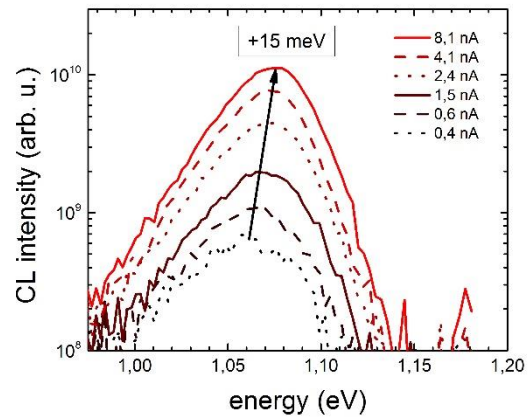


Fig. 1: Impact of the beam current on the cathodoluminescence spectra of a 200 nm thin CIGSe solar-cell-lamella.

typical behavior of highly compensated semiconductors [4].

Figure 2 shows the impact of the electron energy on the CL spectra of a 200 nm thin lamella. For low voltages, where the expansion of the excitation volume is smaller than the lamella thickness, the peak maximum shifts to lower energies with increasing electron energy. This behavior results from a change of the excitation density with changing electron energy.

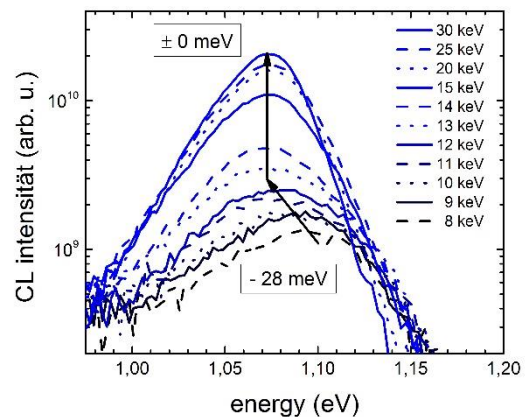


Fig. 2: Impact of the electron energy on the cathodoluminescence spectra of a 200 nm thin CIGSe solar-cell-lamella.

With lower electron energy the average excitation density increases and leads to a blue shift of the CL spectra, which is also typical for high compensated semiconductors. For high voltages, where the lamella thickness has a significant impact on the excitation volume, no peak shift can be observed. If the excitation volume is cut off by the lamellae thickness the average excitation density does not change with further increasing electron energy.

However, the cathodoluminescence characterization method also allows to measure the band gap grading. In combination with an scanning electron microscope the luminescence signal can be correlated to the excited area. Figure 3 shows an overlay of a SEM image and monochromatic cathodoluminescence images at a 240 nm thin lamellae of a CIGSe solar cell with a single grading. The gallium grading can be clearly seen by the emission energy at different regions in the absorber layer. Next to the back contact the highest emission energy has been detected and could be correlated with a high gallium concentration. With increasing distance from the back contact the emission energy

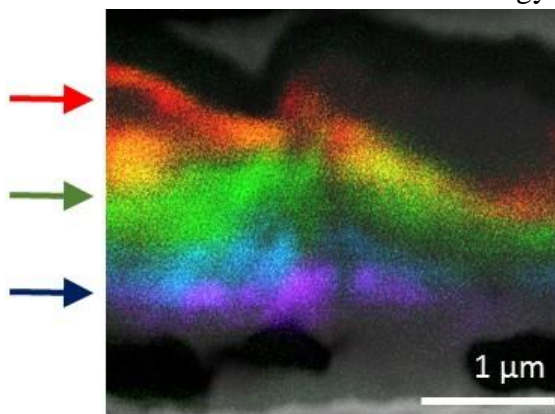


Fig. 3: Overlay of a SEM image and monochromatic cathodoluminescence images (red: 1.09 eV, orange: 1.11 eV, green: 1.13 eV, blue: 1.15 eV, violet: 1.17 eV) of a 240 nm thin lamella of a graded CIGSe solar cell.

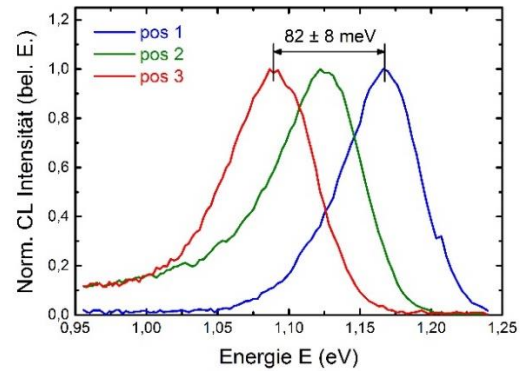


Fig. 4: Spectra at different positions at the lamella marked with arrows in figure 3.

decreases continuously. This behavior is typical for CIGSe solar cells prepared in a sequential process [5].

Figure 4 shows some CL spectra taken at different positions, marked with arrows in figure 3. The three spectra show the same behavior as the mapping in figure 3. The peak energy shifts to lower energies with increasing distance from the back contact.

In conclusion we have shown the influence of the electron energy and the beam current on the CL spectra of thin lamellae. Additionally the gallium grading has been investigated at thin lamellae with a high spatial resolution.

Finally the sequential process was optimized and cell efficiencies for single graded CIGSe solar cells without additional sulfur at the front contact have been raised up to 15.6 %, which equals 16.4 % with an anti-reflective coating.

References

- [1] I. Barkshire *et al.*, *J. Mikrochimica Acta* **132**, 113-128 (2000).
- [2] P. Schöppe *et al.*, *Appl. Phys. Lett.*, **106**, 013909 (2015).
- [3] S. Schönherr *et al.*, *PVSC 2014 IEEE 40th*, 1699-1703 (2014).
- [4] M.J. Romero *et al.*, *Appl. Phys. Lett.*, **83**, 4770 (2003).
- [5] T.-T. Wu *et al.*, *Nano Energy* **10**, 28-36 (2014).

Advanced X-ray fluorescence analysis of Cu(In,Ga)Se₂ cross sections

Philipp Schöppe, Claudia S. Schnohr, Michael Oertel, Ellen Butz, Sven Schönherr, Andreas Johannes, Stefanie Eckner, Manfred Burghammer¹, Gema Martínez-Criado¹, Udo Reislöhner, and Carsten Ronning

¹ European Synchrotron Radiation Facility, B.P. 220, F-38043 Grenoble Cedex, France

Chalcopyrite type Cu(In,Ga)Se₂ thin film solar cells have recently closed the gap to silicon based technologies after a record efficiency of 22.3 % was reported. The absorber layer is typically inhomogeneous at different scales [1-5]. Compositional and structural properties of the absorber affect the solar cell performance [6]. In order to unravel the impact of inhomogeneity on the electrical properties and hence, on the conversion efficiency there is a strong need for spatially resolved investigations. In return we have introduced a new approach of measuring thin cross sectional lamellas of whole Cu(In,Ga)Se₂ solar cell devices via highly focused X-ray fluorescence analysis (XRF) [7]. This ensures a spatial resolution in the sub-micrometer range combined with excellent compositional analysis. The XRF measurements were performed at the ID13 beamline of the European Synchrotron Radiation Facility (ESRF). A spatial resolution of about 280 nm was achieved, which mainly was limited by the beam diameter. In order to further improve the spatial resolution we performed measurements at the ID16B-nano-analysis beamline of the ESRF, which was recently upgraded. Hereby a 29.3 keV X-ray beam was used. Hence, for all elements, which are present in our solar cells the characteristic K_α X-rays could be analyzed. Some results from these investigations are presented here.

The solar cells were prepared by a two stage sequential process which is described in principle in [8]. Further, the absorber

layer was exposed to a KF post deposition treatment. Subsequently, cross sectional lamellas were cut out of complete solar cell devices using a focused ion beam. The lamellas were milled to a final thickness between 200 to 300 nm ensuring a sufficient fluorescence signal and mechanical stability at once.

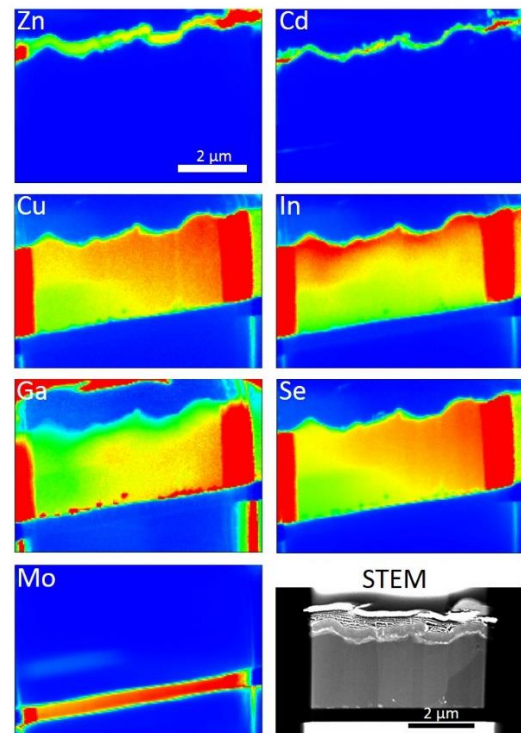


Fig. 1: Elemental maps of a Cu(In,Ga)Se₂ solar cell obtained by XRF are displayed together with the corresponding STEM image.

Fig. 1 shows the elemental maps of a complete Cu(In,Ga)Se₂ solar cell cross section together with the corresponding scanning transmission electron microscopy (STEM) image. All elements, which are

typically present in a Cu(In,Ga)Se₂ solar cell are detected and can be clearly assigned to the different layers of the solar cell. The only exception here are the light and/or lowly concentrated elements such as S and Na. As it can be seen in the elemental maps every absorber element shows lateral inhomogeneity, which may also come from variations of the lamella thickness. By calculating ratios like e.g. [Cu]/([In]+[Ga]) or [Ga]/([In]+[Ga]) these thickness effects can be neglected.

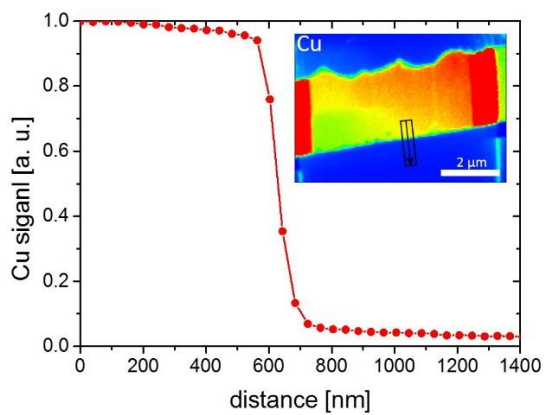


Fig. 2: Line scan with a width of 400 nm was extracted from the Cu map (shown in the inset).

In order to determine the spatial resolution the very sharp edge between the Cu signal and the back contact was used. From this area a line scan with a width of 400 nm was extracted. The clear transition from the absorber to the back contact shown by the drop in the Cu signal is depicted in **Fig. 2**. By calculating the derivative of this edge and fitting a Gaussian function on it one obtains the spatial resolution, which is the full width at half maximum. For this particular sample a spatial resolution of (98.4 ± 1.2) nm was achieved. That is an improvement by a factor of three to previous measurements [7]. By applying that improved spatial resolution with the already excellent concentration analysis it

was now possible to observe compositional variations at grain boundaries. It was found that for some grain boundaries the concentration of Cu is depleted.

References

- [1] U. Rau et al., Appl. Phys. A **96**, 221 (2009).
- [2] U. Reislöhner and C. Ronning, Appl. Phys. Lett. **100**, 252111 (2012).
- [3] C. S. Schnohr et al., Phys. Rev. B **85**, 245204 (2012).
- [4] S. Eckner et al., Appl. Phys. Lett. **103**, 081905 (2013).
- [5] Y. Yan et al., Appl. Phys. Lett. **87**, 121904 (2005).
- [6] D. Abou-Ras et al., Solar Energy Materials & Solar Cells **95**, 1452 (2011).
- [7] Ph. Schöppe et al., Appl. Phys. Lett. **106**, 013909 (2015).
- [8] M. Oertel and C. Ronning, J. Appl. Phys. **117**, 105302 (2015).

Activation of Al dopants in contacted ZnO nanowires

Davide Cammi, Michelle Geelen*, Andreas Johannes, Carsten Ronning

**Instituut voor Materiaalonderzoek, Martelarenlaan 42, 3500 Hasselt, Belgium*

Enhancement of the n-type conductivity of ZnO nanowires (NWs) by doping is essential for various applications, especially in transparent and flexible electronics. Among possible shallow donors in ZnO, Al is one of the most commonly used because of its large availability, low cost and non-toxicity.

Doping by ion beam implantation allows the introduction of the desired impurities in the semiconductor crystal beyond their solubility limit and ensures a homogeneous doping profile [1]. As a drawback, a large density of defects may be generated during the implantation process. This can dramatically alter the electrical properties of the implanted material. As such, post-implantation thermal treatments are typically performed, in order to recover the original crystal structure and to activate the implanted ions [2]. However, this is a critical issue in case of contacted nanowires, since at the high temperatures typically required for this purpose, effects such as alloying near the contact region [3], formation of new interface states [4] and eventually complete sample degradation [5] may occur. A detailed investigation of the thermal stability of Al implanted contacted ZnO nanowires is therefore required.

The nanowires were grown by the VLS method [6] and subsequently transferred to a new substrate (850 nm of SiO₂ on Si). After photolithography and metal deposition, the final samples consist of some nanowires bridging two Ti/Au electrodes (10nm/100nm).

The electrical properties of the samples were investigated by measuring their I-V

characteristics with a Source-Measure Unit (SMU) Keithley (Model 237).

The implantations were performed on the contacted nanowires using the implanter ROMEO. Ion energy and fluence were selected in order to obtain a doping concentration of 10¹⁹ cm⁻³ at depth of 100 nm. Additionally, similar samples were implanted with Ar with a comparable implantation profile, in order to separately investigate the effect of the influence of the generated defects on the electrical properties of contacted ZnO nanowires.

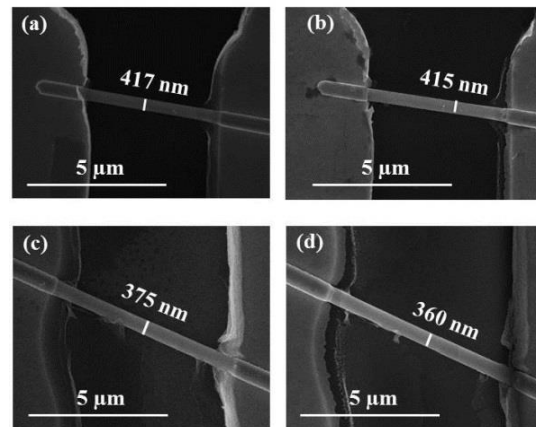


Fig. 1: SEM pictures of contacted ZnO nanowires before and after implantation with Al (respectively in (a) and (b)) and Ar (respectively (c) and (d)).

Scanning Electron Microscope (SEM) pictures (figure 1) reveal that the implantation process does not induce appreciable surface roughness, although a slight reduction of the nanowire diameter can be observed after Ar implantation due to sputtering.

The formation of a significant amount of defects during Ar implantation is proved by the drastic reduction of the conductivity in

the implanted samples after implantation, as shown in figure 2(b).

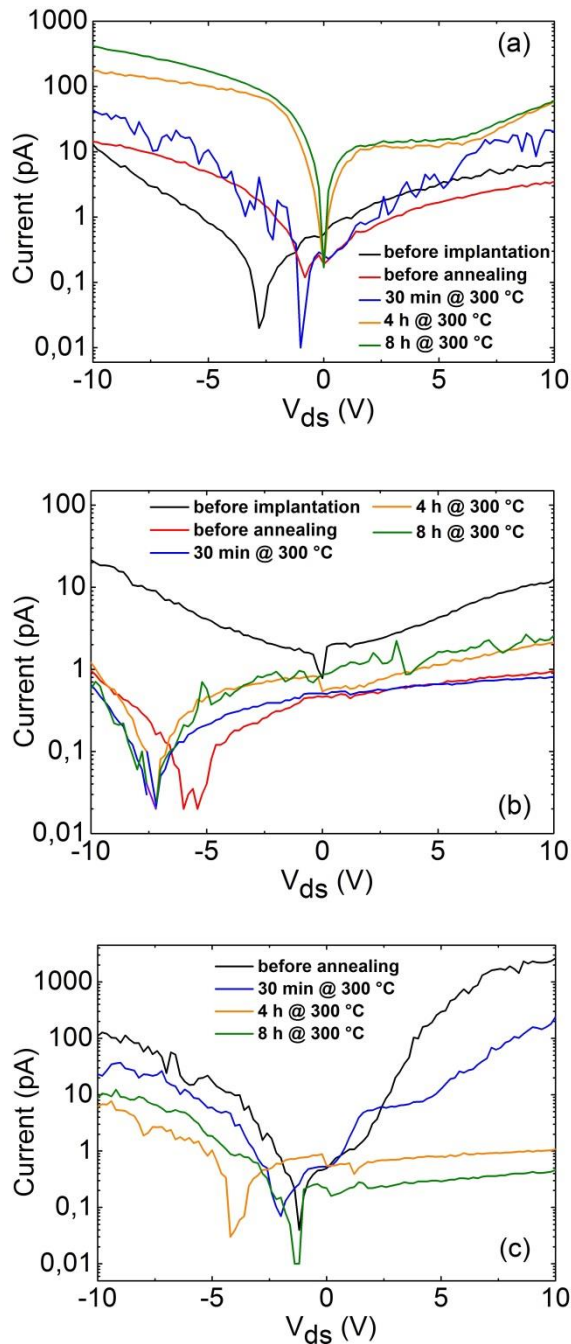


Fig. 2: I-V characteristics of contacted ZnO nanowires before and after Al (a) and Ar implantation (b) and following post-implantation annealing treatments. (c) I-V characteristics of a non-implanted reference sample.

The I-V characteristics of the sample after Al implantation are instead slightly improved (figure 2(a)), probably due to the

partial activation of Al ions as shallow donors.

Annealing of the Al implanted ZnO nanowires at 300 °C in air at atmospheric pressure for times longer than 30 minutes leads to progressive improvement of the I-V characteristics (figure 2(a)). The maximum increase of the sample conductivity is obtained after annealing for 8 hours. On the other hand, the conductivity of the Ar implanted sample is not recovered after analogous annealing procedures (figure 2(b)). Deterioration of the I-V characteristics is also observed in a non-implanted sample, which was annealed under the same conditions and used as a reference (figure 2(c)). The observed increase of the conductivity in Al implanted ZnO nanowires can be therefore entirely attributed to the activation of Al ions as shallow donors.

References

- [1] C. Ronning *et al.*, *Mat. Sci. Eng. R* **70**, 30-43 (2010).
- [2] S. Geburt, PhD Thesis, University of Jena, 2013
- [3] K. Ip *et al.*, *J. Cryst. Growth*, **287**, 149-156 (2006).
- [4] L. J. Brillson *et al.*, *J. Appl. Phys.*, **109**, 121301-33 (2011).
- [5] H.-K. Kim *et al.*, *Appl. Phys. Lett.*, **77**, 1647-1649 (2000).
- [6] C. Borschers *et al.*, *J. Phys. Chem. B*, **110**, 1656-1660 (2006).

Electroluminescence of single Eu implanted ZnO nanowires

Y. Haj Hmeidi, R. Röder, D. Cammi, and C. Ronning

Zinc oxide (ZnO) is a wide band gap (~ 3.37 eV at room temperature) semiconductor exhibiting a large exciton binding energy of 60 meV [1]. Furthermore, it is a good candidate to host rare earth ions, which show intra-shell transitions in the visible and infrared spectra range. Indeed photoluminescence studies of Europium (Eu) ions implanted single ZnO NWs reveal intense emission lines of intra-4f transitions at RT [2]. Although electroluminescence (EL) of RE doped ZnO bulk layer has been achieved by applying DC or AC voltage [3-6], the EL of single RE implanted ZnO nanowires remains a challenging task. We propose a new approach for EL devices based on single Eu implanted ZnO (ZnO:Eu) NW, and investigate the EL operation. Zinc oxide NWs were grown via

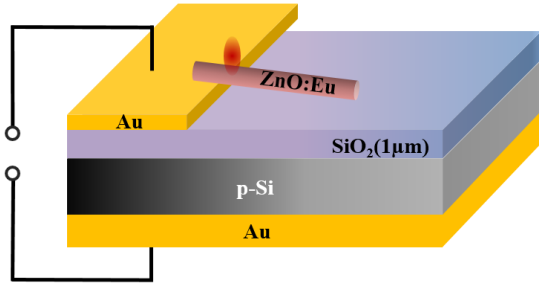


Fig. 1: Schematic showing the device structure based on single Eu doped ZnO NWs.

vapor transport following the VLS mechanism in horizontal tube furnace [3]. The NW ensemble was subsequently implanted with a fluence of $\Phi \geq 2 \times 10^{15}$ cm⁻³ of an ion energy of 200 keV. Afterwards ZnO:Eu nanowires were annealed at 700° C in air for 120 minutes in order to remove irradiation damage and create necessary Eu-O_i complexes [2]. Ultimately, the ZnO:Eu nanowires were

deposited directly onto samples, with defined contacts pads by an imprint technique. The contacts pads (10 nm Ti / 100 nm Au) were structured beforehand by photolithography. The final device structure is based on an additional isolating layer of SiO₂ (1 μm) between ZnO:Eu nanowires and the bottom electrode, resulting in a capacitor like architecture as it is illustrated in figure 1. The ZnO:Eu nanowires show EL at RT by applying an AC voltage square wave with voltages in the range of 5-9 V (0 to peak value), and frequencies in the range of 12.5-16.5 MHz. The EL occurs mainly at the interface between the ZnO:Eu and the contact pads in all devices. We characterized the EL of ZnO:Eu as a function of the applied frequency between 1 kHz - 20 MHz, while the peak voltage value was kept constant at $V_{0-p} = 5 \pm 0.25$ V. Results are shown in figure 2. The observed EL is clearly the 4f-intrashell transitions of Eu ions.

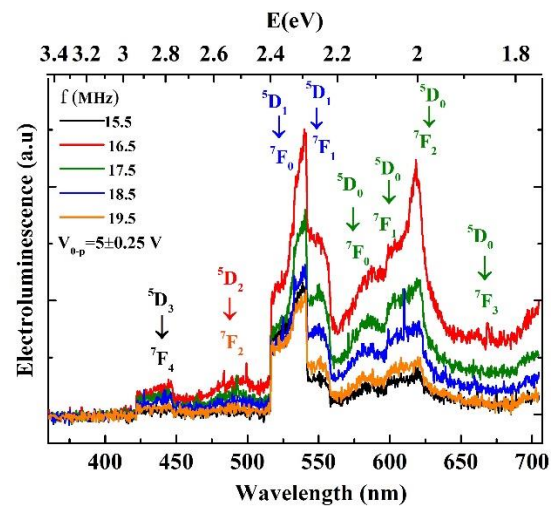


Fig. 2: Room temperature electroluminescence spectra for different of applied AC frequencies, while the peak voltage was kept constant at 5 V.

The transitions can be assigned to Eu in trivalent charged state according to literature [4-9]. The EL of Eu ions proves the success of the device fabrications. The spectral position of the Eu emission remains unchanged for different frequencies. Several ZnO:Eu nanowire devices show qualitatively similar EL spectra. In addition all ZnO:Eu show a maximum of EL at frequency of 15.5-17.7 MHz as it is shown in figure 3. This frequency is not related to theoretical resonance frequency of the equivalent RC circuit, which was calculated to be about 90 MHz. Furthermore, we investigated

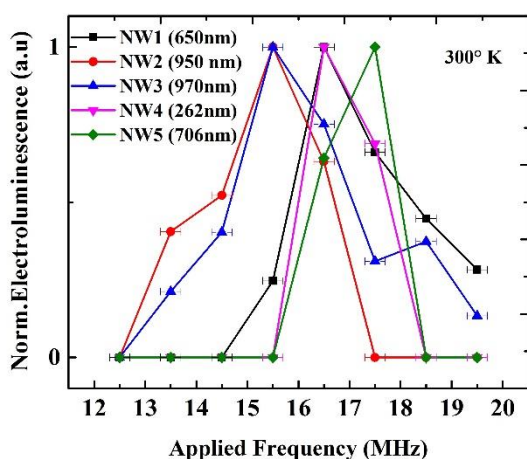


Fig. 3: Electroluminescence intensity for different ZnO:Eu nanowires as function of applied AC frequency. The peak voltage was kept constant at 5 V. The EL spectrum of NW1 is present in figure 2.

the EL dependence on the applied peak voltage between 4-10 V at fixed frequency of 12.5 ± 0.2 MHz. EL spectra of one ZnO:Eu NW device are depicted in figure 4. All ZnO:Eu NW devices show optimal EL at a peak voltage of 7.5-9.5 V. Although, there is no clear correlation between the diameter of ZnO:Eu nanowires and their EL, the ZnO:Eu nanowire with diameter thicker than 650 nm seems to exhibit a lower threshold frequency and peak voltage (see figure 3).

Note, that there is no EL observed from the near-band edge transitions of ZnO. We suggest that the mechanism of excitation is direct-impact ionization of luminescence centers of the Eu by hot electrons injected from the gold electrode.

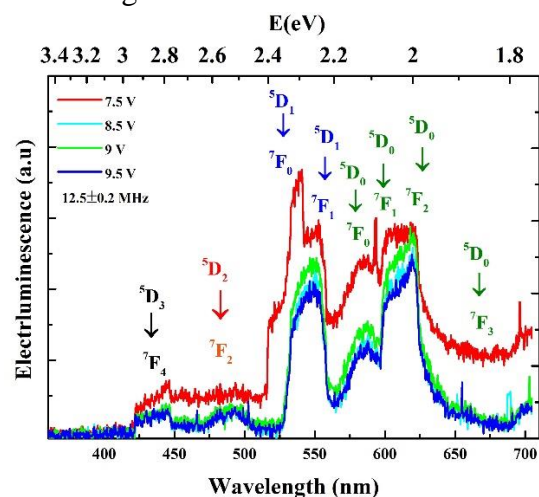


Fig. 4: Room temperature EL spectra for different applied AC peak voltages. The frequency was kept constant at 12 MHz. The data was acquired for NW1 in figure 3.

In summary, we investigated the EL of single ZnO:Eu nanowires at RT. and its dependence on the applied frequencies and voltages. The most likely mechanism is direct-impact ionization by hot electrons.

References

- [1] S. Liu, et al., *Adv. Mater.* **21**, 1217 (2009).
- [2] S. Geburt, et al., *Nano Letters* **14**, 4523 (2014).
- [3] Borchers C, et al., *J. Phys. Chem. B* **110**, 1656–60 (2006).
- [4] S. Iwan, et al. *Materials Science in Semiconductor Processing* **30**, 263 (2015).
- [5] S. Bachir et al, *J. Phys. Chem. Solids* **57**, 1869 (1996).
- [6] S.A.M. Lima, et al., *Applied Physics Letters* **90**, 023503 (2007).
- [7] Yang, et al., *Adv. Optical Mater.* **2**, 240 (2014).
- [8] Wang, et al., *J. Phys. Chem. C* **115**, 22729 (2011).
- [9] Chen, et al., *Journal of Alloys and Compounds* **431**, 317 (2007).
- [10] U. Vetter, PhD Thesis, University of Göttingen (2003).

Investigations of the electroluminescence of single Eu ion implanted ZnO nanowires at room temperature

Y. Haj Hmeidi, R. Röder, A. Johannes, and C. Ronning

Electroluminescence (EL) of single Eu ion implanted Zinc oxide nanowires (ZnO:Eu) was achieved by utilizing a new approach, where the final device structure is based on an isolating layer of SiO₂ (1 μm) between a single ZnO:Eu nanowire and a bottom electrode, resulting in the capacitor-like architecture. This is illustrated in figure 1. Applying an AC voltage square wave to the devices, leads to EL from the ZnO:Eu nanowires. EL occurs mainly at the interface between the gold electrode and the ZnO:Eu NW, as it is shown in figure 1. We investigated the EL operation for two electrodes of different size, this leads to two different theoretical capacitances, which were calculated to be C₁ ≈ 1.5 pF, and C₂ ≈ 15 pF. For both types of devices, we investigated the EL dependence on the applied AC voltage signal with frequencies between 1 kHz and 20 MHz at fixed peak voltage of V_{0-p} = (5±0.3) V. Several ZnO:Eu nanowire with different capacitance were investigated. All ZnO:Eu nanowire devices show qualitatively similar EL spectra. One example is shown in figure 2, and this dev-

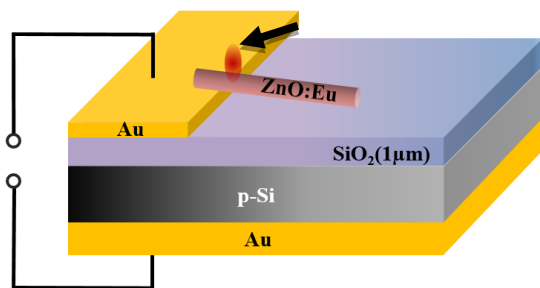


Fig.1: Schematic showing the device structure based on single Eu doped ZnO NWs. The red spot represents the position of electroluminescence spot.

ice has a capacitance of C₂ ≈ 15 pF. The acquired EL is the 4f-intershell transitions of Eu ions. The transitions can be labeled according to literature [1-8]. In both types

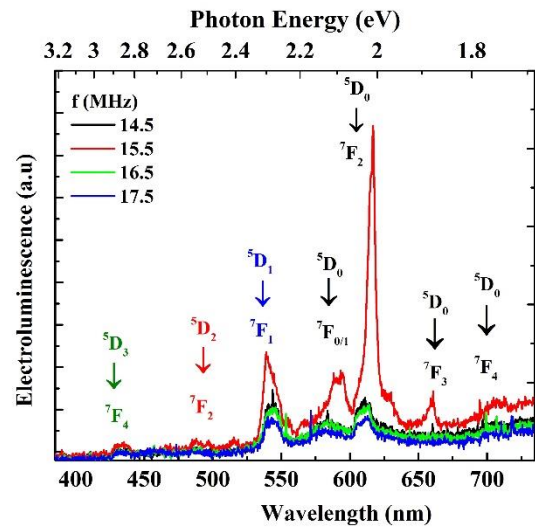


Fig.2: Electroluminescence spectra as a function of applied AC signal. The peak voltage was kept constant at 5 V.

of devices, EL exhibits a maximum at the frequency of 15-17 MHz, as it shown in figure 3. This frequency position is different from theoretical resonance frequency of the equivalent RC circuit, which was estimated to be about 90 MHz. Clearly, changing the capacitance of the ZnO:Eu nanowire devices does not change the frequency of the maximum observed EL. Additionally, three different waveforms were applied to one ZnO:Eu nanowire device at the same frequency and peak voltage, as it is shown in figure 4. Obviously the most intense EL is obtained by applying a square waveform. The harmonic drop in the applied peak voltage is important for EL operation. Furthermore, we investigated the EL

dependences on the applied peak voltage between 4-10 V at fixed frequency of 12.5 ± 0.2 MHz.

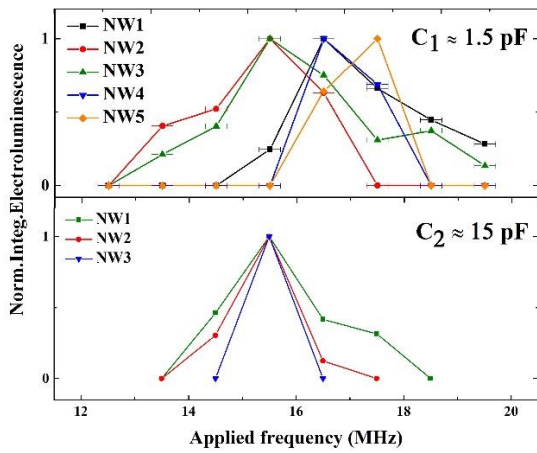


Fig.3: EL intensity for different ZnO:Eu nanowires as a function of the applied AC signal. The peak voltage was kept constant at 5 V. Two types of devices, with $C_1 \approx 1.5$ pF and $C_2 \approx 15$ pF. The EL spectrum of NW1 with $C_2 \approx 15$ pF is present in figure 2.

The intensity of EL in all ZnO:Eu nanowire devices shows qualitatively similar behavior. The EL exhibits a maximum around a peak voltage of 8 V. One example is shown in figure 4. This device has an estimated capacitance

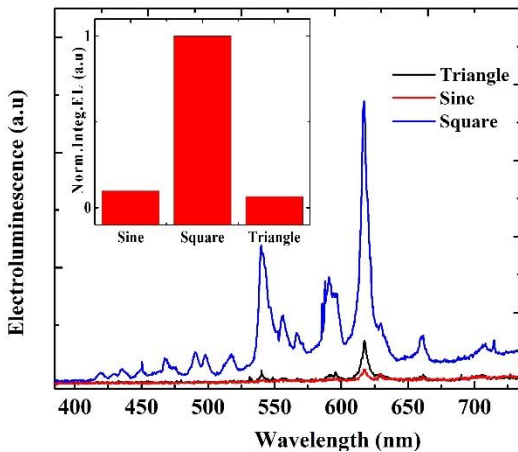


Fig.4: EL spectrum of one ZnO:Eu nanowire device. AC signal with Square, triangle and sine waveform were applied to the device. The frequency and peak voltage were kept at 15.5 MHz and 5 V. Inset shows the integrated EL intensities when applying different signal waveforms.

of $C_2 \approx 15$ pF. It is presumed, that increasing the peak voltage at this high frequency, increases the leaking current through the isolating layer of SiO₂. In this case less electrons contribute to EL processes. Eventually, the EL decreases by applying higher peak voltage.

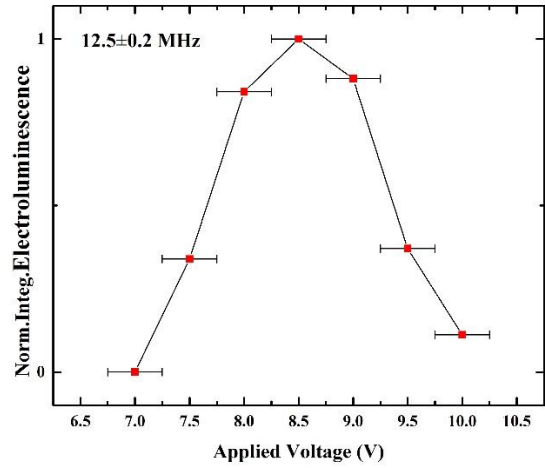


Fig.5: EL intensity as function of applied AC peak voltage. The frequency was kept constant at 12.5 MHz. capacitance is $C_2 \approx 15$ pF. The EL spectrum is present in figure 2.

In summary, changing the capacitance of single ZnO:Eu nanowire by a factor of 10 does not change the frequency of the maximum EL. Furthermore, the optimal AC signal has a square waveform, in order to obtain the most intense EL.

References

- [1] S. Geburt, *et al.*, Nano Letters **14**, 4523 (2014).
- [2] S. Iwan, *et al.* Materials Science in Semiconductor Processing **30**, 263 (2015).
- [3] S. Bachir, C. Sandouly, J. Kossanyi, and J. C. Ronfard-Haret, J. Phys. Chem. Solids **57**, 1869 (1996).
- [4] S.A.M. Lima, *et al.*, Applied Physics Letters **90**, 023503 (2007).
- [5] Yang, *et al.*, Adv. Optical Mater. **2**, 240 (2014).
- [6] Wang, *et al.*, J. Phys. Chem. C **115**, 22729 (2011).
- [7] Chen, *et al.*, Journal of Alloys and Compounds **431**, 317 (2007).
- [8] U. Vetter, PhD Thesis, University of Göttingen (2003).

Investigation of the Potassium-Doping of Tetraphenyldibenzoperiflanthene (DBP) on Ag(111) by Photoelectron Spectroscopy

Felix Otto, Christian Udhardt, Tino Kirchhübel,
Bernd Schröter, Roman Forker, and Torsten Fritz

Tetraphenyldibenzoperiflanthene (DBP, $C_{64}H_{36}$) is a candidate for future application in organic electronics. This red dye molecule consists of an aromatic backbone with four nearly perpendicularly oriented phenyl groups [1]. For any applications it is crucial to control its electronic and optical properties, for example by alkali metal doping. We have analyzed the impact on these properties upon potassium doping for DBP thin films on Ag(111) on the one hand using *in situ* differential reflectance spectroscopy (DRS) and on the other hand by means of ultraviolet and x-ray photoelectron spectroscopy (UPS, XPS).

The surface of the Ag(111) single crystal was cleaned by three cycles of Ar-sputtering and subsequent annealing at 500 °C. Organic molecular beam epitaxy was used to grow the DBP films in ultra-high vacuum ($<10^{-9}$ mbar) at a rate of ≈ 0.2 ML/min. Potassium was deposited from a dispenser source (SAES getters) on a freshly prepared DBP sample to avoid degradation effects.

The sample preparation was monitored by *in situ* DRS to control the film thickness and, in the case of alkali metal doping, the change of the optical properties. These quantities are observable due to changes of the reflectivity R

$$DRS(E, d) = \frac{R(E, d) - R(E, 0)}{R(E, d)}$$

E is the energy of the incident light and d denotes the film thickness. Further information on this method are given in refs. [2, 3]. The photoelectron spectroscopic measurements were done after transferring the sample to our surface analysis facility

without breaking the ultra-high vacuum. UPS spectra were taken with p-polarized He I α radiation (21.218 eV), whereas Al K α (1486.71 eV) was used for XPS.

The orange curve in Fig. 1 shows the final DRS measurement after the growth of 3 monolayer equivalents (MLE) of DBP on Ag(111). There are two neutral DBP species named low (LE) and high energy (HE) which are determining the shape of the spectrum [4].

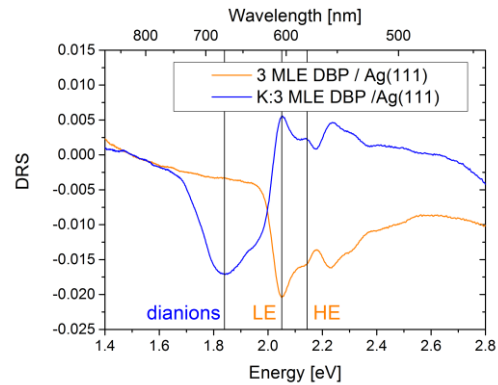


Fig. 1: Comparison of the final *in situ* DR spectra of 3 MLE DBP on Ag(111) (orange) and the potassium deposition on the same sample (blue). DBP dianions are developing during the doping process, whereas the LE- and HE-species of the neutral molecule decrease in intensity.

The blue curve in Fig. 1 shows that the mentioned LE and HE species become weaker due to the deposition of potassium. Furthermore, the optical signature of DBP dianions appears with a 0.2 eV lower optical gap [5]. Nevertheless, no structural rearrangement was observed by low energy electron diffraction (LEED). Based on this different experimental observations, investigations with photoelectron spectroscopy

are interesting to study structural and electronic properties. We determined the amount of potassium on the sample using the relative intensities of the K 2p and C 1s state in XPS (Fig. 2).

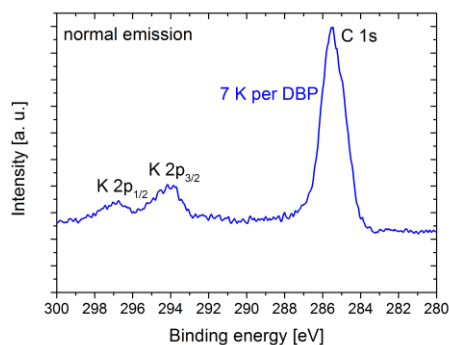


Fig. 2: Al K_{α} XPS spectrum of K:3 MLE DBP on Ag(111) in normal emission focusing on the K 2p and C 1s region. The evaluation of the relative intensities gives an amount of 7 K atoms per DBP molecule.

A calculated K-to-DBP ratio of 7 is higher than necessary to cause dianions, if we assume an integer charge transfer from K to DBP. This indicates either a partial charge transfer to DBP or the occurrence of potassium clusters on the sample.

The second option is rather unlikely, since there is no component in the K 2p spectra corresponding to a K-Ag bond or free potassium. Furthermore, work function measurements show no evidence for an inhomogeneous sample. Large clusters of potassium between DBP molecules are therefore unlikely.

Doping induced modifications of the molecular electronic structure play a crucial role for potential technical applications. We investigated the influence of K deposition on the frontier orbitals by means of UPS (Fig. 3). The undoped DBP layer has a hole injection barrier (onset of the HOMO) of 1.7 eV. This value is significantly reduced to 0.2 eV upon doping.

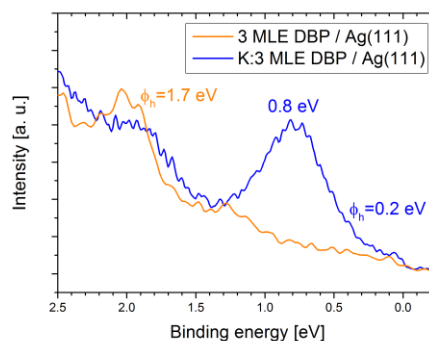


Fig. 3: He I α UPS spectra of undoped and doped 3 MLE DBP on Ag(111) in the HOMO region. A new peak at 0.8 eV evolves due to K deposition. The hole injection barrier ϕ_h decreases from 1.7 to 0.2 eV.

The reason for this effect is a new peak arising at 0.8 eV, which can be assigned to the now filled former lowest unoccupied molecular orbital (LUMO) of the undoped DBP molecule. This is consistent with the molecular dianions observed with DRS. The UP spectra show no hint of electronically neutral potassium, which is expected to cause a peak at about 0.4 eV [6].

In conclusion, we were able to study the optical and electronic properties of DBP dianions on Ag(111) originating from K-doping. A partial charge transfer from the alkali metal atoms to molecules occurs, strongly affecting the electronic structure in the HOMO region.

References

- [1] J. D. Debad *et al.*, J. Am. Chem. Soc. **118**, 2374 (1996).
- [2] R. Forker and T. Fritz, Phys. Chem. Chem. Phys., **11**, 2142-2155 (2009).
- [3] R. Forker *et al.*, Annu. Rep. Prog. Chem., Sect. C: Phys. Chem., **108**, 34-68 (2012).
- [4] T. Kirchhübel *et al.*, Langmuir, (2016) submitted.
- [5] T. Kirchhübel, Master's thesis, Friedrich-Schiller-University Jena (2014)
- [6] L.-G. Petersson and S.-E. Karlsson, Phys. Scr. **16**, 425 (1977).

Commensurism at Electronically Weakly Interacting Phthalocyanine/PTCDA Heterointerfaces

Marco Gruenewald, Christoph Sauer¹, Julia Peuker, Matthias Meissner, Falko Sojka, Achim Schöll¹, Friedrich Reinert¹, Roman Forker, and Torsten Fritz

¹Universität Würzburg, Experimentelle Physik VII & Röntgen Research Center for Complex Material Systems RCCM, 97074 Würzburg, Germany

Organic thin films have been already established in many applications such as field effect transistors (OFET), light emitting diodes (OLED), and photovoltaic devices (OPVD). Recently, organic quantum well structures (OQW) attract much interest as they could play a central role in advanced organic-based applications like organic lasers and multi-level logical circuits [1-3]. The broad application of OQWs is still hindered by demanding preparation conditions, namely the need for both a high crystalline quality and well defined interfaces.

In the literature molecular adsorption is often distinguished as either physisorptive or chemisorptive which can be regarded as two extrema on the scale of the bonding strength. The main difference is that the latter case involves the formation of (partly) covalent bonds between substrate and adsorbate which is manifested by a significant hybridization of electronic states and/or charge transfer (CT). There are numerous examples in literature where the occurrence of commensurism is directly related to or even regarded as a univocal proof of a strong interaction between adsorbate and substrate [4-6].

From our point of view this is a prevalent misunderstanding, based on the disregard that {i} the (lateral) forces which adjust the adsorbate species in a certain registry with the substrate depend on the derivative of the interface potential, i.e., the corrugation, not its average value, and {ii} the

overwhelming part of a strong adsorbate-substrate interaction can be non-site-specific [7].

We elucidate here that commensurism at organic-organic heterointerfaces may also occur for physisorbed (i.e., electronically weakly interacting) systems lacking appreciable signs for charge transfer or hybridization. To demonstrate this, we structurally characterized a tin(II)-phthalocyanine (SnPc) ML deposited on top of a PTCDA ML on Ag(111) by low energy electron diffraction (LEED) and low temperature scanning tunneling microscopy (LT-STM).

In Fig. 1 (a) a LEED image of 1 ML SnPc on 1 ML PTCDA/Ag(111) is shown. We fitted numerically a reciprocal lattice to the LEED data using all spots stemming from the SnPc overlayer simultaneously except for those very close or identical to PTCDA spots. According to the fitting procedure, we found a commensurate registry between the SnPc and PTCDA lattices in the temperature range from 300 K to approximately 20 K.

In order to determine the adsorption geometry of individual molecules of the SnPc adlayer we acquired LT-STM images. Figure 1 (b) depicts an overview scan showing unoccupied states predominantly located at the tin atoms. The Sn-up and Sn-down configurations, which are possible because of the non-planarity of SnPc, are clearly discernible. We found 6 SnPc molecules in the unit cell, where 4

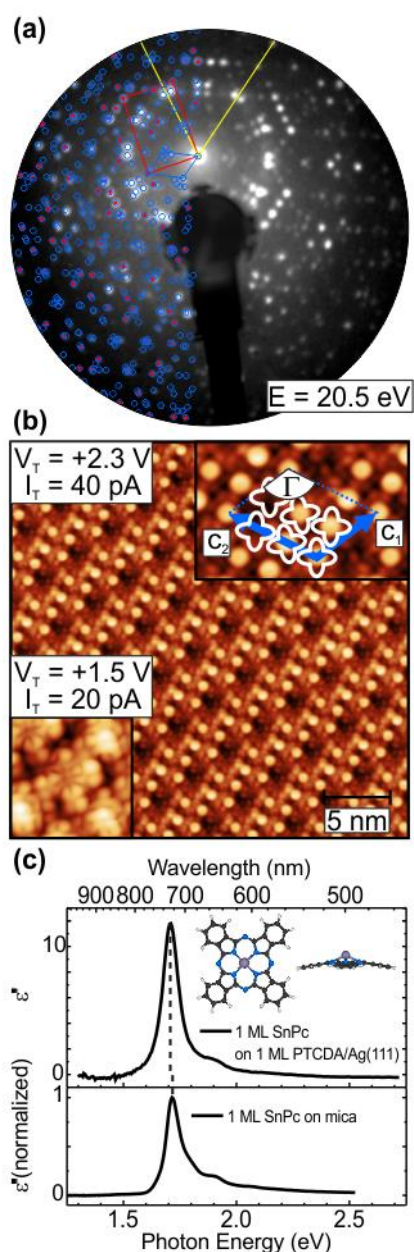


Fig. 1: (a) LEED and (b) STM images of a SnPc ML on top of 1 ML PTCDA / Ag(111). The imaginary part of the dielectric function ϵ'' extracted from DRS data is shown in the upper part of (c). For comparison, ϵ'' for SnPc on inert mica is shown in the lower part of (c). The non-planar molecular structure of SnPc is shown in the inset in (c).

are in Sn-up and 2 are in Sn-down configuration.

The molecular motif is very different from any arrangement of SnPc in the known 3-dimensional bulk structures [8]. Most likely, the regular arrangement of Sn-up and Sn-down molecules is caused by different

adsorption sites on PTCDA. We further acquired high-resolution LT-STM images that clearly feature submolecular resolution with distinct nodal lines in the orbital structure as shown in the inset in Fig. 1 (b). A similar contrast has been reported previously for electronically decoupled phthalocyanines [9].

In order to analyze the bonding strength *in situ* differential reflectance spectroscopy (DRS) is applied [10]. For a SnPc ML on 1 ML PTCDA on Ag(111) we find no indication for a chemisorptive bonding between the stacked organic layers because the spectral character of the optical absorption resembles that of non-hybridized molecules as observed likewise on an inert substrate, cf. Fig. 1 (c). Strictly speaking, we observe monomer behavior owing to a sharp peak at 1.71 eV followed by a small shoulder at 1.87 eV. We thus conclude that electronic interactions with the PTCDA interlayer are minor at most.

Our findings contravenes the aforementioned assumption, namely that the strength of the adsorbate-substrate interaction in the field of organic based interfaces can be directly related to the type of epitaxy.

References

- [1] Faist *et al.*, Science **264**, 553-556 (1994)
- [2] Lindner *et al.*, Appl. Phys. Lett. **93**, 233305 (2008)
- [3] Wang *et al.*, Adv. Mater. **26**, 4582-4587 (2014)
- [4] Umbach *et al.*, Phys. Status Solidi B **192**, 389-406 (1995)
- [5] Umbach *et al.*, Appl. Phys. A **63**, 565-576 (1996)
- [6] Hao *et al.*, J. Chem. Phys. **134**, 154703 (2011)
- [7] Mannsfeld and Fritz, Mod. Phys. Lett. B **20**, 585-605 (2006)
- [8] Friedel *et al.*, J. Chem. Soc. D 400-401 (1970)
- [9] Cheng *et al.*, Surf. Sci. **605**, 415-418 (2011)
- [10] Forker *et al.*, Annu. Rep. Prog. Chem., Sect. C: Phys. Chem. **108**, 34-68 (2012)

Electronic structure of one monolayer DBP on HOPG

Tobias Huempfer, Tino Kirchhübel, Roman Forker, Noriaki Kawakita*, Takashi Yamada*, Toshiaki Munakata*, and Torsten Fritz

*Department of Chemistry, Graduate School of Science, Osaka University, 1-1 Machikaneyama, Toyonaka 560-0043, Osaka, Japan

The organic dye molecule tetraphenyl-dibenzoperiflanthene (DBP, $C_{64}H_{36}$) consists of an aromatic backbone and four additional phenyl rings [1]. Recently, it has attracted attention for usage in optoelectronic devices due to its ability to customize the electronic structure as well as the molecular light absorption and emission.

For the investigations of the electronic structure two photon photoemission (2PPE) experiments were performed. In this method the sample is irradiated by laser light with tunable wavelength. For this experiment the third harmonics were used. The emitted electrons are measured by a commercial electron analyzer. Within the sample two processes can occur. On the one hand an electron in an *occupied* state can absorb two photons and can be directly lifted above the vacuum level. Those states occur at the same energy in the *initial* energy scale for different wavelengths of the incoming light. On the other hand an electron can be lifted to a formerly unoccupied state by a first photon, and then be lifted over the vacuum level by a second photon. In this case the energetic position of *unoccupied* states can be detected, which appear at the same energetic positions in the *intermediate* energy scale.

The highly oriented pyrolytic graphite (HOPG) substrate was brought into a UHV chamber with a base pressure of 10^{-9} mbar. After several annealing cycles at about 500 °C one monolayer (ML) of the DBP molecule was evaporated onto the substrate at room temperature.

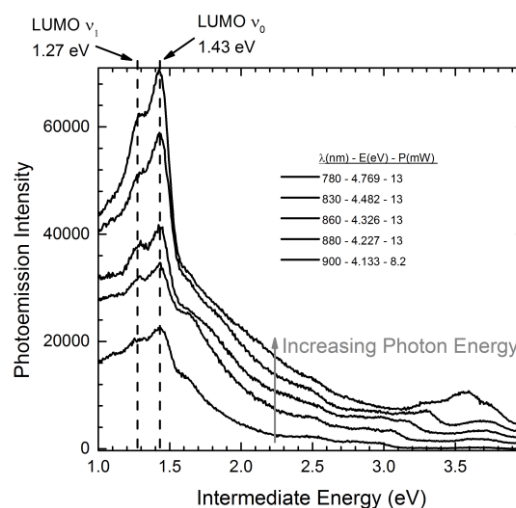


Fig. 1: Wavelength dependent 2PPE measurements of 1 ML DBP on HOPG in the intermediate energy-scale.

The spectra in Fig. 1 show an intense peak at 1.43 eV that does not change its energetic position for different photon energies in the intermediate scale. Therefore it can be concluded that it originates from an unoccupied electronic state. By comparison to DFT calculations this peak can be assigned to the LUMO of the DBP molecule. The additional shoulder at 1.27 eV most likely originates from the first vibronic progression of the LUMO.

The intensity of both peaks is increasing with increasing photon energy of the incoming light. This effect arises from the fact that for higher photon energies there are more electrons available that can be lifted from occupied states to the LUMO, because the energy is high enough to transfer electrons from deeper molecular orbitals.

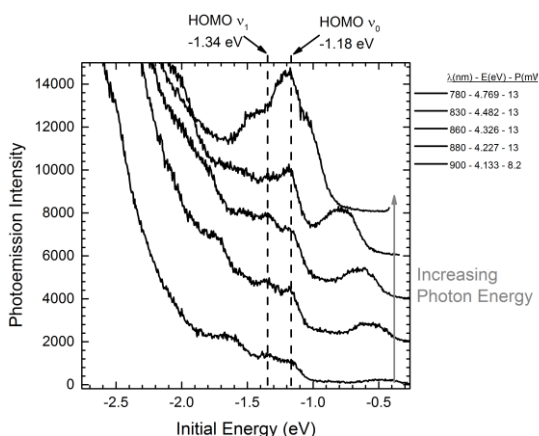


Fig. 2: Wavelength dependent 2PPE measurements of 1 ML DBP on HOPG in the initial energy-scale.

Having a closer look at the energy region shown in Fig. 2 in the initial energy scale one can see that there are two peaks at -1.18 eV and -1.34 eV that do not change position in this scale upon altering the laser wavelength. Comparing these energetic positions with UPS data of this system [2], the peak at -1.18 eV can be assigned to the HOMO of DBP. The lower energy peak at -1.34 eV then originates from the first vibronic progression of the HOMO of the DBP molecule.

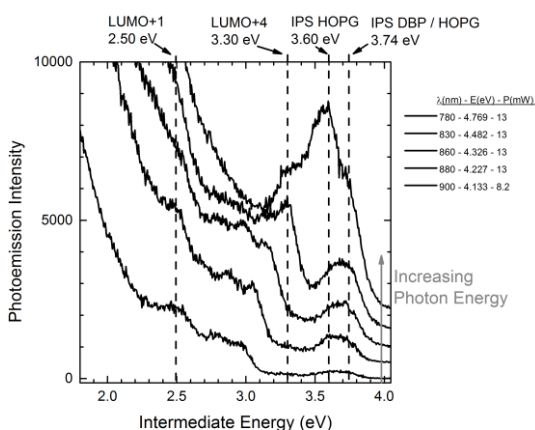


Fig. 3: Wavelength dependent 2PPE measurements of 1 ML DBP on HOPG in the intermediate energy-scale (Zoom of Fig. 1).

The spectrum in Fig. 3 shows the region around the image potential state (IPS) again in the intermediate energy for different laser energies. The IPS state itself seems broadened compared to the bare substrate (not shown). This arises from the fact that there are parts of the sample covered by DBP molecules and still some remaining bare substrate areas available.

Another peak is visible in the spectrum at 2.50 eV that does not change its position upon altering the laser wavelength. From DFT calculations it can be assigned to the unoccupied LUMO+1.

In the 2PPE spectra recorded with a photon energy of 4.482 eV (830 nm) and higher an additional peak appears at 3.30 eV, which does not occur for lower photon energies. Due to the energetic position, this peak can be assigned to the LUMO+4 of DBP by comparing it with the DFT calculation. This feature can only be measured when the photon energy is high enough to lift an electron from the HOMO to the former unoccupied LUMO+4, which is only possible for photon energies higher than the aforementioned.

The LUMO+2 and LUMO+3 cannot be identified in the measured data, because in this energy region the peak of the occupied HOMO and its vibronic progression are located.

In the presented work we investigated the electronic structure of 1 ML DBP on HOPG via 2PPE. All emerging features could be labeled by comparing it to DFT calculations and UPS data.

References

- [1] J. D. Debad *et al.*, *J. Am. Chem. Soc.* **118**, 2374-2379 (1996).
- [2] S. Kera *et al.*, unpublished.

Planar Hybrid Josephson Junctions on FeSe_{0.5}Te_{0.5} Thin Films

S.Döring, S. Schmidt, V. Tympel, F. Schmidl, S. Kawale, E. Bellingeri*, and P. Seidel*

**CNR-SPIN, Corso Perrone 24, I-16152 Genova, Italy*

For the investigation on iron-based superconductors (FBS) we designed a layout for the preparation of planar hybrid Josephson junctions. It allows an universal use of different materials and classes of FBS as base electrode as well as differently conducting materials as barrier to prepare junctions either of SNS', SNIS' or SIS' type. Additionally to our former investigations on Co:BaFe₂As₂, an 122-type FBS, in this report we will present results based on thin films of the 11-type FBS FeSe_{0.5}Te_{0.5} [1] using the same junction design. Our investigations include the observation of Josephson effect and Andreev reflection studies, respectively.

The design of the junction and its preparation is well described in [2,3] and excepts of the change of base electrode material we use the same kind here, with a sputtered Gold barrier ($d=5\text{nm}$) and a counter electrode of thermally evaporated Pb, covered by an In protection layer.

Using quasiparticle spectroscopy one is able to get information about the order parameter of the FBS, e.g. its symmetry, the number, structure and value of the superconductor gaps. Usually analysis of spectra is done by the BTK-model [4], but there are other extending models taking the specific multiband character of FBS into account like [5].

A typical spectrum is shown in fig 1. Its shape is far away from usual one-gap s-wave superconductors. Typically and also observed for the 122-type FBS [6] is the triangular shape of the central peak. Additionally one can observe side dips, which are possible features in spectra of

s+- superconductors within the Golubov model [5]. Similar ones were observed by other groups for 11 compounds [7,8], however we did not so for 122-type, yet. This spectra give a clear indication of the unconventional nature of 11-type FBS and FBS in general, respectively.

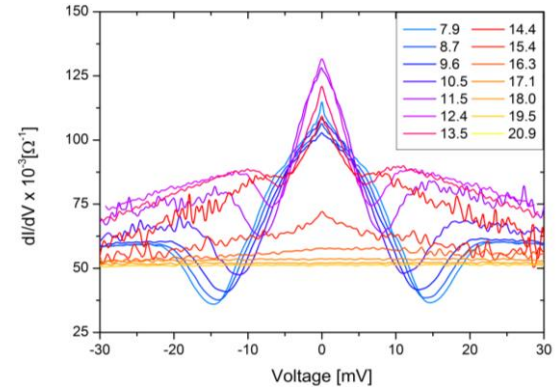


Fig. 1: Quasiparticle spectra of a $3\mu\text{m} \times 3\mu\text{m}$ junction at temperatures between 7.9K (cyan) and 19.6K (yellow).

The second method, one which we are more focused is the Josephson effect using the overlap of Cooper pair waves between the two electrodes. A Josephson junction can be described by the RSJ-model consisting of the junction with critical current I_c , parallel shunted by an ohmic resistance R_n , which are the characterising parameters.

A first example of an I-V characteristic is shown in fig. 2. Its behaviour differs from standard RSJ-like, which predicts $V \sim (I^2 - I_c^2)^{0.5}$. As clearly visible the observed shape is nearly linear for $I > I_c$ here. This can be explained by the existence of two parallel mechanism for current transport, as described by Saitoh et al. [9]. One is the RSJ-like Josephson effect, the other one a flux flow over the junction, usually given by $I \sim \tanh(V)$. If the weighting of both is

nearly equal, a linear shape is the consequence. The assumption of a flux flow behaviour can be supported by fig. 3. Again an I - V characteristic is shown, but for a junction with much bigger area. This favours the flux flow over RSJ-like Josephson effect. Thus the shape of the I - V characteristic is rather completely formed by flux flow. Since the smallest junction presented in fig. 1 of this work does not show a Josephson-like behaviour, one could assume, that there is a critical dimension to be exceeded for occurrence of Josephson effect, but also the influence of flux flow grows significantly faster than the RSJ-like Josephson effect. The finding of optimal parameters of junction area and barrier thickness for the observation of mostly pure RSJ-like behaviour should be the task for future work.

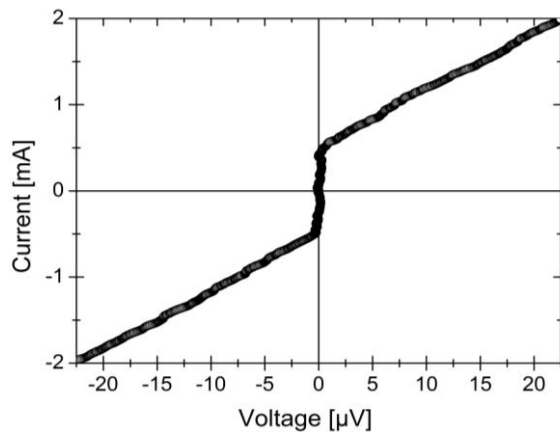


Fig. 2: Current-Voltage characteristic of a junction with an area of $10\mu\text{m} \times 10\mu\text{m}$ at $T=4.2\text{K}$.

From the given I - V characteristic in fig. 2 one could obtain the characteristic parameters $I_c=440\mu\text{A}$ and $R_n=20\text{m}\Omega$. The temperature dependence of the corresponding I_cR_n -product is shown in fig. 4. Due to a strong variation of I_c in different curves, it is very noisy. Noticeable is the difference between the positive and negative current branch at temperatures close to T_c . Nevertheless a fit within the Apostolov-model [10] was

possible. This model is based on the proximity effect, occurring in the non-superconducting barrier layer.

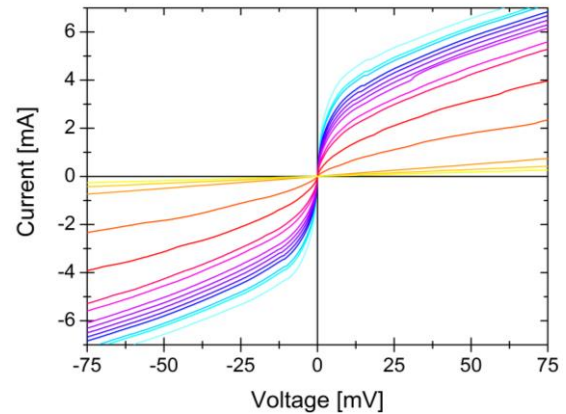


Fig. 3: Current-Voltage characteristic of a junction with an area of $100\mu\text{m} \times 100\mu\text{m}$ at temperatures between 4.2K (cyan) and 17.4K (yellow)

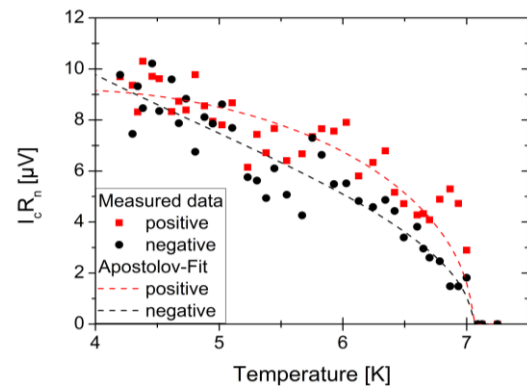


Fig. 4: Temperature dependence of the I_cR_n product obtained from the junction in fig. 2.

References

- [1] E. Bellingeri *et al.* Appl. Phys. Lett. **96** 102512 (2010)
- [2] S. Döring *et al.* Physica C **478**, 15 (2012).
- [3] S. Schmidt *et al.* Appl. Phys. Lett. **97**, 172504 (2010)
- [4] G. E. Blonder, M. Tinkham, and T. M. Klapwijk Phys. Rev. B **25**, 4515 (1982)
- [5] A. A. Golubov *et al.* Phys. Rev. Lett. **103**, 077003 (2009)
- [6] S. Döring *et al.* Institute report 2014, 88
- [7] N. Fujioka *et al.* Physica C **518**, 28 (2015)
- [8] Y.T. Shen *et al.* J. Appl. Phys. **114**, 123912 (2013)
- [9] Saitoh *et al.* Jap. J. Appl. Phys. **36**, 272 (1997)
- [10] S. Apostolov and A. Levchenko Phys. Rev. B **86**, 224501 (2012)

Measuring the photo-elastic coefficients of silicon at 1550 nm by means of a rotating wave plate polarimeter

René Glaser, Christian Schwarz, Daniel Heinert and Ronny Nawrodt

To detect gravitational waves, predicted by Albert Einstein within his well-known General Relativity [1], has been one of modern day physics great goals, which was recently reached by both LIGO detectors [2]. For detecting these small disturbances of space-time, interferometric gravitational wave detectors, based on Michelson-like setups, are being used (see [3] for example). Some of the advanced interferometric gravitational wave detectors currently under construction will use optical components on cryogenic temperatures, for example 20 K, to become even more sensitive [4].

To predict the noise level of the interferometer the knowledge of mechanical, electrical and optical properties of the utilised materials is required. A promising candidate material for future gravitational wave detectors is silicon [5]. Many properties of crystalline silicon have already been investigated. One property newly investigated here is the photo-elastic behavior of silicon. The setup for measuring birefringence was developed within a master's thesis [6] and was presented in [7].

By applying mechanical stress or strain to the optically isotropic silicon crystal, it becomes birefringent. This behavior is called photo-elasticity. For not too high stresses, the birefringence Δn depends linearly on the applied strain ε :

$$\Delta n = C \cdot \varepsilon.$$

The proportionality constant C hereby depends on the direction of the applied strain in relation to the orientation of the crystal and on the wavelength of the used light.

If light is passing through the silicon crystal parallel to a $\langle 100 \rangle$ direction and strain is applied perpendicular to this direction but parallel to another $\langle 100 \rangle$ axis, the proportionality constant can be expressed as

$$C = \frac{1}{2} n_0^3 (p_{11} - p_{12}).$$

Similarly, for strain parallel to a $\langle 110 \rangle$ axis it is described by

$$C = \frac{1}{2} n_0^3 p_{44}.$$

Hereby n_0 is the refractive index of silicon without any strain and the p_{ii} are the photo-elastic coefficients.

If the light passes the crystal parallel to a $\langle 111 \rangle$ axis, the photo-elastic behavior stays the same for strain in all directions remains perpendicular to the travelling direction of the light [8]. In this case the proportionality constant is given by

$$C = \frac{1}{6} n_0^3 (p_{11} - p_{12} + 2p_{44}).$$

The setup used to measure birefringence already has been presented in [7]. A schematic of the rotating waveplate polarimeter can be seen in Figure 1.

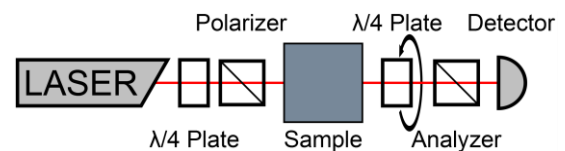


Fig. 1: Schematic of the setup. The polarimeter consists of the rotating quarter wave plate and the polarizer (analyzer) in front of the detector.

To determine the photo-elastic coefficients, small silicon beams with dimensions of about 0.5 mm in thickness and 5 mm in width are being used. Different

weights are clamped on the bottom end of the silicon beams and the upper end is clamped in a fixed position, so the mass of the attached weight is pulling downwards along the beam due to gravitational force. By this method, static mechanical stresses up to about 4 MPa are applied, which results in strains of about 6×10^{-5} . This leads to a measured birefringence in the order of 10^{-5} . The resolution of the setup is able to resolve the birefringence of a sample of at least two orders of magnitude smaller.

In Figure 2 you can see the results for the measurements at room temperature in comparison with other experiments done by Higginbotham [9] and Biegelsen [10], and also with theoretical ab initio calculations done by Levine [11] and Hounscome [12]. The own measurements fit in well with the results of the shown references. Only the values obtained by Higginbotham show larger deviations. However, they also differ significantly from the measurements of Biegelsen and the theoretical calculations by Levine and Hounscome and they lack error bars. Hence it is reasonable to neglect

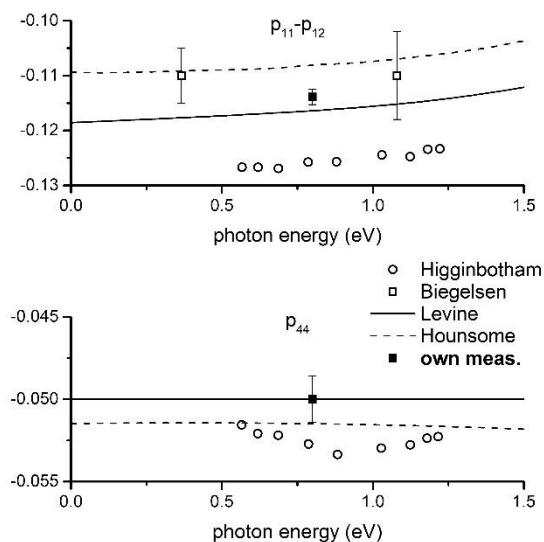


Fig. 2: The measured results fit in well with the related results of the presented references. them.

The thermal behavior of the photo-elastic coefficients is of great interest to study possible polarization effects and novel noise sources at low temperatures. Hence, a setup is built, which allows measurements at low temperature. The sample is placed inside a cryostat and the probing light beam has to cross a window and has to be reflected by two mirrors, to get back to the polarimeter, since the cryostat only has one window. The effects of the window and the mirrors are investigated, such that they can be taken into account for the measurements of the photo-elastic coefficients.

Further measurements will show the temperature dependence of the photo-elastic coefficients and their influence on interferometric gravitational wave detectors.

This work was supported by the Aspera/Appec project "ET R&D" under contract 05A13SJ1.

References

- [1] A. Einstein, Sitzungsber. K. Preuss. Akd. Wiss. 154 (1918).
- [2] B. P. Abbott *et al.*, Phys. Rev. Lett. **116**, 061102 (2016).
- [3] G. M. Harry *et al.*, Classical Quantum Gravity. **27**, 084006 (2010).
- [4] K. Somiya, Classical Quantum Gravity. **29**, 124007 (2012).
- [5] S. Rowan *et al.*, Phys. Lett. A. **347**, 25 (2005).
- [6] R. Glaser, Master Thesis, FSU Jena (2015).
- [7] R. Glaser *et al.*, Annual Report 2014.
- [8] S. He *et al.*, J. Appl. Phys. **96**, 3103 (2004).
- [9] C. W. Higginbotham *et al.*, Phys. Rev. **184**, 821 (1969).
- [10] D. K. Biegelsen, Phys. Rev. B. **12**, 2427 (1975).
- [11] Z. H. Levine *et al.*, Phys. Rev. B. **45**, 4131 (1992).
- [12] L. S. Hounscome *et al.*, Phys. Status Solidi. **203**, 3088 (2006).

Zero-field steps and resonant modes of the long Josephson junction

Alexander Grib¹ and Paul Seidel

¹Physics Department, Kharkiv V. N. Karazin National University, 61022, Kharkiv, Ukraine

Intrinsic Josephson junctions reveal coherent emission at voltages corresponding to frequencies of geometrical resonances of microwaves [1]. Self-resonant steps in IV-characteristics were observed at resonances. In the previous investigations [2] we showed that self-resonant steps appear when the stack of junctions is strongly inhomogeneous, so some junctions radiate inside the transmission line which is formed by the whole system. In the present work on the example of the solitary long Josephson junction we show that self-resonant steps in the IV-curve can appear when resonant modes stipulated by the dimension of this junction are in the range of Josephson generation. We model the long intrinsic junction as a multijunction interferometer. In our model the long junction is divided to n pieces along its length (Fig. 1). In ranges of the capacitively and resistively shunted model, such a system is described by the set of equations for the difference of the phase of the order parameter φ_k which include current conservation conditions together with the flux quantization conditions:

$$\alpha_k \ddot{\varphi}_k + \beta_k \dot{\varphi}_k + I_{ck} \sin \varphi_k = I_b - I_{k-1,k}^R + I_{k,k+1}^R, \quad k=2 \dots n-1, \quad (1a)$$

$$I_{k-1,k}^R L + [\Phi_{k-1,k} + \gamma(\varphi_{k-1} - \varphi_k)], \quad k=2 \dots n, \quad (1b)$$

$$\alpha_1 \ddot{\varphi}_1 + \beta_1 \dot{\varphi}_1 + I_c \sin \varphi_1 = I_b + I_{1,2}^R, \quad (1c)$$

$$\alpha_n \ddot{\varphi}_n + \beta_n \dot{\varphi}_n + I_c \sin \varphi_n = I_b - I_{n-1,n}^R, \quad (1d)$$

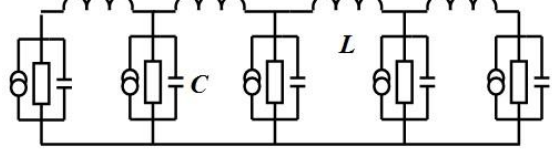


Fig. 1: The scheme of the long junction. Five “elementary Josephson junctions” are shown. In calculations the long junction is divided to 100 “elementary junctions”.

where one and two dots over symbols denote the first and the second derivatives with respect to time, $\alpha_k = \frac{\Phi_0 C_k}{2\pi}$, $\beta_k = \frac{\Phi_0}{2\pi R_k}$, $\gamma = \frac{\Phi_0}{2\pi}$, I_{ck} and R_k are the critical current and the resistance of the “elementary junction”, so the value of

$\frac{1}{n} \sum_{k=1}^n I_{ck} R_k = V_c = const$ for all “elementary junctions”, C_k is the capacitance of the junction, L is the inductance of the “elementary cell” between junctions, $I_{j-1,j}^R$ is the ac current in the loop between two “elementary junctions” with indices $j-1$ and j , I_b is the bias current, Φ_0 is the quantum of magnetic flux. Self-induced resonant steps appear in the IV-characteristics of the system. The average value of C_k is connected with the inductance L by means of the relation $C = \zeta^2 / (\bar{c}^2 L)$ with \bar{c} is the velocity of light in the long junction. With the use of Eqs. (1a)-(1d) we calculated IV-characteristics of the mesa structure of 180 micrometers in length by the method of Runge-Kutta [2]. Critical currents

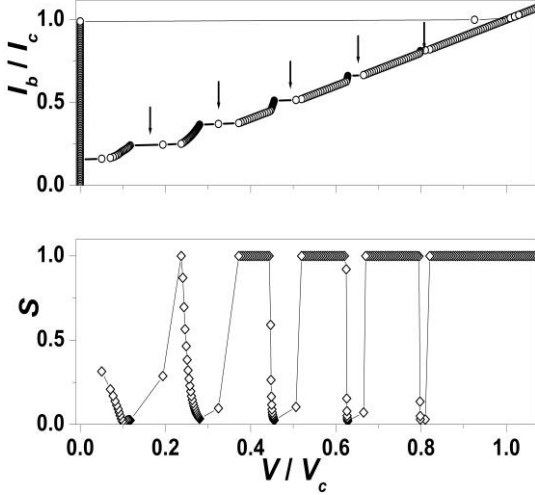


Fig. 2: (a)-the IV-characteristic of the long Josephson junction with the length $D = 180$ micrometers. Arrows mark resonant values of $V_m = 16.3 \cdot m \cdot V_c$; (b)-the dependence of the normalized averaged square of the sum of all ac voltages over “elementary junctions” S on the averaged voltage per junction. Parameters of the system: the Gaussian distribution of critical currents around the averaged value of $I_c = 5.4 \cdot 10^{-4} \text{A}$ with the spread 0.02mA , $n = 100$, $C = 3.96 \cdot 10^{-13} \text{F}$, $L = 1.8 \cdot 10^{-15} \text{H}$, $\bar{c} = 6.7 \cdot 10^7 \text{m/s}$.

of junctions I_{ck} were random values which had the Gaussian distribution with the spread 0.02mA . The IV-characteristic of the system has self-induced steps (Fig. 2). The random superposition of electromagnetic waves in the long junction led to the excitation of resonant modes. There appear zero-field steps in the IV-characteristic of the junction (they marked by arrows in Fig. 2a). Resonance voltages are as follows [3]:

$$V_m = \frac{\Phi_0 \bar{c} m}{D}, \quad m=1,2,3\dots \quad (2)$$

In Fig. 2b we plotted the dependence of the normalized averaged square of the sum of all ac voltages over “elementary junctions” on the averaged voltage per junction $S(V/V_c)$. It is seen that there are deep minima of S in the regions of steps. In these regions standing waves are formed

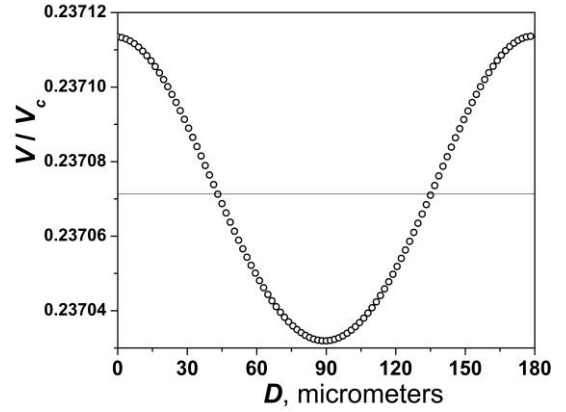


Fig. 3: The distribution of the averaged ac voltage along the transmission line at the bias current $I_b = 0.251 \cdot I_c$. Solid line shows the mean value of voltage.

in the junction. Voltages V_m correspond to even values of Fiske steps [3], so even resonant modes are excited at V_m . The mode which corresponds to the first maximum of the dependence $S(V/V_c)$ at $0.237 \cdot V_c$ is shown in Fig. 3. It is seen that this mode corresponds to two half-waves of voltages along the length of the system.

Thus, in the present work [4] we found the mechanism of the excitation of vibrations of the electromagnetic field in the long junction. This is the locking of random longitudinal vibrations with the resonant mode. This locking leads to the appearance of self-resonant steps in the IV-curve which coincide with even Fiske steps.

References

- [1] M. Tsujimoto *et al.*, Phys. Rev. Applied, 2, 044016, 2014.
- [2] A. Grib and P. Seidel, Low Temp. Phys. (Fiz. Nizk. Temp.) **38**, 321-325 (2012).
- [3] T. A. Fulton and R. C. Dynes, Solid State Commun., vol.12, pp.57-61, 1973.
- [4] Alexander Grib and Paul Seidel, IEEE Explorer, DOI: 10.1109/ISEC.2015.7383434.

Point contact spectroscopy of Co-doped Ba-122 single crystals

Noor Hasan, Sebastian Döring, Stefan Schmidt, Volker Tympel, Frank Schmidl, Thomas Wolf¹ and Paul Seidel

¹ Institute of Solid State Physics, Karlsruhe Institute of Technology, D-76021 Karlsruhe, Germany

Fe-based superconductors (FBS) are a new family of unconventional high temperature superconductors discovered in 2006. They show very interesting properties like high critical currents and magnetic fields. Most important for the still missing understanding in FBS is the pairing symmetry of the order parameter. In order to understand the nature of the superconductivity in iron pnictides; it is necessary to exam and probe their properties, such as energy gap and order parameter symmetry. Point Contact Andreev Reflection spectroscopy (PCARS) is an experimental way to investigate the superconducting gap. Therefore we prepared Niobium (Nb) tunneling point contacts on the optimally doped $\text{Ba}(\text{Fe}_{1-x}\text{Co}_x)_2\text{As}_2$ single crystals ($x \approx 0.06$, $T_c=23.5$ K) which were produced with a self-flux method [1]. The preparation performed by a sharp tip of a Nb electrode pressed along the c-axis of the polished surface of single crystals.

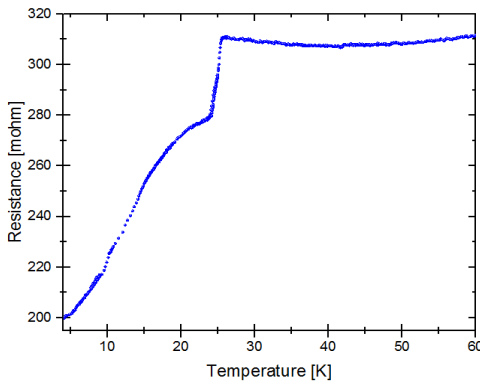


Fig. 1: Resistance obtained from a Co-doped single crystal and Nb electrode.

Fig. 1 shows the temperature dependence of the contact resistance. The curve shows two drops at temperatures of about 23.5 K and ~ 9.2 K which correspond to the T_c of the pnictide single crystal and the Nb tip, respectively. Fig. 1 displays that the $R(T)$ curve is not passing through the origin. That may be the case because of the relatively high carrier transportation rate. In contrast to this case the behavior of junctions showing Josephson effects gives an indication for a critical current and leads to $R(T)$ curves passing through the origin. A typical I-V characteristic given in Fig. 2 shows obviously a nonlinear behavior which is confirmed by measuring the differential resistance (dV/dI) spectra vs. voltage at 4.2 K. On the other hand, the value of the dV/dI spectra at zero voltage is equal to $200 \text{ m}\Omega$ which is the same minimum value of $R(T)$ as in Fig. 1.

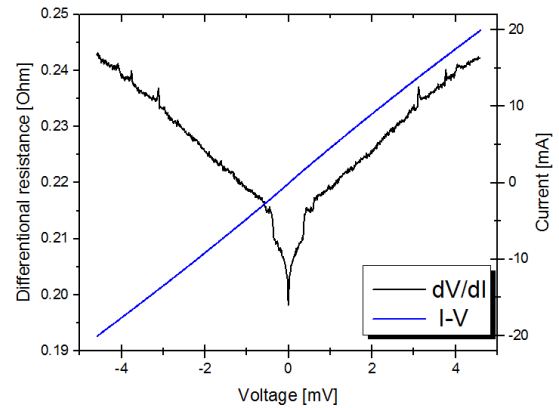


Fig. 2: I-V characteristics and its differential resistance measured at 4.2 K.

[Hier eingeben]

The measured differential resistance spectra at different temperatures in Fig.3 show V-shaped central peaks that may be caused by Andreev reflection. In order to evaluate these data, we used an extended Blonder-Tinkham-Klapwijk BTK model [2]. SN type can be used for Andreev- and tunneling spectroscopy, if it is measured at temperature above the critical temperature of the Nb tip. The observed results show central peaks with multiple features which decreases with the increasing of the temperature and just disappeared above the T_c of the crystal as shown as the green line at $T=26.2$ K in Fig. 3. As well as it shows spread in bias voltage (energy spectra), which may correspond to the broadening parameter Γ [3]. The gap value is determined to be about 3 meV for Ba-122 electrode which is close one value which was observed in [4], where they showed two gap values of $\Delta_1=3.8$ meV and $\Delta_2=8.2$ meV. The spectra also show small peaks in the positive and negative voltage branch in ± 1.5 mV that may be caused by the gap of Nb Δ_{Nb} , which is about 1.5 meV [5].

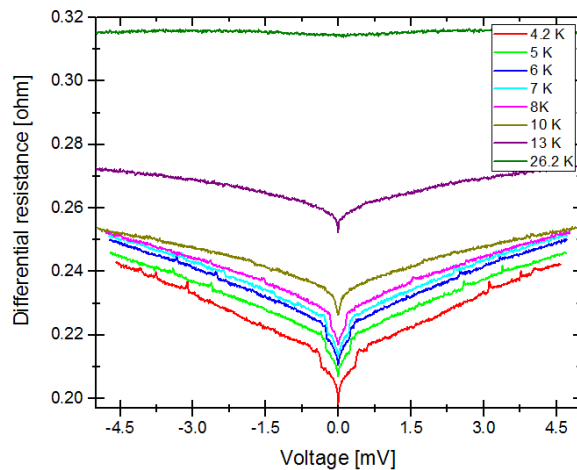


Fig. 3: Differential resistance vs. voltage of contact at different temperatures.

In order to ensure better comparability, the analysis of experimental results leads to a normalized conductivity [6]. Thus the calculated normalized conductance which shows a zero bias conductance peak in the conductance-V characteristics, see Fig. 4.

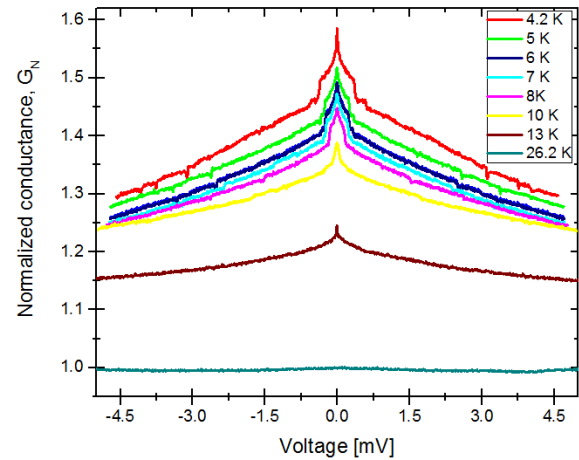


Fig. 4: Normalized conductance of contact at different temperatures.

The advantage of using a Nb tip as counter electrode on the Ba-122 single crystals, we may be able to compare the point contact spectroscopy of single crystals with fabrication planar junctions which have Nb thin film counter electrodes in the near future.

Acknowledgments

We thank the EC (project IRON-SEA), the DFG Se 664/15-2(SPP 1458), and the DAAD for financial support.

References

- [1]F. Hardy *et al.*, *Phys. Rev. B* **81**, 060501 (2010).
- [2]G. E. Blonder *et al.*, *Phys. Rev. B* **25**, 4515 (1982).
- [3]R C Dynes *et al.*, *Phys. Rev. Lett.* **41**, 1509- 1512 (1978).
- [4]M. Tortello *et al.*, *Phys. Rev. Lett.* **105**, 237002 (2010).
- [5]H.-J. Köhler and P. Seidel, *Phys. stat. sol. (b)* **g**, K 51 (1980).
- [6]I. Giaever, *Phys. Rev. Lett.* **5**, (1960).

The Einstein Telescope

Ronny Nawrodt, Rene Glaser, Daniel Heinert, Gerd Hofmann, Julius Komma, Stefanie Kroker¹, Christian Schwarz, and the ET Science Team²

¹Institute of Applied Physics, Albert-Einstein-Straße 15, 07745 Jena

²The full list of the ET Science Team can be found in ref. [3]

Albert Einstein's theory of general relativity predicts the existence of gravitational waves [1]. However, the direct observation of gravitational waves is a very challenging task that calls for extremely sensitive instruments. At last, it was possible to push these instruments to a sensitivity that is sufficient to detect gravitational waves. One century after Einstein's publication a first direct observation of a gravitational wave signal was recently announced from the Advanced LIGO detectors [2] opening a new window to the universe and paving the way for the field of gravitational wave astronomy.

To be capable of performing gravitational wave astronomy detectors with a sensitivity of even ten times better than current instruments are needed. Since constructing such a detector takes about 10-15 years, already now plans for the next generation of gravitational wave detectors are made. The Einstein Telescope is a so

called 3rd generation gravitational wave detector which is intended to provide this enhanced sensitivity requirements (see Fig. 1). This detector is proposed to be a pan-European effort [3]. Its key features to overcome current sensitivity limits are higher laser powers, low noise materials and cryogenic operation as well as better seismic isolation by means of a novel suspension system for the optical components [4].

A central improvement in sensitivity is achieved by using cryogenic temperatures as well as novel, low-mechanical loss materials. The mechanical loss of an optical component is directly linked to the Brownian thermal noise of related device by means of the fluctuation-dissipation-theorem [5, 6]. Thus, minimizing Brownian thermal noise calls for low mechanical losses and low operational temperatures, simultaneously. Fig. 2 gives an overview of the mechanical loss of different optical materials.

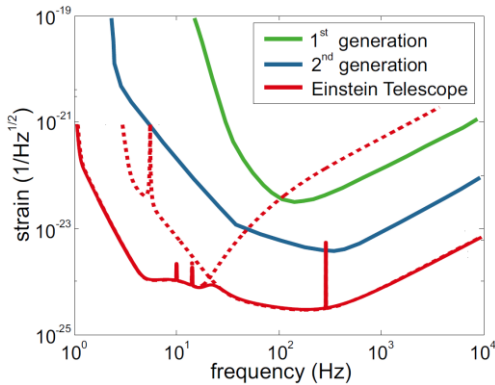


Fig. 1: Comparison of the strain sensitivity of different generations of gravitational wave detectors.

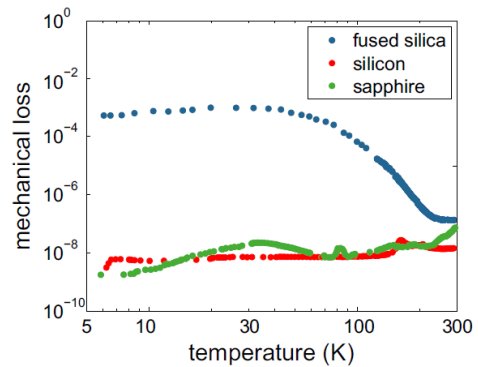


Fig. 2: Mechanical loss of different materials in dependence of the temperature.

Whereas amorphous materials like fused silica – which is currently used in the operating detectors - exhibit a large mechanical loss at cryogenic temperatures crystalline materials like silicon or sapphire have a very small mechanical loss and are thus very well suited for low noise devices.

With the change in optical material several properties and techniques that are important for gravitational wave detectors have to be investigated or even entirely newly developed. Amongst them are mechanical [7], thermal [8] and optical properties [9], as well as jointing techniques [10], polishing, surface state termination [11], and annealing procedures that change the other properties.

All of these parameters and techniques interact with each other. Finding a low thermal noise and highly thermally conductive suspension is for example a non-trivial task. While thermal noise calls for thinner suspension wires thermal conductivity requests the opposite. Delicate measurements are needed to characterize both, test material as well as exact elements for the detectors.

As another example Fig. 3 shows the mechanical loss of silicon between 80 K and 140 K. Before a dedicated heat

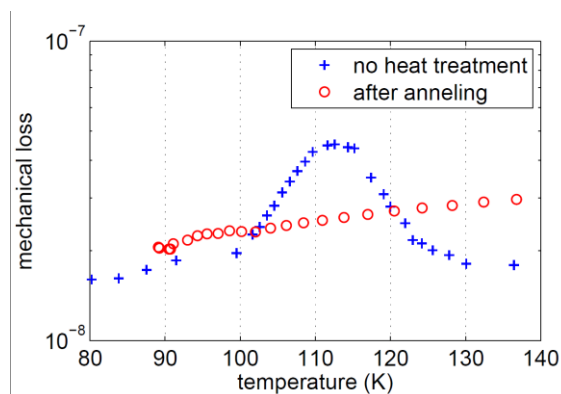


Fig. 3: Mechanical loss a silicon bulk sample before and after annealing.

treatment the silicon sample shows a loss peak that would lead to increased Brownian thermal noise if operated at these temperatures. After annealing the loss peak vanished. The annealing process clusters oxygen that is interstitially located in Czochralski grown silicon samples – as the one used here. Thus, the observed mechanical loss peak is a very sensitive probe for interstitial oxygen in silicon.

Bringing all different results together will lead to a much more sensitive detector for gravitational waves as can be studied in detail in [3].

This work was supported by the DFG under project SFB TR7, the EU within the projects ET (211743) and the ELiTES program (GA 295153) as well as the BMBF under ET R&D (05A13SJ1).

References

- [1] A. Einstein, Sitzungsber. K. Preuss. Akad. Wiss. **1**, 688 (1916) and A. Einstein, Sitzungsber. K. Preuss. Akad. Wiss. **1**, 154 (1918)
- [2] B. P. Abbott et al., Phys. Rev. Lett. **116**, 061102 (2016)
- [3] M. Abernathy et al., „Einstein Gravitational Wave Telescope Conceptual Design Study”, online available at www.et-gw.eu under file ET-0106C-10
- [4] S. Kroker, R. Nawrodt, IEEE Instrumentation & Measurement Magazine **3**, 4 (2015)
- [5] H. B. Callen, R. F. Greene, Phys. Rev. **86**, 702 (1952)
- [6] Yu. Levin, Phys. Rev. D **57**, 659 (1998)
- [7] P. G. Murray et al., Class. Quantum Grav. **32**, 115014 (2015)
- [8] A. Khalaidovski et al., Class. Quantum Grav. **31**, 105004 (2014)
- [9] J. Degallaix et al., Class. Quantum Grav. **31**, 185010 (2014)
- [10] G. Hofmann et al., Class. Quantum Grav. **32**, 245013 (2015)
- [11] R. Nawrodt et al., Class. Quantum Grav. **30**, 115008 (2013)

Cryogenic Current Comparator for Storage Rings and Accelerators

Ralf Neubert¹, Jessica Golm^{1,2}, René Geithner^{2,4}, Volker Tympel¹, Febin Kurian^{3,4}, Thomas Sieber³, Marcus Schwickert³, Paul Seidel¹, and Thomas Stöhlker^{2,3,4}

¹Institut für Festkörperphysik, Friedrich-Schiller-Universität Jena FSU

²Helmholtz-Institut Jena HIJ, ³GSI Helmholtzzentrum für Schwerionenforschung GmbH

⁴Institut für Optik und Quantenelektronik, Friedrich-Schiller-Universität Jena

The First Cryogenic Current Comparator (CCC) for a non-destructive highly sensitive monitoring of nA-beams was developed in the 90s. In recent years this system was optimized for lowest possible noise-limited current resolution in combination with a high system bandwidth of about 200 kHz. This improved CCC consists of commercial state-of-the-art SQUID components, niobium shielding and a toroidal niobium pick-up coil with nanocrystalline NANOPERM[®] core material [1].

The existing CCC has been installed and tested in the Antiproton Decelerator (AD) at CERN in cooperation with GSI, HIJ and FSU Jena, to measure the low-intensity coasting beam. Modifications were required for this implementation in order to adapt the AD beam parameters. The signal slew rate during AD injection exceeds the slew rate of CCC-system because the current suddenly jumps from 0 to $\approx 12 \mu\text{A}$. To solve this problem a low pass filter was inserted between the pick-up coil and the primary coil of the matching transformer. Figure 1 shows the different wiring diagrams and Figure 2 the corresponding noise spectra.

From the first serial setup of resistor and capacitance follows an additional noise contribution around the resonant peak. This is why a parallel connection of resistor and capacitance was chosen for the

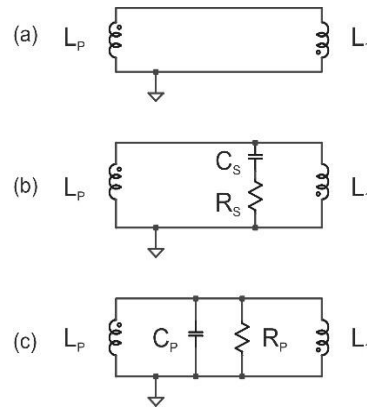


Fig. 1: Connection scheme of the test-ed filter setup in the input circuit between pick-up coil $L_P = 104 \mu\text{H}$ and primary coil $L_1 = 104 \mu\text{H}$ of the matching transformer while the upper scheme is the original one. $C_S = 10 \mu\text{F}$, $R_S = 1 \Omega$, and $C_P = 10 \mu\text{F}$, $R_P = 0.225 \Omega$ at 4.2 K.

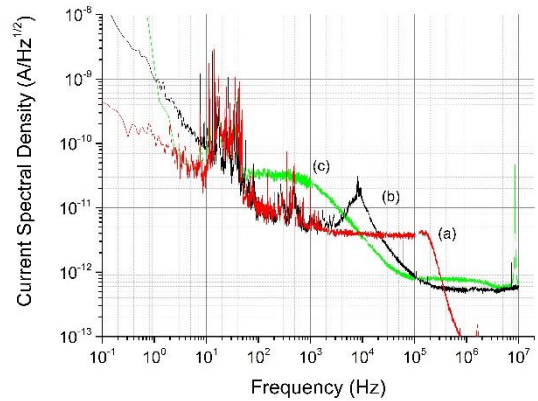


Fig. 2: Current noise of the CCC in the original configuration without filtering in the input circuit (a), with serial connection of R_S and C_S (b), and with parallel connection of R_P and C_P (c) between the pick-up coil $L_P = 104 \mu\text{H}$ and the primary coil $L_1 = 104 \mu\text{H}$ of the matching transformer.

final setup at AD which is more stable but also with an additional noise contribution and a required signal bandwidth of 1000 Hz [2].

The CCC could also be used as an important tool for beam commissioning. Figure 3 shows a beam commissioning cycle measured successfully with the CCC. It is important to find the machine parameters where the particles can travel through the ring without interaction. Particles which hit the wall are lost for the beam. During the measurement shown here the beam got entirely lost during the first cooling plateau (time span $\sim 45 - 80$ s).

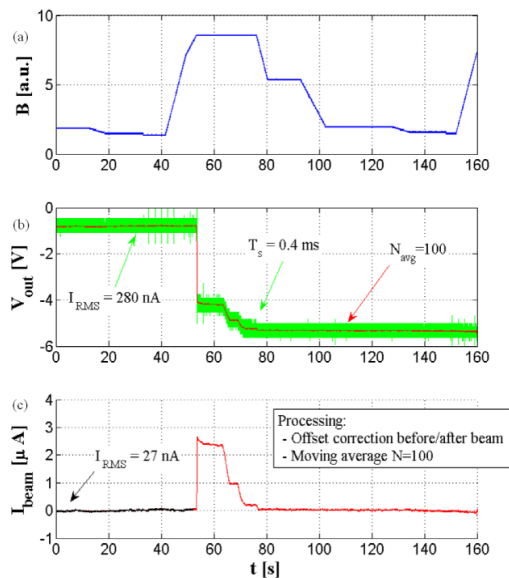


Fig. 3: (a) Magnetic Cycle of AD Di-poles in arbitrary Units. (b) SQUID/FLL raw signal of beam current (in green), and same signal filtered with a moving average (in red). (c) Calibrated beam current measurement after filtering and baseline recovery (before beam injection and after beam extraction) [3].

Within the FAIR project (Facility for Antiproton and Ion Research) an improved SQUID-based CCC is intended to be used as diagnosis device for ion beams. In July 2015 a three-year BMBF joint project (de-

velopment, sensor optimization and test of cryogenic current comparators for use on novel ion sources, accelerator systems and storage rings) with Helmholtz Institute Jena, GSI Darmstadt, Leibniz Institute of Photonic Technology Jena and TU Darmstadt was started.

Furthermore, a one-year project in cooperation with HIJ, CERN and GSI started in January 2016 with the aim to build a new CCC adapted for the requirements in the CRYRING at GSI. This CCC will be used as a test bench for further optimizations of the beam intensity measuring system and new manufacturing technologies and alternative core materials will be studied.

References

- [1] R. Geithner *et al.*, *Phys. Scr.* **T166** 014057, (2015)
- [2] R. Geithner *et al.*, Proc. IBIC 2015, Melbourne, Australia. MOPB013, (2015).
- [3] M. Fernandes *et al.*, Proc. IBIC 2015, Melbourne, Australia. WEPF04, (2015).

Towards a single photon detector in the microwave regime

G. Oelsner¹, E. Il'ichev¹, C.K. Andersen², K. Mølmer², M. Schmelz¹, S. Anders¹, U. Hübner¹,
M. Grajcar³, H.-G. Meyer¹, and P. Seidel

¹Leibniz Institute of Photonic Technology, Jena, Germany

²Department of Physics and Astronomy, Aarhus University, Denmark

³Department of Experimental Physics, Comenius University, Bratislava, Slovakia

In recent years, quantum optic experiments have been repeated in the frame of solid state quantum systems. This involves for example the vacuum Rabi splitting [1] the resonance fluorescence of a single artificial atom [2] as well as single atom lasing [3].

Nevertheless, key devices, namely single photon sources and detectors are missing in the toolbox of superconducting quantum systems. While the creation of single photons inside of cavities was achieved by transferring the excitation from an artificial atom [4], a reliable detection of single photons is still lacking. The low photon energies hinder the use of commercially photomultiplier tubes [5].

We propose the use of an underdamped current biased Josephson junction coupled to a microwave cavity for photon detection. The detection scheme is as follows: The junction is biased close to its critical current value I_c . Then the additional rf-current of a single photon leads to switching of the junction to the stable finite voltage state. This voltage can easily be detected since, depending on the material combination, a value of the order of mV can be achieved.

The current amplitude created by a single photon inside of a cavity may be estimated by [6]

$$I = \sqrt{\frac{h\nu}{L}},$$

where h is the Plank constant, ν the frequency of the microwave radiation and L the inductance of the resonator. We already demonstrated [6] that switching current distribution widths of the order of 2 nA may be achieved. Compared to the current amplitude of tens of nA found for standard $\lambda/4$ resonators, those results promise stable detection conditions.

To test the performance of such device we designed and fabricated a prototype, consisting of two coplanar waveguide resonators each shunted to ground by a Josephson junction. The chip layout is shown in Figure 1.

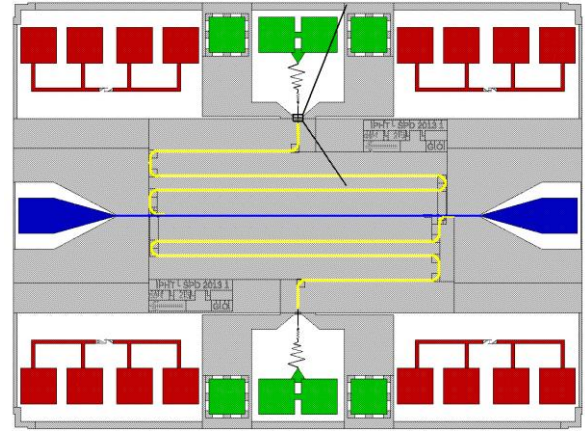


Fig.1: Chip Layout. Two $\lambda/4$ resonators (yellow) are coupled to a microwave transmission line (blue). Josephson junctions (shown in the insert) are coupled in the current antinode of the resonators. A 4-point de-connection (green) ensures current bias and voltage readout. Test junctions with corresponding de-connection (red) are available for pre-characterization.

It is fabricated by the Nb-AlOx-Nb-cross-type technology [7] with an aimed current density of 200 A/cm².

For characterization of one of the devices we measured the transmission through the central microwave line by applying a bias current to one of the junctions. The fitting of the shift of the resonance frequency due to the Josephson inductance [8] allowed the reconstruction of the resonator parameters: resonant frequency $\nu = 2.506$ GHz, quality $Q = 1000$, capacitance $C = 1.6$ pF, and inductance $L = 2.5$ nH. The estimated current amplitude of a single photon for our device thus is 25 nA.

Measuring the temperature dependency of the switching current distribution without microwave in addition gives information about the junction. Thus, the current is

ramped up with a rate of $0.5 \mu\text{A/s}$ and the value at that the finite voltage state is achieved is recorded. Repeating this for at least 1000 times allows to reconstruct the mean switching current I_s and its standard deviation σ . Plotted over the temperature these values follow the same dependency as shown in [6]. The reconstructed values for the junction are the maximal mean switching current $I_s^{\text{max}} = 13 \mu\text{A}$, the minimal $\sigma^{\text{min}} = 40 \text{ nA}$, and the cross over temperature from quantum to thermal activated switching at 200 mK . These values give roughly the same results for the junction parameters as reconstructed from the junction size and geometry: normal resistance $R_J = 140 \text{ W}$ and capacitance $C_J = 400 \text{ fF}$.

Finally, the sensitivity of the device should be estimated. Therefore, we apply a microwave signal with variable frequency and amplitude and measure again switching current distribution. A typical example for an applied power of -110 dBm at the sample input is shown in Figure 2.

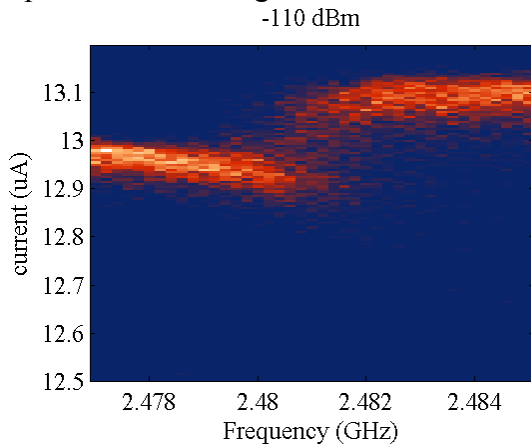


Fig.2: 2D-picture of switching current histograms plotted in y -direction at different driving frequencies. The color scale gives the number of switching events for a certain current and frequency.

A maximal shift of the switching current is achieved for a certain microwave frequency. We denote the minimal mean switching current with I_m . Also a minimum for the distribution width is found at this position (compare also [8]). With reducing power the position of this maximum moves to lower frequency. This is explained by the Josephson inductance, since higher bias currents are needed for lower signal amplitude.

We extracted this maximal shift for different signal amplitudes. Plotted over the driving amplitude (see upper plot in Figure 3) a linear dependence is found. Thus, our device works, as expected, as amplitude detector.

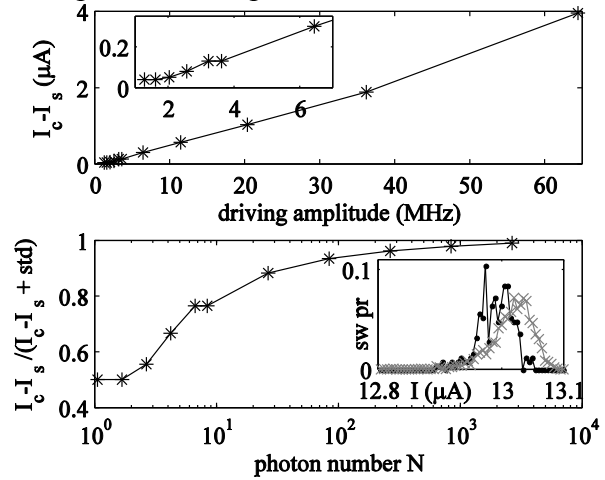


Fig.3: Shift of the histograms in the upper and sensitivity of our device in the lower plot. In addition, the insert in the upper plot is a zoom of the region close to zero and in the lower plot shows the histograms taken for the undisturbed junction (grey) and the lowest applied power (-119 dBm , black)

We define the sensitivity of our device as

$$S = \frac{I_c - I_m}{I_c - I_m + \sigma}$$

and plot it versus the reconstructed photon number in the cavity in the lower plot of Figure 3. The value tends to one for high driving, since there a large separation between histograms with and without driving signal is achieved. For small signals of the order of one photon the maximums of the distributions still are separable and a sensitivity of 0.5 is achieved.

In summary, our fabricated device already works as microwave amplitude detector. The junction parameters should be optimized to values comparable as in [6] for clear separation between switching currents with and without microwave input.

References

- [1] A. Wallraff, et al., Nature **431**, 162 (2004)
- [2] O. Astafiev et.al, Science **327**, 840 (2010)
- [3] O. Astafiev, et al., Nature **449**, 588 (2007)
- [4] A.A. Houck, et.al. Nature **449**, 328 (2007)
- [5] R.H. Hadfield, Nature Photonics **3**, 696 (2009)
- [6] G.Oelsner, et.al., Appl. Phys. Lett. **103**, 142605 (2013)
- [7] S. Anders, et.al. Supercond. Sci. Technol. **22**, 064012 (2009)
- [8] G. Oelsner, et.al. in preparation

Optical absorption of silicon at near infrared and its correlation with electronic properties at cryogenic temperatures

Philip Pastrik, René Glaser and Ronny Nawrodt

The optical properties of silicon have been studied during the last few years. Thus we collected measurements showing the variety of behaviour in case of dropping temperature for silicon with different intensity of doping.

In any case conclusions about the relation between optical and electronic properties were based on inaccurate manufacture specifications. Hence we decided to characterise the samples by their electronic properties with possibilities provided in the institute, so we can investigate the temperature – dependency and link those properties with optical features. This knowledge allows us to word standards of quality required of the silicon to be used in applications like GW – detectors [1].

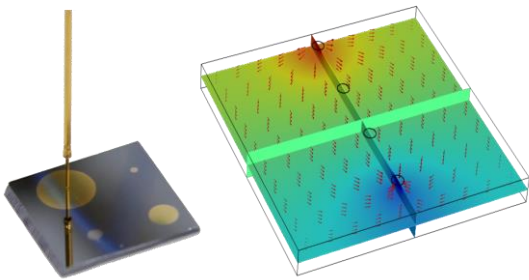


Fig. 1: Illustration of samples. Left, silicon with Schottky – contacts made from gold and contact pin. Right, COMSOL simulation to calculate the conductivity from the measurement of resistance.

Two different processes describe the absorption of light in a solid material; inter- and intraband absorption. Free charge carriers are generated during interband absorption, while already free carriers cause the intraband process.

Therefore the absorption of light in semiconductors is strongly temperature dependent, as the number of free electrons increases as the temperature rises.

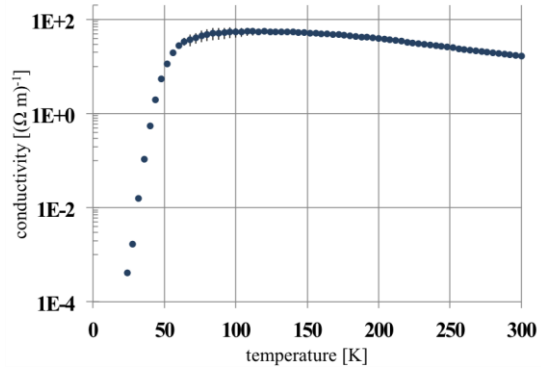


Fig. 2: Determined conductivity of silicon depending on temperature. The conductivity drops dramatically as the density of free carriers decreases at temperatures below 100K after mobility increases during cooling.

To study the electronic properties of silicon, a measurement setup was needed that would fit in our cryostat. Both, the density and the mobility of carriers determine the absorption by free carriers, such as it is necessary to know density and lifetime to interpret absorption by interband processes. The combination of measurements with a 4 – wire setup to determine the conductivity and a Capacity – Voltage (CV) measurement on a Schottky – contact to measure the density of carriers enable the calculation of absorption by free carriers, as Ohm’s law provides the mobility. The observation of conductivity is also a possibility to recognise an abrupt change of carrier density caused by irradiation.

Two types of electronic contact were necessary. Aluminium was used as ohmic

contact since other materials as indium and lead failed to show reliable properties. To obtain a Schottky – contact, gold was sputtered on the surface of the silicon after it has been cleaned with HF.

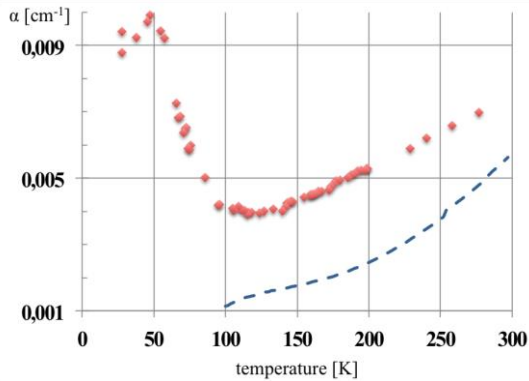


Fig. 3: Red dots, measured absorption of silicon sample. Blue dashed line, absorption of same silicon calculated from density of free charge carriers and mobility of carriers.

To make a bonding even possible, the gold structure was treated by heat, so a gold wire could get fixed onto the surface. For best ohmic behaviour, the aluminium contacts were not treated after the evaporation, yet the surface of the silicon had to be cleaned from oxide.

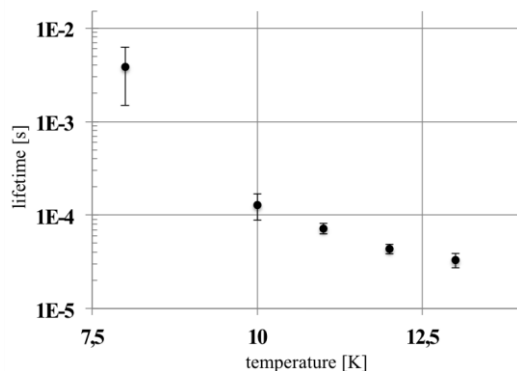


Fig. 4: Lifetime of excited states depending on temperature. The higher values at lower temperatures could be caused by the absence of scattering centres.

It was possible to use the prepared samples to measure their conductivity at cryogen temperatures at 8 Kelvin up to 300 Kelvin within the same continuous – flow

cryostat (cooled by LHe). As shown in Fig.2 in a first step the conductivity increase as temperature drops due to the increase of mobility. At temperatures below 100 Kelvin, the charge carriers return to their ground – states, as expected, so the resistivity increase dramatically by orders of magnitude until it reaches too high values to ignore the internal resistance of the source-measurement unit (SMU).

In Fig.3 the measured absorption at 1550 nm and the absorption calculated for the determined density of carriers for the same phosphorus – doped silicon – wafer with 1 to 5 Ωcm is shown. The deviation could be caused by a bias in the CV – measurement.

The absorption starts to rise again as soon as the interband process occurs due to the growing number of electrons in ground state (see Fig.3). Once there is no excited state anymore, the absorption reaches saturation level. Below 40 Kelvin free electrons are generated by absorption of radiation only. To calculate the absorption caused by interband absorption and absorption by free carriers generated by interband process at low temperature, the lifetime of excited states is necessary. Therefore a pulsed laser irradiated the silicon. A change of conductivity was detected and it was possible to measure the time it takes for an excited state to relax (see Fig.4).

The increase of lifetime could be the reason for the fall of absorption at temperatures below the range of saturation [2]. In a further step, it will be possible to study the link between absorption, lifetime and impurity density at low temperature.

References

- [1] <https://tds.ego-gw.it/ql/?c=7954>
- [2] P. Pastrik *et al.*, Annual Report 2014.

Examination of bicrystal grain boundary junctions of $\text{BaFe}_2(\text{As,P})_2$ pnictide superconductors

Stefan Schmidt, Takahiko Kawaguchi¹, Sebastian Döring, Frank Schmidl, Volker Tympel, Fritz Kurth², Hiroshi Ikuta¹, and Paul Seidel

¹ Department of Crystalline Materials Science, Nagoya University, Japan

² Institute for Metallic Materials, IFW Dresden, Germany

Superconductors can be utilized in a wide range of applications. In polycrystalline or textured cables and magnets one tries to maximize the superconducting current. Natural grain boundaries limit the current as they decrease the critical current, J_C , of their interfaces with increasing mismatch angle. In the case of the widely used YBCO, the steep decrease occurs at very low angles and continues to drop exponentially, see Fig.1.

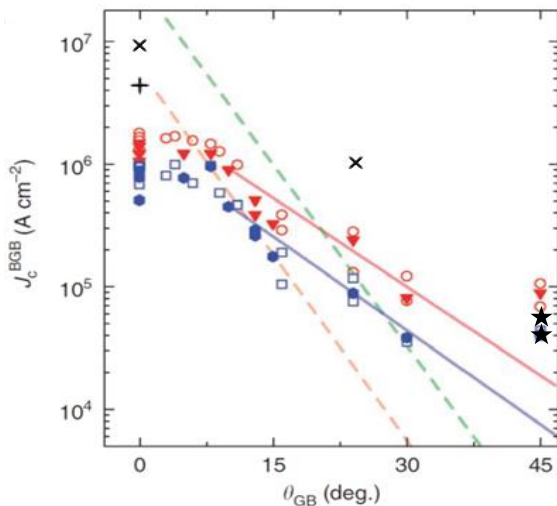


Fig. 1: Critical current density vs grain boundary angle [1]. The black x and + mark results from P-doped Ba-122 samples deposited by MBE [2] and PLD [3], respectively. The stars denote the results mentioned in the present article.

In 2008, a new class of superconductors with a high critical temperature was discovered. First investigations suggested, that at least some of those pnictides develop an exponential decrease with a more gradual slope. In Figure 1 this decline is visible thanks to the logarithmic scale of J_C . The red and blue symbols correspond to temperatures of 4 K and 12 K, respectively.

Even more promising properties have been found in P-doped Ba-122 compounds. In contrast to the well-examined Co-doped Ba-122 the isovalent substitution of Arsenic with Phosphorous implies pure structural deformation to be the cause for a superconducting transition. First grain boundary measurements suggest a J_C decline with a slope as gradual as for the Co-doped pnictide, but with an even higher initial value of around 10^7 A/cm².

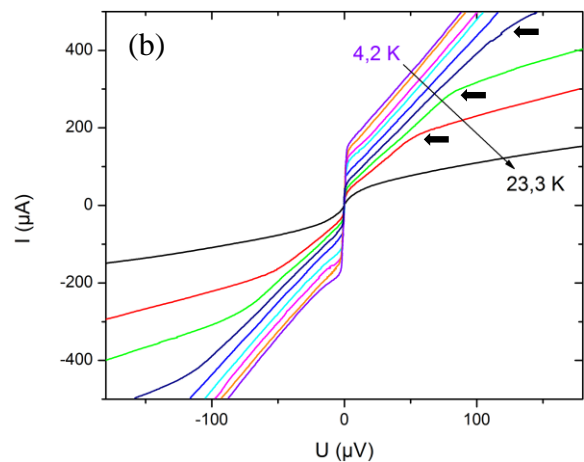
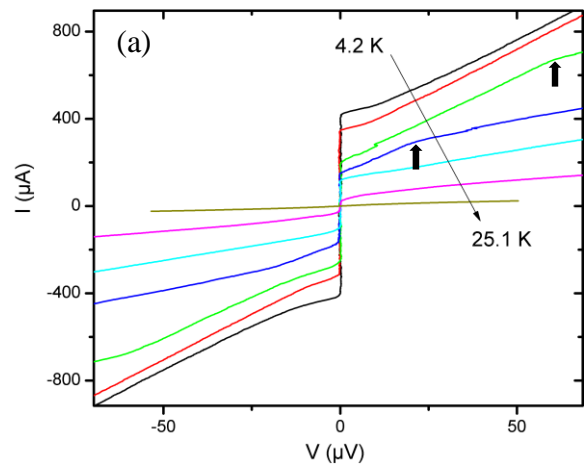


Fig. 2: I-V characteristics of a 45° grain boundary junction at different temperatures. (a) microbridge width = 10 μm . (b) bridge width = 7 μm .

We prepared P-doped Ba-122 grain boundary junctions based on thin films that have been deposited similarly to the samples in [2]. As substrate material we chose LSAT due to the improved superconducting properties compared to MgO substrates. Using ion beam etching narrow bridges with different widths have been structured to investigate the properties of the grain boundary, systematically [4]. The I-V characteristics show RSJ-like behavior with a considerably high excess current, see Fig. 2. When looking at the slope at higher voltages one can see a “second knee” at a number of curves, marked by fat arrows. In the top picture, Fig. 2 (a), the given curves are colored green (11.5 K) and dark blue (14.4 K).

In Fig. 2 (b) the curves at temperatures of 16.6 K, 18.4 K, and 20.2 K show a similar behavior. This peculiarity leads to two different values of the normal state resistance. Whereas the curves at temperatures below 16 K bottom exhibit a $R_{N,1}$ of about 0.25Ω the characteristic at 23.3 K has a slope that corresponds to $R_{N,2} = 1 \Omega$. This behaviour can be explained with the presence of more than one Josephson junction. If the critical current of the first junction is exceeded it switches to its resistive state with $R_{N,1}$. At this point the second junction remains Josephson-like until its critical current is reached as well. The temperature dependencies of both current values are depicted in Fig. 3 for both bridge widths. The “second knee” could not be investigated at lower temperatures due to the high currents that would have been needed – a similar microbridge was destroyed at currents around 1 mA. The temperature dependence of both I_c and the additional knee of the grain boundary junction with a bridge width of $10 \mu\text{m}$ is shown in Fig. 3 (a). At around 16 K both

current values cannot be distinguished anymore.

In Fig. 3 (b) the “second knee” seems to close at a higher temperature than the critical current itself. Future investigations will clarify the origin of this feature even more.

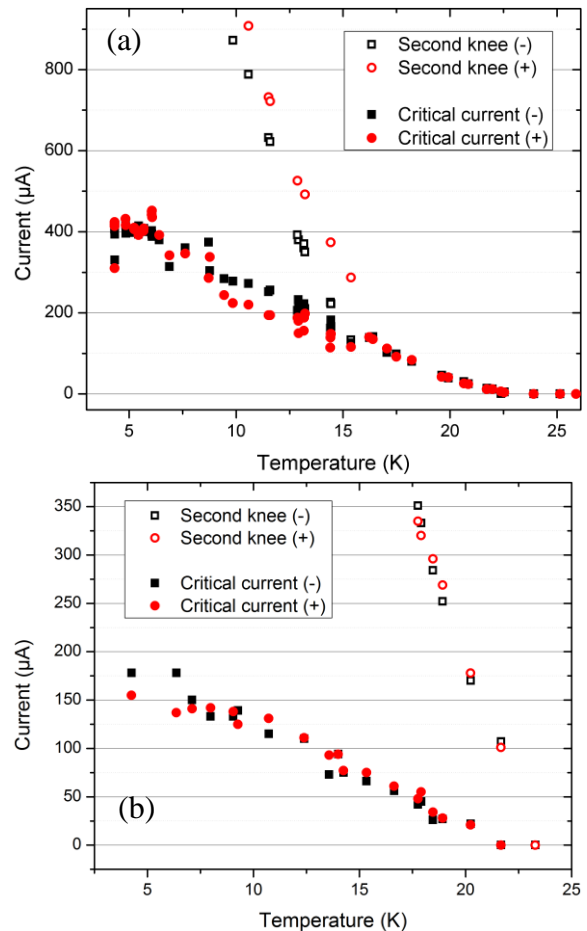


Fig. 3: (a) and (b) Temperature dependencies of the critical current and the second knee in the I-V characteristics shown in Fig. 2 (a) and (b). The brackets in the legend panel indicate the current branch this value belongs to, (-) being the negative current branch and (+) the positive one.

References

- [1] T. Katase *et al.*, *Nat. Comm.* **2**, 409 (2011).
- [2] A. Sakagami *et al.*, *Physica C* **494**, 181-184 (2013).
- [3] P S. Adachi *et al.*, *Supercond. Sci. Technol.* **25**, 105015 (2012).
- [4] S. Schmidt *et al.*, *J. Phys. Conf. Series* **507**, 012046 (2014)

A portable three-axis SQUID-based absolute vector magnetometer

T. Schönau^{1,2}, M. Schmelz², V. Zakosarenko³, R. Stolz², M. Meyer³, S. Anders², S. Linzen²
and H.-G. Meyer²

¹Friedrich-Schiller-University Jena, Institut für Festkörperphysik, Helmholtzweg 5, D-07743 Jena, Germany

²Leibniz Institute of Photonic Technology, PO Box 100239, D-07702 Jena, Germany

³Supracon AG, An der Lehmgrube 11, D-07751 Jena, Germany

The highly sensitive mapping of large areas of the Earth's magnetic field is relevant for many applications, like e.g. mineral and oil exploration, unexploded ordnance detection, archaeology and many others.

The obtained data quality is mainly limited by the noise level and bandwidth of the used sensors. In this respect, SQUIDs offer huge advantages compared to established sensors like fluxgates or scalar cesium vapor magnetometers. But, due to their periodic voltage-flux characteristics and the necessity to operate SQUIDs in a flux-locked loop (FLL), their output is ambiguous and limited in its dynamic range. For this reason, only SQUIDs designed as gradiometers have so far found their way to the applications mentioned above. But gradiometers significantly differ from magnetometers with respect to many relevant properties. For example, they are less appropriate to detect magnetic anomalies at great distances. The presented SQUID-based absolute vector magnetometer with enhanced dynamic range is therefore the first approach allowing an equivalent replacement of the established magnetometers in combination with an increase in sensitivity.

In order to overcome the earlier mentioned limitations of SQUIDs, we introduced the so called cascade principle, consisting of a set of coplanar SQUID magnetometers with effective areas that successively differ by about two orders of magnitude. Each SQUID is operated by its own directly

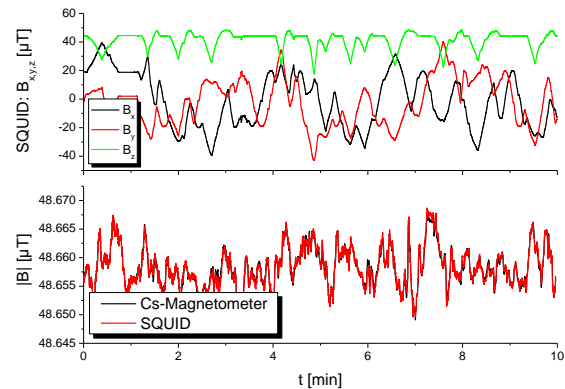


Fig. 1: In order to evaluate its absolute accuracy, the vector magnetometer was tilted and rotated in the homogeneous magnetic field of the Earth. The calculated absolute value $|B|$ coincides well with the output of a scalar cesium magnetometer, which was used as reference.

coupled FLL electronics with integrated auto-reset option. Due to the combined read out of all SQUIDs in the cascade, the ambiguity of a single SQUID can be circumvented and a definite relationship between the magnetic field component perpendicular to the chip and the output can be guaranteed for a much wider range of magnetic field strengths [1,2].

Based on this principle, we implemented a three-axis vector magnetometer with a white noise level of about $10 \text{ fT/Hz}^{1/2}$, suited for mobile operation in the Earth's magnetic field [3].

Beside sensitivity, the accuracy of the vector magnetometer is in particular relevant for potential applications. Several measurement procedures have been developed, allowing a precise and partially automated determination of relevant

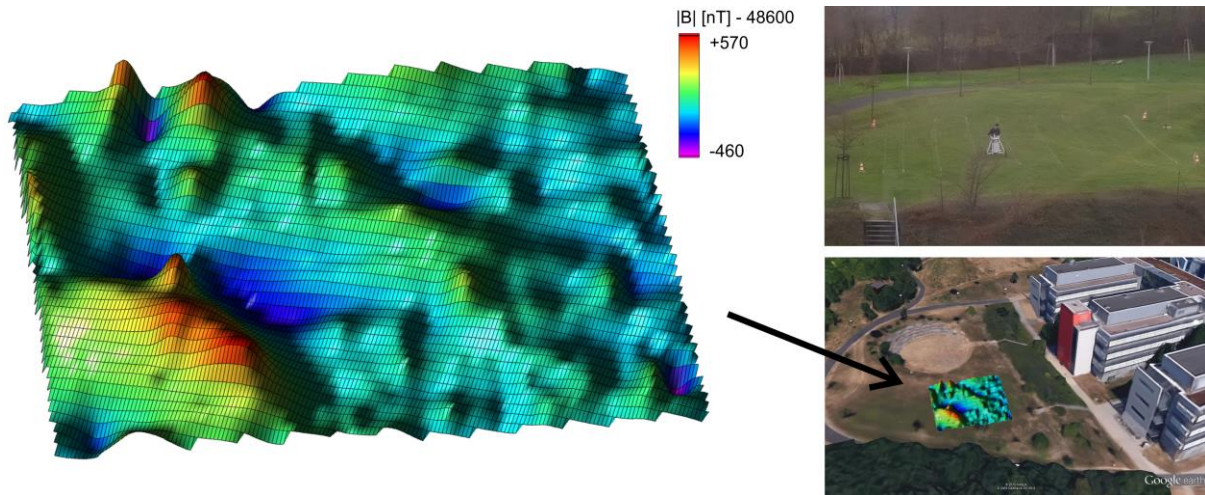


Fig. 2: First test of the setup outside laboratory environment. An area of $15 \times 15 \text{ m}^2$ near IPHT was mapped with a line spacing of 1 m.

parameters like the output voltage per flux quantum for each FLL-channel, crosstalk between channels and the vector of each SQUID's effective area.

As final calibration step, the output signals (B_x , B_y , B_z) must be corrected by an offset vector as well as six scalar values that characterize deviations from a perfect orthonormal 3-axis vector magnetometer. These parameters are determined by tilting and rotating the setup in the homogenous magnetic field of the Earth, as described in [4]. Afterwards, the absolute value $|B|$ calculated from the vector components is rotational invariant as shown in Fig. 1 and coincides with the output signal of a cesium vapor magnetometer.

For a first field test, the setup was mounted on a special non-magnetic trolley and the magnetic field vector was repeatedly mapped within an area of $15 \times 15 \text{ m}^2$. During the measurements, all sensors performed as expected and demonstrated the applicability of the setup. For each iteration, a map of $|B|$, like the one shown in Fig. 2, was calculated. By comparing these maps, we found that deviations could mainly be attributed to the limited spatial resolution of the measurement, which can

in future be overcome by the use of differential GPS.

The author likes to thank his supervisor Prof. Paul Seidel.

References

- [1] T. Schönau, M. Schmelz, V. Zakosarenko, R. Stolz, M. Meyer, S. Anders, L. Fritsch and H.-G. Meyer, *Supercond. Sci. Technol.* **26** 035013 (2013).
- [2] V. Zakosarenko, T. Schönau, R. Stolz and H.-G. Meyer, *Patent DE 1020130* (2014).
- [3] T. Schönau, V. Zakosarenko, M. Schmelz, R. Stolz, S. Anders, S. Linzen, M. Meyer and H.-G. Meyer, *Rev. Sci. Instrum.* **86** 105002 (2015).
- [4] H.-U. Auster, K.H. Fornacon, E. Georgescu, K.H. Glassmeier and U. Motschmann *Meas. Sci. Technol.* **13** 1124 31 (2002).

Effects of LC shunting on the Shapiro steps features of a Josephson junction

Yu. M. Shukrinov ^{a,b}, I. R. Rahmonov ^{a,d}, K. V. Kulikov ^{a,b}, P. Seidel ^c

^a*BLTP, Joint Institute for Nuclear Research, Dubna, Moscow Region, 141980, Russia*

^b*Dep. of Theoretical Physics, International University of Dubna, Dubna, 141980, Russia*

^c*Institut für Festkörperphysik, Jena, D-07743 Jena, Germany*

^d*Umarov Physical Technical Institute, TAS, Dushanbe, 734063 Tajikistan*

An important point for different applications of Josephson junctions (JJs) is a possibility to manipulate and control their parameters and characteristics. One of the effective methods for affecting the JJ is its shunting by LCR (L: inductance; C: capacitance; R: resistance) elements [1–5]. In particular, shunting leads to the synchronization of oscillations of the superconducting current in an array of JJs. JJs, together with the LCR elements, form an oscillatory circuit.

An interesting problem concerns the effect of external electromagnetic radiation. The properties of SS in the case of shunted JJ are not investigated yet. Up to now there is no detailed study of SS on a resonance branch. Particularly, the amplitude dependence of the width of SS on the resonance branch has not been considered till now.

In Ref.[6], we demonstrate an effective way to manipulate and control the features of JJs and investigate the influence of the external electromagnetic radiation on the dynamics and IV-characteristics of JJs shunted by LC elements. The properties of SS on the resonance branch offer promising applications.

The scheme of JJ with the LC shunting elements is represented in fig. 1. To describe the properties of this system, we use the usual RCSJ model which captures

its main features. In the normalized units the system of equations describing this electric scheme can be written in the form

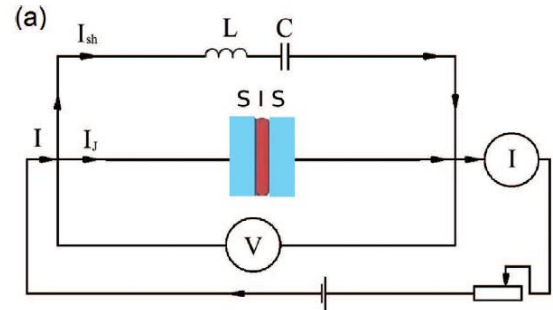


Fig. 1: Schema of the JJ with LC shunting elements

$$\begin{cases} \frac{\partial \varphi}{\partial t} = V \\ \frac{\partial V}{\partial t} = I - \sin \varphi - \beta \frac{\partial \varphi}{\partial t} - C \frac{\partial u_c}{\partial t} + A \sin \omega t \\ \frac{\partial^2 u_c}{\partial t^2} = \frac{1}{LC} (V - u_c) \end{cases} \quad (1)$$

Here u_c is the voltage at the capacitance. The bias current I is normalized to the critical current I_c of JJ, time - to the inverse plasma frequency $\omega_p = \sqrt{2eI_c / \hbar C}$, voltages V and u_c normalized to $V_0 = \hbar \omega_p / 2e$; shunt capacitance C - to the capacitance of the JJ C_j , and shunt inductance L - to $(C_j \omega_p^2)^{-1}$. In the system of equations (1) we introduce a dissipation parameter

$\beta = (1/R_j)\sqrt{\hbar/2eI_cC_j} = 1/\sqrt{\beta_c}$ with β_c as McCumber parameter. Amplitude A and frequency of external radiation ω normalized respectively to the critical current I_c and plasma frequency ω_p .

Figure 2(a) represents the IV-characteristic obtained at amplitude $A = 0.6$ and the frequency $\omega_R=3$ equal to the eigenfrequency of the resonance circuit, i.e. at the resonance condition $\omega_R = \omega_J = \omega_{rc}$. The first SS in this case is on the top of the resonance branch. In the inset to fig. 2(a) we enlarge this part of the IV-characteristic to demonstrate clearly the step at $V = 3$. We note that on the IV-characteristic appear other steps, which are not observed without shunting. We see that these steps show (figs. 2(b)–(d)) a zero slope, so we consider them to be harmonics and subharmonics of the Shapiro step. The dependence of the SS width on A at frequency $\omega_R = 3$ for shunted JJ with note SS-rc is represented in fig. 2(e). The dots are numerical results and squares are their fitting. Here we show also the simulation results (dots) and theoretical (squares) for the case without shunting (SS) at the same frequency $\omega_R=3$.

We show that the amplitude dependence of the Shapiro step width crucially changes when the Shapiro step is on the resonant circuit branch. These effects might give very important advantages for methods and

technologies that exploit the response of Josephson junctions to microwave fields.

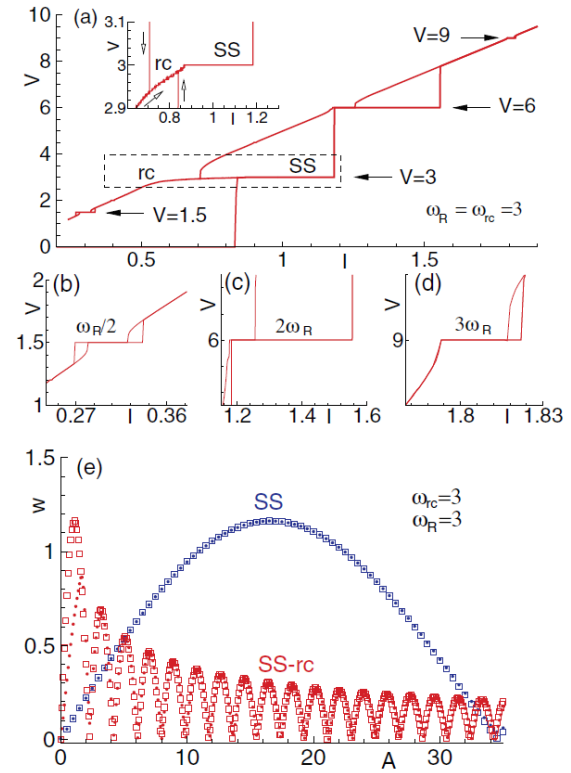


Fig. 2: (a) IV-characteristic of the shunted JJ under radiation. The arrows indicate the branch at the resonance $\omega_R = \omega_{rc} = 3$, harmonics at $V = 6$, $V = 9$ and subharmonic at $V = 1.5$. The inset (b), (c) and (d) show the enlarged harmonics and subharmonic (1/2) indicated in (a). (e) The amplitude dependence of the width w of SS on the resonance branch (SS-rc) at $\omega_R = 3$, compared to the dependence without shunting (SS) [6].

References

- [1] Hadley P. and Beasley M. R., Appl. Phys. Lett., 50 (1987) 621.
- [2] Wiesenfeld K., Colet P. and Strogatz S. H., Phys. Rev. Lett., 76 (1996) 404.
- [3] Filatrella G., Pedersen N. F. and Wiesenfeld K., Phys. Rev. E, 61 (2000) 2513.
- [4] Grib A. N., Seidel P. and Scherbel J., Phys. Rev. B, 65 (2002) 094508.
- [5] Fistul M. V., Phys. Rev. B, 75 (2007) 014502.
- [6] Yu. M. Shukrinov, I. R. Rahmonov, K. Kulikov. and P. Seidel, EPL 110, 47001, (2015)

Multi-resonance frequencies matching – Measurement of very small inductivities

Volker Tympel, Ralf Neubert, Jessica Golm, René Geithner

Sometimes it is necessary to measure very low inductivities in the nano-Henry-range. Of course there are precision-LCR-meters available like the E4980A from Agilent with a wide frequency range from 20 Hz to 2 MHz and a 4-digit resolution [1]. Small inductivities can be measured with short cables easily [Fig. 1], but we will have problems with larger cables which cannot be compensated by 4-wire-technique or short-circle compensation. Long cables are typical for cryogenic measurement setups.

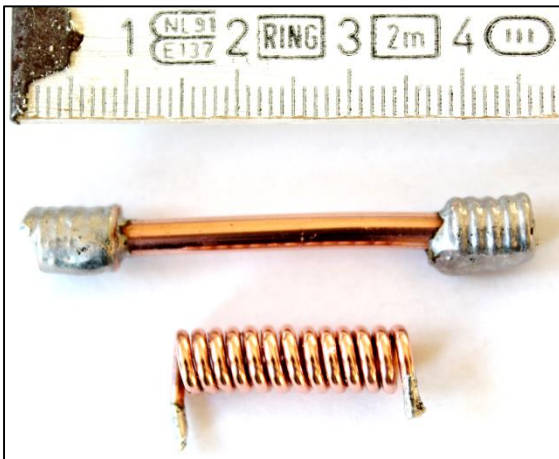


Fig. 1: Copper test inductivities, top: 5 nH / 270 $\mu\Omega$, bottom: 120 nH / 8.8 m Ω @ 100 kHz.

A coreless single turn pick-up Pb-coil for a cryogenic current comparator (CCC) as shown in Fig. 2 should have a very small inductivity of a few nH. To verify the measurements done with a precision LCR-meter on different frequencies is a second, complete different method necessary to understand the influence of the cables and the contact pads. Fig. 3 shows an inductivity of 22 nH below 10⁶ Hz and ca. 17 nH above and a very low resistance below 35 m Ω measured with an E4980A and four short bunched Cu-wires (20 cm, 2.5 mm²).

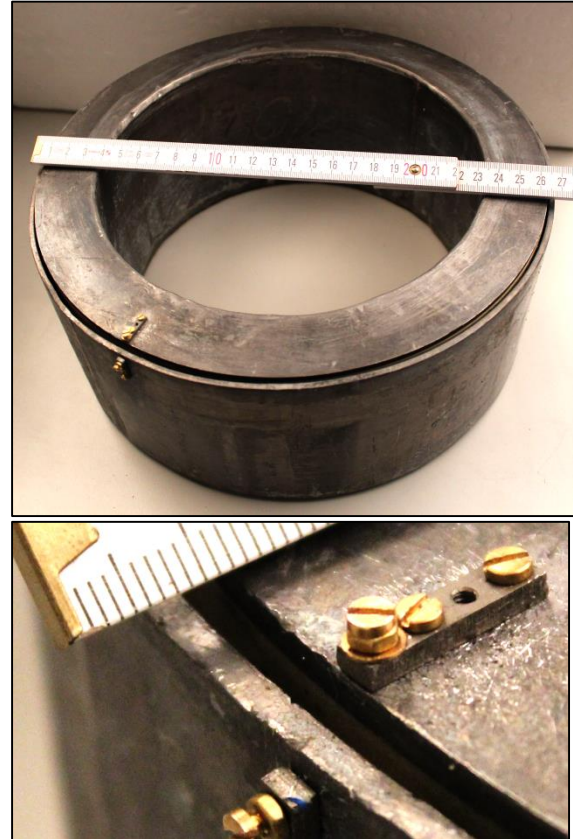


Fig. 2: Coreless single turn pick-up coil made of lead with niobium contact pads (bottom).

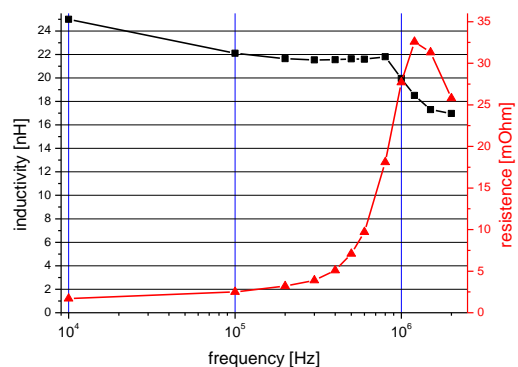


Fig. 3: Inductivity and resistance of the pick-up coil vs. frequency measured with E4980A and very short Cu-wires at room temperature.

Assuming a constant inductivity L_0 and a parasitic capacity C_0 of the coreless coil and a low resistance we can measure the

first resonance frequency f_0 with a programmable synthesizer HM8134, a fast oscilloscope and cable-decoupling via the resistances R_2 and R_3 [Fig. 4].

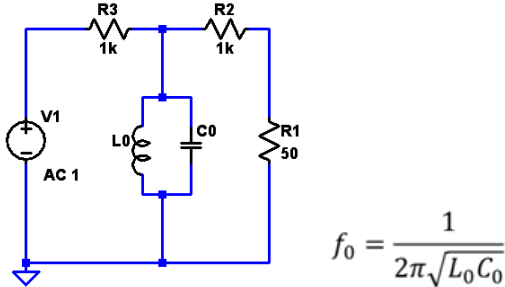


Fig. 4: Measurement of the resonance frequency of L_0C_0 -resonator.

Two additional capacities with low parasitic inductivities [Fig. 5] open the way to measure four new resonance frequencies as shown in Fig. 6.

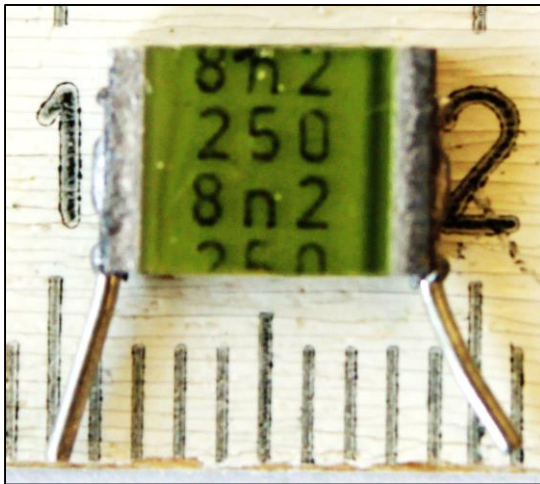


Fig. 5: Nominal 8.2 nF capacity with short wires and suitable for cryogenic applications.

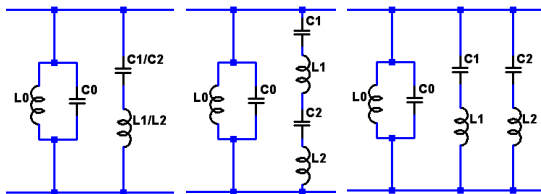


Fig. 6: Left: L_0C_1 -/ L_0C_2 -resonator, middle: L_0C_S -resonator, right: L_0C_P -resonator.

At the end we have five measured frequencies and five unknown parameters: the searched coil inductivity L_0 , the coil capac-

ity C_0 , the used additional capacities C_1 and C_2 and their inductivities assuming $L_1 = L_2$. Now we can use a C++ written software to vary all five parameter in five loops, calculating always the five resonance frequencies and find the best match according the measured frequencies. Tab. 1 shows the results for the single-turn Pb-coil with a mean error of the frequencies of 2 % and a mismatch of only 1.5 nH between the LCR-meter and the multi resonance frequencies matching method.

Best matching		$L_0 = 18.5 \text{ nH}$	
$C_1 =$ 8.18 nF	$C_2 =$ 7.89 nF	$C_0 =$ 225 pF	$L_1 = L_2 =$ 5.28 nF
Fre- quency	comment	measured MHz	calculated MHz
f_0	C_0 coil only	78.0	77.99
f_1	+ C_1	11.5	11.26
f_2	+ C_2	11.7	11.45
f_S	C_1, C_2 serial	14.1	14.33
f_P	C_1, C_2 parallel	8.37	8.573

Tab. 1: Matching results and comparison between measured and calculated frequencies.

The described method opens a way to measure very low inductivities over long connection cables in cryogenic applications. The control of measuring equipment can easy be realized by a Rubidium frequency standard as described last year in [2]. However, it is necessary for the multi-resonance frequencies matching that parameters within range of the resonance frequencies are frequency-independent.

References

- [1] Agilent Technologies, E4980A Precision LCR Meter User's Guide, Dec. 2002.
- [2] V. Tympel, ISO 9001 Quality management of measuring equipment – First step: Time und frequencies. 120-121, Annual Report 2014, download 2015-12-20: http://www.ifk.uni-jena.de/ifk_multimedia/Jahresberichte/Jahresbericht+2014.pdf.

Inner-gap structure in differential-conductance spectra of superconducting junctions with degraded interfaces

Elena Zhitlukhina¹, Mikhail Belogolovskii², Igor Devyatov³, Oleg Egorov, and Paul Seidel

¹ *Donetsk Institute for Physics and Engineering, 03680, Kyiv, Ukraine*

² *Institute for Metal Physics, 03680, Kyiv, Ukraine*

³ *Lomonosov Moscow State University, Skobeltsyn Institute of Nuclear Physics, 119991 Moscow, Russia*

This work was aimed to explain some unexpected features in transport characteristics of superconducting junctions which look very unusual from the viewpoint of the conventional theory. The first feature of such kind known as a ‘knee’ was revealed in 70s for tunneling S-I-S Nb-based trilayers at voltage biases slightly above the twice gap value [1]. The next puzzling feature was the so-called ‘peak-dip-hump’ structure observed in conductance-vs-voltage curves for high- T_c -superconductor break-junctions [2]. In these experiments the peak was attributed to twice the gap magnitude although the values obtained were systematically lower than those found in other experiments. But the main problem of the measurements was the presence of a pronounced dip revealed also by other techniques like STM or ARPES. The last unusual feature which is analyzed below relates the inner-gap structure in S-c-S junctions (c stands for a constriction with a transmission probability near unity). Related experiments detected a fine structure due to multiple Andreev reflections within the constriction between the two superconductors. According to the theory, the conductance peaks positions are $V_n = 2\Delta_s / (en)$, Δ_s is the s -wave symmetrical order parameter, n is an integer. But, in contrast to the expectations, this relation did not set the positions of peaks but rather those of dips [3]. We explain the origin of the discrepancy relating it to the degradation of S-c and c-S interfaces which is modeled by inserting clean non-superconducting (n) interlayer of the thickness d_n between I and S films. Confinement of electrons in the n-metal film results in discrete quantum-well states that can be

probed directly by single-electron tunneling spectroscopy.

We propose an intuitive geometric picture for the bound states with energies $\varepsilon = E - E_F$ (E_F is the Fermi energy) based on the quantization condition, which requires an integer number of 2π phase accumulation along an enclosed ‘round trip’ of an electron. The latter one includes backscattering from the insulating layer which gives a phase shift of π , Andreev electron-to-hole and hole-to-electron reflections from the n/S interface, and phase shifts accumulated by quasiparticles during the paths from one boundary to another. The relation for the lowest bound level reads as $\bar{\varepsilon} = (\hbar v_F / 2d_n) \arccos(\bar{\varepsilon} / \Delta) \cos \theta$, here $d_n \neq 0$, θ is the incident angle. For vanishing d_n , we get $\bar{\varepsilon} = \Delta$. When the thickness d_n is finite, $\bar{\varepsilon} < \Delta$ and the effect is controlled by the parameter $\alpha = 2d_n \Delta_s / (\hbar v_F) = d_n / \xi_n$, where the length scale governing superconducting correlations in a clean n-metal is $\xi_n \approx E_F / (k_F \Delta_s)$, v_F and k_F are its Fermi velocity and wave vector. In traditional metals, due to comparatively large v_F and small Δ_s $\xi_n \geq 100$ nm and, thus, the effect of the n-interlayer can be observed merely at d_n of the order of tens nanometers. Such interlayers can be introduced only artificially within the junction, see, for example, [4,5]. If, however, the Fermi velocity is small and at the same time the energy gap is large, as it is in Nb and novel high- T_c compounds, a completely different situation is expected. In this case, degradation of the superconductor surface

on the length scale of the order of several nanometers which is typical for these materials can result in crucial changes in the transport characteristics.

Our calculations for N-I-n-S and S-n-I-n-S heterostructures were based on a scattering-like formalism taking into account all transmission and reflection events in the system. We have shown that the constructive interference of electron and hole waves within the n interlayer leads to the shift of maximums in conductance spectra to lower voltage positions and appearance of well-defined dips at voltage biases which exactly correspond to the energy gap value Δ_s in corresponding N-I-S and S-I-S superconducting trilayers without degraded interfaces. To take into account the finite value of the mean free path of a quasiparticle excitation l_n in a nm-thick n -interlayer we have introduced an additional imaginary term $\pm i/(2l_n)$ in the wave vector of an electron (a hole) in the n interlayer (see also [6]). Figs. 1 and 2 show some represented curves illustrating our statements.

From Fig. 1 it follows that with increasing d_n , the bound state formed due to the interference of electron and hole waves is shifted to lower voltages and a pronounced dip appears slightly below the gap value (Fig. 1, dashed curve). For larger d_n we can see the appearance of an additional hump structure (Fig. 1, dotted curve) above the gap voltage bias which reminds about the presence of a non-analytical square-root dependence of Andreev-reflection amplitudes.

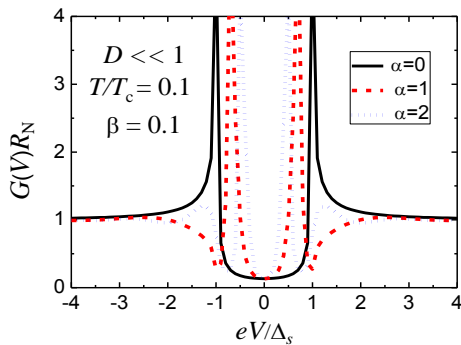


Fig. 1: Low-temperature differential conductance-versus-voltage characteristics for a planar three-dimensional N-I-n-S junction with various thicknesses of the normal n interlayer in the tunneling regime (the barrier transparency $D \ll 1$); parameters

$\alpha = 2d_n\Delta_s/(\hbar v_F)$ and $\beta = d_n/l_n$, the s -pairing symmetry of the superconducting order parameter is assumed.

In Fig. 2 we show conductance spectra of a heterostructure with two superconducting electrodes and an insulating layer with transparency D near unity.

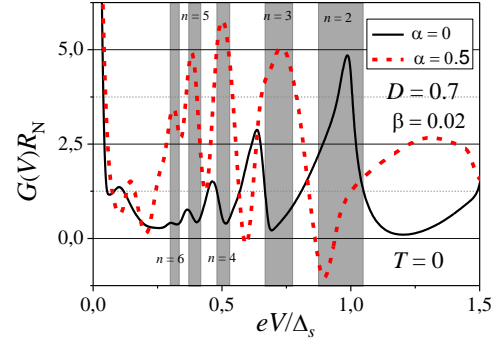


Fig. 2: Low-temperature differential conductance-versus-voltage spectra for a planar three-dimensional S-n-I-n-S junction with identical superconductors and high-transparency transition region ($D = 0.7$) without n -interlayer ($\alpha = 0$) and for a finite thickness of the normal n interlayer. Shaded regions show positions of the $2\Delta_s/n$ features (peaks in the first case and dips in the second one). The s -pairing symmetry of the superconducting order parameter is assumed.

Our results throw some light on unexpected features of transport characteristics in superconducting heterostructures with degraded interfaces. Comparison of the theoretical simulations with concerned measured data provides a way for determining correct gap values.

This work was performed within the German-Ukrainian project SE 664/18-1, Deutsche Forschungsgemeinschaft (DFG) and partly supported by the grant No. 612600 LIMACONA “Light-Matter Coupling in Composite Nano-Structures”, the EU Seventh Framework Programme,

References

- [1] P. Seidel and J. Richter. Phys Status Solidi B **98**, 189, 1980.
- [2] T. Geiges. Tunnelling experiments in high T_c superconductors: intrinsic and heating effects. PhD Thesis, Lausanne, EPFL, 2005.
- [3] H.Y. Günel, N. Borgwardt, I.E. Batov *et al.* Nano Lett. **14**, 4977, 2014.
- [4] S.M. Freake and C.J. Adkins. Phys. Lett. **29A**, 382, 1969.
- [5] D.H. Prothero. Phil. Mag. **29**, 829, 1974.
- [6] F. Yang and R.-B. Liu. Sci Rep, **5**:12109, 2015.

Direction-dependent RBS channelling studies in ion implanted LiNbO₃

E. Wendler, G. Becker, J. Rensberg, E. Schmidt, S. Wolf, W. Wesch

Lithium niobate (LiNbO₃) has outstanding properties, which makes it useful as substrate for optical devices. For device production, also ion implantation is of importance because it can be used for the modification of the optical properties of LiNbO₃ and for patterning by application of ion beam enhanced chemical etching (IBEE) (see e.g. [1] and references therein).

It is known that a different amount of damage was detected by Rutherford backscattering spectrometry in channelling configuration RBS/C in ion implanted LiNbO₃ crystals depending on how the used crystals were cut. In the hexagonal unit cell of LiNbO₃, the lattice vectors **a** and **c** correspond to the x- and z-direction, respectively. The crystal consists of oxygen octahedrons sitting on strings along the z-direction. The centres of the octahedrons are alternately occupied by Li, Nb and a vacancy. LiNbO₃ commonly used in experiments are X- and Z-cut samples with x- and z-axis being parallel to the surface normal, respectively. The different damage concentrations measured with RBS/C in X- and Z-cut LiNbO₃ were attributed to Nb atoms occupying the free octahedron sites of the LiNbO₃ lattice [2]. These free octahedron lattice positions are hidden along the atomic rows in x-direction but placed within the channels in z-direction, which can explain the low damage concentration measured in x-direction and the high one measured in z-direction, respectively.

However, to our knowledge all measurements discussed in literature were performed on different samples. But the

damage concentration measured after implantation may also depend on the crystal cut used for the ion implantation. In case of the hexagonal GaN, for example, different damage concentrations were measured with RBS in c-direction depending on whether the c-axis was parallel to the surface normal during ion implantation or not [3].

Three different types of congruent LiNbO₃ crystals purchased from CrysTec GmbH were used: common X- and Z-cut samples and additionally samples with the surface normal in the x-z plane being 45 degrees away from both the x- and z-direction, which are called for short XZ-cut in the following text.

Samples of each kind were implanted simultaneously with 350 keV argon (Ar) ions to ion fluences ranging from 2.5×10^{13} to 1×10^{15} cm⁻². All samples were analysed by RBS/C using 1.4 MeV He⁺ ions and a backscattering angle of 170 degrees.

The resulting damage profiles for X-, Z-cut samples are shown in Fig. 1a and those for the XZ-cut samples in Fig. 1b. A more detailed discussion of these profiles is given in Ref. [4]. Figure 1 shows that the profiles obtained for a given crystalline direction (x-direction, z-direction) but different sample cuts (X-, Z-, XZ-cut) are in reasonable agreement. The defect concentration for a given direction is independent of the sample cut. And the defect concentration for Z-cut is reduced compared to X-cut LiNbO₃. This becomes even more obvious when comparing the mean damage concentration in the maximum of the measured distribution,

n_{da}^{max} , as a function of the ion fluence N_I for the various samples investigated as shown in Fig. 2. In this figure, data from previous studies on 350 keV Ar ion implanted LiNbO₃ are included for comparison [5]. Although the damage formation does not depend on the crystal cut used for ion implantation, the damage concentration measured with RBS depends on the crystal alignment.

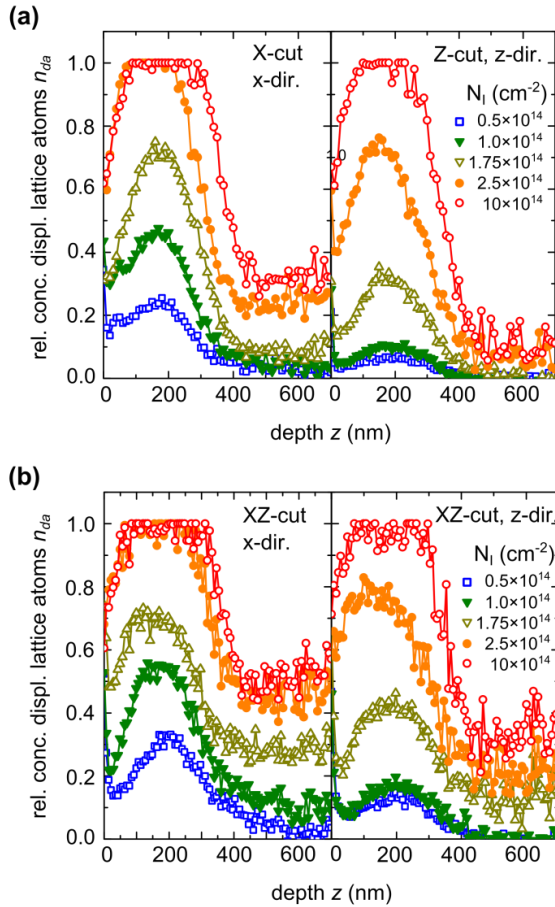


Fig. 1: Relative damage concentration n_{da} versus depth z for LiNbO₃ implanted with 350 keV Ar ions to various ion fluences. The profiles were calculated from the RBS channelling spectra measured on (a) X-cut and Z-cut samples, (b) XZ-cut samples in x -direction and XZ-cut samples in z -direction.

These results provide a clear proof that displaced Nb atoms in ion implanted LiNbO₃ occupy preferably the free octahedron sites of the LiNbO₃ lattice

structure. This result is further confirmed by angular-resolved RBS measurements [4]. In this case spectra were measured on one sample as a function of two orthogonal angles between the surface normal and the ion-beam direction. From these data well defined angular scans over several crystal planes can be deduced (not shown). The results obtained are in complete agreement with those shown above [4].

From our results it can be unambiguously concluded that Nb atoms displaced during ion implantation preferably occupy the free octahedron sites of the LiNbO₃ lattice structure and most likely also form Nb_{Li} antisite defects. The applied techniques can be also applied to implanted crystals with other structures.

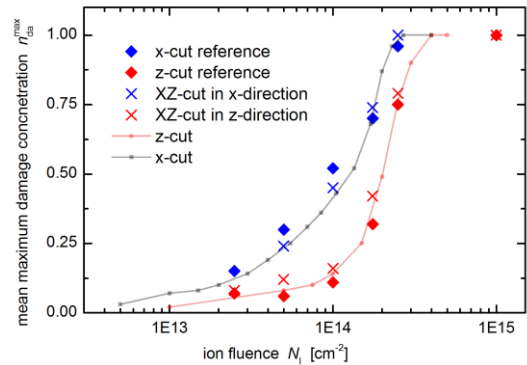


Fig. 2: Mean maximum damage concentration n_{da}^{max} versus ion fluence N_I for LiNbO₃ implanted with 350 keV Ar ions. Large symbols represent the results of the present work and the lines with small symbols show previous results [5].

References

- [1] F. Schrepel *et al.*, Nucl. Instrum. Methods Phys. Res. B 250 (2006) 164.
- [2] H. Karge *et al.*, Nucl. Instr. Methods 182 (1981) 777.
- [3] K. Lorenz, E. Wendler, private commun.
- [4] E. Wendler *et al.*, Nucl. Instrum. Methods Phys. Res. B, *in press*.
- [5] F. Schrepel *et al.*, Nucl. Instr. and Methods Phys. Res. B. 250 (2006) 164.

Ion-induced erosion of ice-covered carbon grains in molecular clouds and planetary disks

Cornelia Jäger, Tolou Sabri, Guiseppe Baratta¹, Maria Elisabetta Palumbo¹, Elke Wendler, Thomas Henning², Giovanni Strazzulla¹

¹ INAF–Osservatorio Astrofisico di Catania via Santa Sofia 78, 95123 Catania, Italy

² Max-Planck-Institut für Astronomie, Königstuhl 17, 69117 Heidelberg, Germany

IR observations with the ISO and Spitzer satellites have clearly confirmed that solid carbon dioxide is abundantly present along the line of sight to quiescent clouds and star forming regions. Since CO₂ has a low abundance in the gas-phase, it is supposed to be synthesized on grains by energetic processing of icy mantles and/or by surface reactions. In the laboratory, we simulated the ion-induced processing of grain/ice composites in astrophysical environments by studying the synthesis of CO and CO₂ in an ice layer on top of amorphous carbon grains at ~15 K [1].

Such carbon particles with fullerene-like structures were produced by pulsed laser ablation of isotopically pure ¹³C targets and subsequent grain condensation in a quenching He/H₂ gas atmosphere [2]. The thickness of the layers on either KBr or Si substrates was adjusted to 120 nm (dense film) corresponding to ~1000 nm of a porous, particulate film. These layers were placed in the UHV chamber, cooled down to 17 K, covered with O₂ or H₂O ices, and finally bombarded with 200 keV protons. A 200 kV ion implanter that was connected to the UHV chamber at the INAF-Osservatorio Astrofisico di Catania served as an ion source. The growth of ices was monitored by IR spectroscopy. Ice thicknesses were derived by the laser interference method and were found to be 250 and 130 nm for the H₂O and the O₂ film, respectively. IR spectra were acquired in situ before and after ion bombardment at 17 K. The carbon grains

were used for multiple ice depositions and H⁺ bombardments with fluences of 6.57×10^{15} , 1.65×10^{16} , 1.65×10^{16} , 1.15×10^{16} , and 1.65×10^{16} ions cm⁻² corresponding to a total dose of 6.76×10^{16} ions cm⁻². The penetration depth of the impinging protons is larger than the combined thickness of the carbon and ice layer according to SRIM calculations. In addition, to compare the ion-induced structural changes of carbon grains covered by ice with those having no ice layers, bare grains were bombarded with a fluence of 7×10^{16} 200 keV H⁺ ions cm⁻² at 16 K at the IFK in Jena.

Fig. 1 shows the appearance of narrow features in the ices due to the formation of ¹²CO, ¹³CO, ¹²CO₂, ¹³CO₂ molecules upon ion bombardment. The ¹³CO and ¹³CO₂ molecules are exclusively formed from the particulate carbon upon bombardment. The column densities of CO and CO₂ at varying ion fluences were calculated from the band areas divided by the band strengths of the corresponding molecules [1].

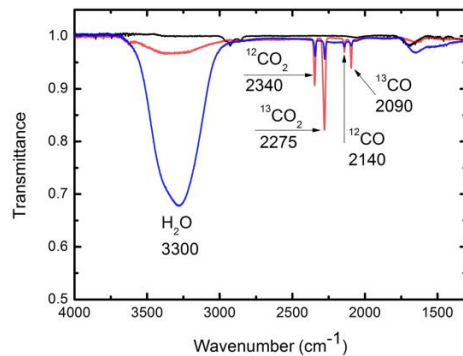


Fig. 1: IR spectra of bare ¹³C grains before ion bombardment (black line), ¹³C grains covered by H₂O (blue line) and O₂ ice (red line) after bombardment with 200 keV H⁺.

The column densities were used to determine the formation rate of ^{13}CO and $^{13}\text{CO}_2$ upon bombardment (see Fig. 2). The data were fitted with an exponential curve $y = A(1 - e^{-\sigma\phi})$, where A is the asymptotic value, σ the total cross section, and ϕ the fluence. The formation rate R is given by $R = A \times \sigma$ [1].

^{13}CO and $^{13}\text{CO}_2$ were formed from the solid phase by ion-induced erosion at the interface ice/grain. The amount of C removed from the layers was calculated to be 4.7 and 2.9 molecules/ion for $^{13}\text{CO}_2$ and ^{13}CO , respectively, corresponding to an erosion rate of 1.13×10^{-15} nm/ion. The ion fluence of 6.76×10^{16} $\text{H}^+ \text{cm}^{-2}$ applied in this study is equivalent to an H^+ bombardment during the grains' lifetime in dense molecular clouds [3]. Such processes may drastically reduce the amount of solid carbon in astrophysical environments such as accretion disks or molecular clouds and influence existing astrochemical models. The erosion of solid carbon also affects the formation of complex organics in the interstellar medium [4,5].

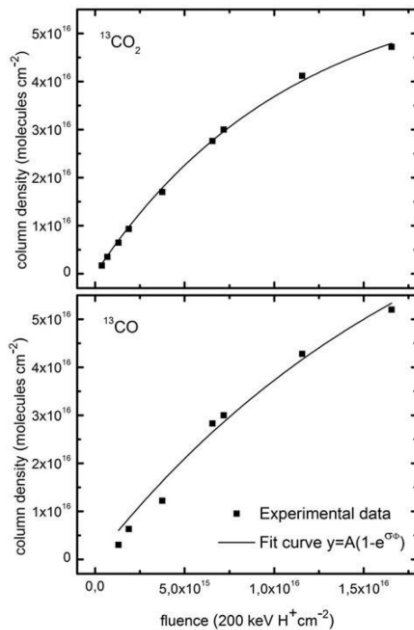


Fig. 2: Column densities of ^{13}CO and $^{13}\text{CO}_2$.

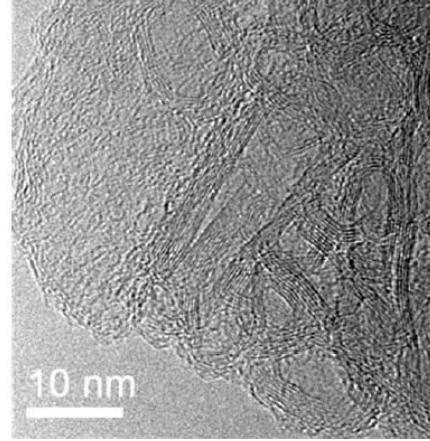


Fig. 3: High-resolution transmission electron microscope (HRTEM) image of the upper carbon layer after ion-induced processing of ice-covered fullerene-like carbon grains.

The erosion of carbon and formation of CO and CO_2 is accompanied by structural modifications of the remaining carbon grains, which can be observed in Fig. 3. The HRTEM image of carbon grains after proton bombardment provides insight into a strongly graphitized grain material. The structural modifications were found to be much stronger for ice-covered than for bare carbon grains, which could be explained by the increased reactivity at the surface due to dissociation of bonds and annealing effects by exothermic formation of molecules in the ice layer close to the interface ice/grains. The structural changes have a strong influence on the absorption efficiency in the IR up to the submillimeter range and the spectral index β ($Q_{\text{abs}/a} \sim \lambda^{-\beta}$) of the material.

References

- [1] T. Sabri et al., *Astronom. Astrophys.* **575**, A76 (2015).
- [2] C. Jäger et al., *Astrophys. J.* **689**, 249-259 (2008).
- [3] V. Mennella et al., *Astrophys. J.* **615**, 1073-1080 (2004).
- [4] S. Ioppolo et al., *Astronom. Astrophys.* **493**, 1017-1028 (2009).
- [5] E.A. Bergin et al., *Faraday Discussions* **168**, 61-79 (2014).

Photostability of PAH molecules - Interstellar chemistry

Gaël Rouillé, Serge A. Krasnokutski, Daniele Fulvio, Cornelia Jäger, Gustavo A. Garcia¹, Xiao-Feng Tang¹, Laurent Nahon¹, and Thomas Henning²

¹ *Synchrotron SOLEIL, L'Orme des Merisiers, Saint-Aubin BP 48, 91192 Gif-sur-Yvette Cedex, France*

² *Max-Planck-Institut für Astronomie, Königstuhl 17, 69117 Heidelberg, Germany*

The presence of polycyclic aromatic hydrocarbon (PAH) molecules in the interstellar medium (ISM) implies a life cycle comprising various formation and destruction mechanisms. Accordingly, the populations of PAH molecules must be dominated by the species with the most favorable balance between formation and destruction rates. The formation and destruction of regular PAH species, which are composed of fused, six-membered aromatic carbon cycles only, may proceed via the production of intermediates such as PAH molecules carrying hydrocarbon side groups. Thus regular and substituted PAH molecules may be present in the ISM.

The diffuse ISM is mostly constituted by H I regions where photons can carry an energy as high as 13.6 eV, more energetic ones being largely absorbed by H atoms. In such an environment, photodissociation could represent a significant destruction mechanism of PAH species. In a recent study, we proposed that fast intramolecular vibrational energy redistribution and internal conversion would prevent the photodissociation of ethynyl-substituted PAH species [1]. The verification of this proposition required experiments that we eventually carried out at the DESIRS beamline of the SOLEIL synchrotron facility [2].

The photoelectron photoionization coincidence (PEPICO) spectroscopy of phenanthrene, pyrene, 9-ethynylphenanthrene, and 1-ethynylpyrene was

performed at energies up to 20 eV. This technique provided us with the ionization energy E_i of each species (Fig. 1) and also the appearance energy of fragment ions produced by the loss of atoms by the parent molecules upon photoionization (Fig. 2).

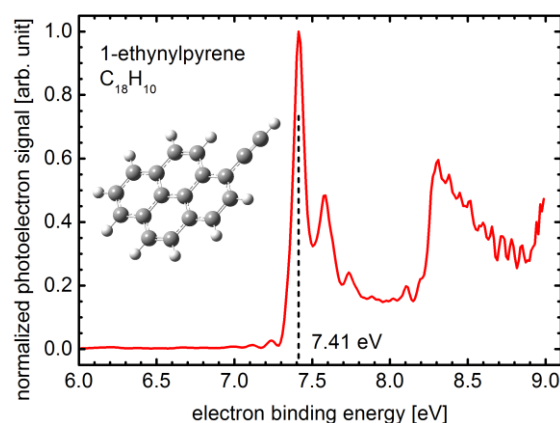


Fig. 1: Photoelectron spectrum of an ethynyl derivative of pyrene recorded at 9.0 eV with indication of the first ionization energy.

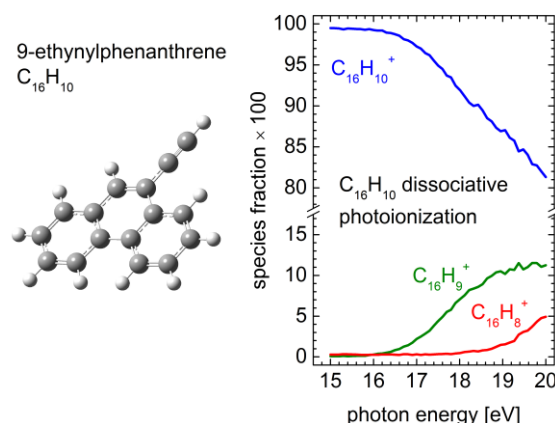


Fig. 2: Breakdown curve describing the fragmentation of 9-ethynylphenanthrene upon photoionization. The loss of one and then two H atoms is observed.

We have found that the ethynyl-substituted PAH molecules are similar to their regular counterparts in terms of ionization energy. Moreover, the similarity extends to the appearance energy $E_{a,-H}$ of the singly dehydrogenated fragment ion [2].

and dihydrogenated derivatives, ethynyl-substituted PAH molecules are as photostable as the non-substituted species in H I regions [2]. As the latter can survive the UV radiation field of the ISM provided that they contain at least 30 to 50 C atoms [4, 5], the same can be inferred for their

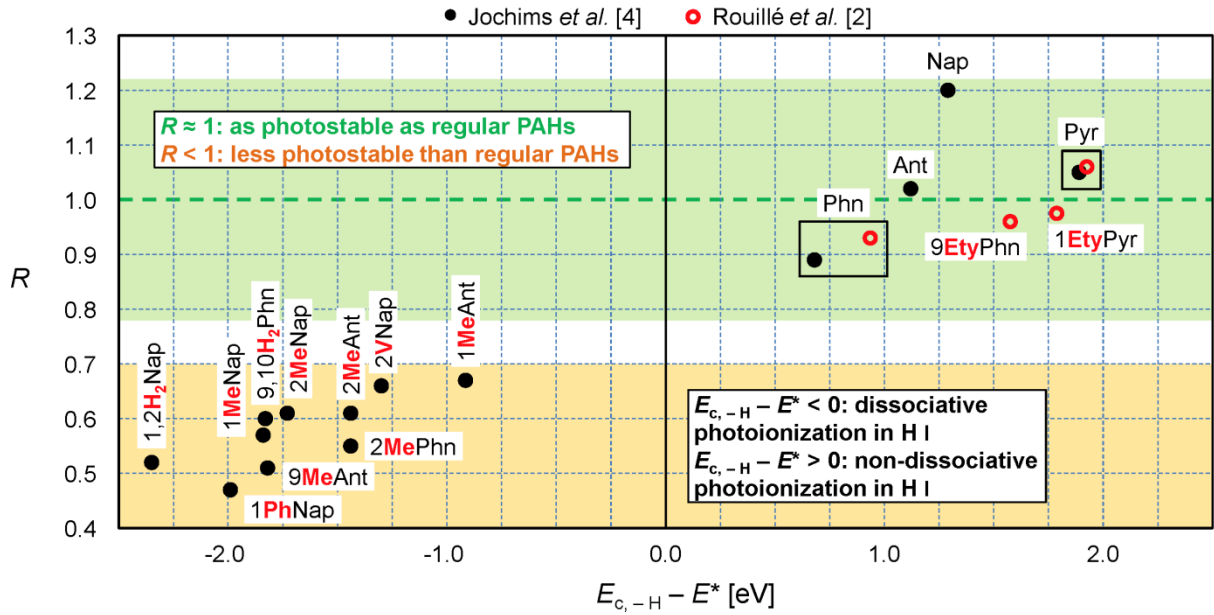


Fig. 3: Photostability of PAH derivatives compared with that of regular species. R is a relative photostability index, $E_{c,-H}$ is the critical energy for the loss of a H atom, and $E^* = 13.6 - E_i$. Nap: naphthalene; Ant: anthracene; Phn: phenanthrene; Pyr: pyrene; Me: methyl; Ety: ethynyl; V: vinyl; Ph: phenyl; H₂: dihydrogenation. The numbers indicate the position of the side group(s) in the molecular structure.

In contrast, past studies reported lower E_i and $E_{a,-H}$ values when comparing methyl-, vinyl-, and phenyl-substituted PAH molecules with regular species [3]. The same observation was made for dihydrogenated PAH species [3]. An analysis using the Rice-Ramsperger-Kassel theory for unimolecular reaction rates concluded that these various derivatives were less photostable than the regular species in H I regions. The relative photostability is estimated with the index R (Fig. 3).

Following the same procedure, the analysis of our experimental data has shown that, unlike methyl, vinyl, phenyl,

ethynyl derivatives. These may therefore contribute to the interstellar populations of PAH molecules as members and also as intermediates in the growth of PAH species through reactions with other interstellar species such as C and C₂H.

References

- [1] G. Rouillé *et al.*, Proc. Int. Astron. Union **9**, 276-280 (2013).
- [2] G. Rouillé *et al.*, Astrophys. J. **810**, 114 (2015).
- [3] H. W. Jochims *et al.*, Astrophys. J. **512**, 500-510 (1999).
- [4] H. W. Jochims *et al.*, Astrophys. J. **420**, 307-317 (1994).
- [5] T. Allain *et al.*, Astron. Astrophys. **305**, 602-615 (1996).

In-situ temperature dependent resistance measurement of ion irradiated vanadium dioxide thin films

Alexander Tille, Jura Rensberg and Carsten Ronning

Vanadium dioxide exhibits an insulator-metal-transition (IMT) from a low-temperature insulating state to a high-temperature metallic state at a critical temperature $T_C \sim 68^\circ\text{C}$ [1]. The phase transition is characterized by an abrupt decrease in resistivity by 3-4 orders of magnitude and dramatic changes of the optical properties in the near-to-mid infrared region [2]. These properties make vanadium dioxide suitable for applications in thermal, electrical and optical sensing and switching devices. But for many practical applications a critical temperature near room temperature is desired.

It is well known, that the critical temperature of the phase transition of VO_2 can be controlled by impurity doping or strain. Recently it was shown, that the intentional creation of irradiation defects can also be utilized to control T_C [3]. To compare the influence of irradiation with different ion species on the phase transition of VO_2 a new sample holder for in-situ electrical measurements as a function of temperature was set up in the ROMEO implantation chamber of the institute of solid state physics. The sample holder is shown in figure 1.

The sample is mounted together with a resistance temperature detector PT1000 on top of a copper block in a 4-wire sensing set up. The copper block is attached to a teflon disc, which thermally isolates the copper block from the liquid nitrogen cooled base. The copper block is heated electrically by two resistors up to 200°C and cooled down to -100°C by a cold bridge connected to the base. The temperature can be ramped or

kept constant with a PID-controller. Heating and cooling rates of several $10^\circ\text{C}/\text{min}$ can be achieved. The ion beam is constantly scanned over the sample and its current is measured using a faraday cup system, separated from the sample holder, enabling electrical measurements even during ion irradiation.

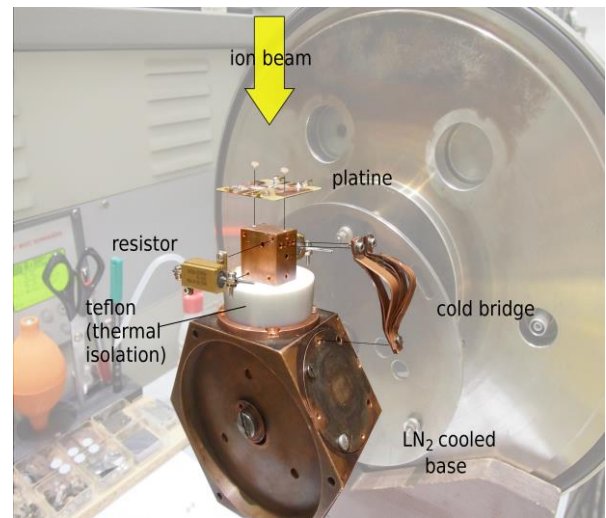


Fig. 1: Sample holder for 4-wire sensing setup in the romeo implantation chamber. The temperature can be varied in the range from -100°C to 200°C .

In a first experiment, we irradiated a 100 nm thin film of VO_2 deposited on Al_2O_3 with 75 keV Ar^+ ions in various fluence steps at a fixed temperature of 0°C , respectively. After each irradiation step the temperature dependent resistance was measured in the temperature range from 0 to 100°C . The results of this measurement are summarized in Figure 2. The dark blue curve is the intrinsic reference measurement and shows the typical hysteresis of a VO_2 thin film upon heating and cooling. At temperatures below 60°C the entire film is insulating and displays high resistance

values, whereas at temperatures above 80°C the film shows low resistance values typical for a bad metal.

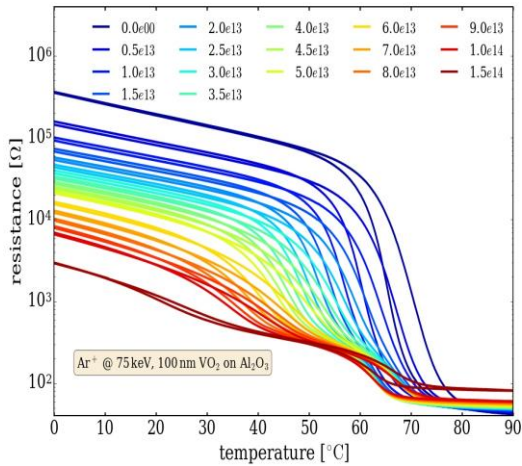


Fig. 2: Temperature dependent resistance curve of an Ar^+ implanted VO_2 thin film.

Consequently, in the transition temperature region the resistance drops by 3 orders of magnitude. With increasing Ar^+ fluence (from blue to red in figure 2) the transition temperature shifts to lower temperatures reaching room temperature for the highest ion fluence shown. The second hysteresis, that is present at $\sim 65^\circ\text{C}$ for all irradiated samples, originates from un-irradiated but strained VO_2 located under the electrical contacts. The contacts shadow the sample from the ion beam. As a result we measure a series connection of strained intrinsic and ion irradiated VO_2 which results in two distinct hysteresis curves.

Our new setup can be used to investigate the electrical properties of various phase-transition materials and the influence of ion irradiation on their phase-transition properties in a short amount of time.

References

- [1] F. J. Morin, Phys. Rev. Lett. **3**, 34 (1959).
- [2] Xinfeng He et al., Phys. Chem. Chem. Phys. **17**, 11638-11646 (2015).
- [3] Rensberg et al., Nano Lett. **16** 1050 (2016).